

ON THE DEVELOPMENT AND
AUTOMATION OF A HIGH-SPEED
LOAD-PULL SYSTEM BASED ON
PXIE MODULES



THOALFUKAR HUSSEINI

DEPARTMENT OF ELECTRICAL ENGINEERING

CARDIFF UNIVERSITY

THIS DISSERTATION IS SUBMITTED FOR THE DEGREE OF

Doctor of Philosophy

Engineering School

November 2018

This thesis is dedicate to my loving parents

DECLARATION

This work has not been submitted in substance for any other degree or award at this or any other university or place of learning, nor is being submitted concurrently in candidature for any degree or other award.

Signed(candidate) Date

STATEMENT 1

This work has not been submitted in substance for any other degree or award at this or any other university or place of learning, nor is being submitted concurrently in candidature for any degree or other award.

Signed(candidate) Date

STATEMENT 2

This thesis is the result of my own independent work\investigation, except where otherwise stated, and the thesis has not been edited by a third party beyond what is permitted by Cardiff University's Policy

Thoalfukar Hussein

on the Use of Third Party Editors by Research Degree Students. Other sources are acknowledged by explicit references. The views expressed are my own.

Signed(candidate) Date

STATEMENT 3

I hereby give consent for my thesis, if accepted, to be available online in the University's Open Access repository and for inter-library loan, and for the title and summary to be made available to outside organisations.

Signed(candidate) Date

Thoalfukar Hussein

November 2018

ACKNOWLEDGEMENTS

I would like to express my deepest appreciation to my supervisor **Prof. Johannes Benedikt** for his guidance and for spending an incredible amount of time imparting his knowledge and ideas to me. His knowledge and experience in the field of measurement systems and RF devices are second to none and my PhD project would definitely not have taken off without his expert supervision.

I would like to extend heartfelt thanks to **Prof. Paul J. Tasker** for his support and guidance throughout the duration of this research project. His invaluable support, encouragement and academic wisdom gave me confidence in overcoming difficult times. His expert advice has permanently been of great help, and he has been a support with a sound knowledge in the field of RF and Microwave Engineering.

A big thank and deepest appreciation goes to **Dr. James J. Bell** who has gone far beyond the work of assisting me. He has always kept me on the right track and I thank him for his support, guidance, effort,

advice, encouragement with my research and entire studies. Without his endless support, it would not be possible to finish this work.

I would also like to extend my sincerest thanks to the other members of the Cardiff Centre for High Frequency Engineering who have been too willing to help whenever they could. They include Dr. Jonathan Lees, Dr. Roberto Quaglia, Azam Al-Rawachy, Kauser Chaudhry, Alex Alt, Michael Casbon, Syed Anera, Jacob Stanswood, Samuel Hefford and Dr. Randeep Saini.

My deepest appreciation goes to my father who taught me how to walk uprightly, and develop honesty and integrity in my life. To my mother, who has always been available to provide good advice and to be a listening ear, and my sisters for their continuous support and encouragements.

Finally, I would like to express a special “thank you” to the most important persons of my life, my beloved wife Marwa and children Taha, Sama, and Ali. Their support and existence in my life during the PhD had helped me more than anything else. They have always brought in my life serenity and love and they have borne the hardships

Thoalfukar Hussein

of alienation and my preoccupied for the study during the course of the PhD. For this, I will always be grateful to them. Thank You.

ABSTRACT

Recent RF applications and research require thousands of accurate measurements to be performed within a practical time. For instance, the global model extraction of a DUT requires thousands of accurate measurements, which would take a very long time when using the traditional RF measurement systems because they are relatively slow. Moreover, the inaccessible software that is used by the traditional systems has made them a vendor-defined system, where their application cannot be extended or amended. This is contrary to the need for a flexible RF system that can be extended and modified according to user preferences. Furthermore, the traditional load-pull measurement strategies are time-consuming thanks to the iteration process and the need for the user interaction. Therefore, developing a new high-speed measurement is essential.

This work demonstrates a high-speed load-pull measurement system that maintains flexibility, accuracy, speed, and high dynamic range. The system's architecture is based on PXIe modules, where the signal

detection is achieved through the use of vector signal analysers (VSA) that can operate over 50 MHz frequency bandwidth. The RF signal generation employs vector signal generators (VSG) using continuous wave (CW) mode generation. The system is calibratable over a 100 dB dynamic range and the measurement speed approaches 200 measurements/sec at 10K samples/average. Due to the accessibility of the raw measured data and the customisable written software, statistical information has been employed to monitor the quality of the measurements and the status of the system. Moreover, an automated active load-pull measurement has been implemented on this measurement system. The automated process has been achieved by exploiting the load-based Cardiff behavioural model. This model is used to predict the required injected signals a_{21} to emulate a load impedance at the DUT reference plane, wherein the results show the ability of the model to achieve a load-target with an error less than -35 dB. The prediction of the DUT's response by the model combined with customised software has allowed for an automated fundamental active load-pull process that requires minimum user interaction to automatically identify the optimum load conditions for the design-relevant parameters (e.g. gain, efficiency or output power over one or multi-power levels) within a few seconds. Two methods have been used to take the impact of the test-set on the generated signal into account: descriptive function and

simple look-up table. These two approaches have been implemented and verified. The results show that each model can achieve the power target with a residual error of less than 0.1 dB.

The automation process has not only covered the definition of the optimum impedances over different power levels but has also identified, in a time efficient manner, the appropriate load-pull impedance space. This ensures that the model's coefficients, which are required for predicting the DUT's response b_{21} and efficiency, are accurately extracted. This approach significantly reduces the number of required measurements, and hence reduces the measurement time when compared to the traditional approach. It takes less than 42 sec to perform 1282 load-pull measurements, that define the appropriate design space (-3dB power contours) for 16 power levels while ensuring that the a- wave based Cardiff behavioural model is simultaneously and accurately extracted.

For the sake of an efficient utilization of the measurement system and further reduction in the required number of measurements required to generate a global behavioural model that is compatible for CAD-tool design, a linear interpolation approach over the extracted coefficients was employed and verified. This approach has allowed

further reduction in the number of measurements because there is no need to perform the load-pull measurement over a high dense grid of input drive power levels (a_{11}), which is essential for the global model generation.

TABLE OF CONTENTS

List of publications	xvi
List of Abbreviation	xvii
1 Introduction	1
1.1 Background	1
1.2 Device Characterisation	6
1.3 Load-Pull Measurement	8
1.4 Research Motivation	10
1.5 Research Objectives	12
1.6 Dissertation Structure	13
References	16
2 Literature Review	19
2.1 Introduction	19
2.2 Linear Characterisation	21
2.3 Non-Linear Characterisation	26
2.3.1 Evolution of Non-linear Measurement Systems	27

2.3.2 NVNA Calibration	30
2.4 Load-Pull Measurement	35
2.4.1 Passive Load-Pull Measurements	36
2.4.2 Active Load-pull Measurements	39
2.5 Chapter Summary	56
References	60
3 High Speed Measurement System Based on PXIe Modules	66
3.1 Introduction	66
3.2 System Description	68
3.3 System Calibration	74
3.3.1 Intra-Chassis Time-based Alignment	75
3.3.2 Receiver Phase and Power Alignment	79
3.3.3 Requirement for a Dedicated Receiver Calibration .	83
3.3.4 System Calibration and Verification	90
3.4 Measurement System Performance	96
3.4.1 Dynamic Range and Measurement Speed	96
3.4.2 Standard Deviation Measurement	99
3.4.3 Analysis and Utilisation of Data Statistics	102
3.5 Chapter Summary	105
References	107
4 Automated Fundamental Load-pull Measurement	109

4.1	Introduction	109
4.2	Automated Active Load-Pull Measurement	112
4.2.1	Initial Measurements	115
4.2.2	Load-based Cardiff Behavioural Model	117
4.2.3	Optimum Impedance Tracking	119
4.2.4	Load-pull Over Power-sweep	124
4.3	Characterisation of Test-Set Nonlinearities	128
4.3.1	Look-Up Table Approach	130
4.3.2	Descriptive Function Approach	134
4.4	Second Harmonic Load-Pull	140
4.5	Chapter Summary	145
	References	147

5 Automating the Determination and Verification of Nonlinear Behavioural Models 149

5.1	Introduction	149
5.2	Optimum Design Space Search Algorithm	151
5.3	Prediction of the Efficiency Contours	160
5.4	Behavioural Model Extraction and Verification	164
5.5	Power Contours Over Different Input Power Levels	167
5.6	Linear Interpolation of the Model's Coefficients	174
5.7	Chapter Summary	179

References	183
6 Conclusion and Future Work	184
6.1 Conclusion	184
6.2 Future Work	190
Appendix A	193
Appendix B	206

LIST OF PUBLICATIONS

- [1] T. Hussein, A. Al-Rawachy, J. Benedikt, J. Bel, and P. Tasker, "Automating the accurate extraction and verification of the cardiff model via the direct measurement of load-pull power contours," in *IEEE/MTT-S International Microwave Symposium*, June 2018, pp. 544–547.
- [2] T. Hussein, A. Al-Rawachy, S. S. Anera, J. Bell, P. Tasker, and J. Benedikt, "On the effective modeling of the test-set non-linearity," in *2018 91st ARFTG Microwave Measurement Conference (ARFTG)*, June 2018, pp. 1–4.
- [3] A. Al-rawachy, T. Hussein, J. Benedikt, and P. J. Tasker, "Cardiff behavioural model analysis using a two tone stimulus," Jan. 2019, to be published.

LIST OF ABBREVIATION

ADC	Analogue to Digital Converter
CAD	Computer-Aided Design
CW	Continuous Wave
DAC	Digital to Analogue Converter
DSO	Digital Sampling Oscilloscope
DUT	Device Under Test
ENOB	Effective Number of Bits
GUI	Graphical User Interface
HPR	Harmonic Phase Reference
IC	Integrated Circuit
LabVIEW	Laboratory Virtual Instrument Engineering Workbench
LMS	Least Mean Square

LO	Local Oscillator
LPA	Load-Pull Power Amplifier
LSNA	Large-Signal Network Analyzer
LUT	Look-Up Table
MMIC	Monolithic Microwave Integrated Circuit
MXIe	Multisystem eXtension Interface
NMSE	Normalised Mean Square Error
NVNA	Nonlinear Vector Network Analyzer
OSR	Oversampling Ratio
PA	Power Amplifier
PCIe	Peripheral Component Interconnect Express
PFI	Programmable Function Interface
PHD	Poly Harmonic Distortion Model
PNA-X	Phase Network Analyzer-X Parameter
SSPA	Solid-State Power Amplifier
T-Clk	Trigger Clock
VNA	Vector Network Analyzer

VSA	Vector Signal Analyser
VSG	Vector Signal Generator
WLAN	Wireless Local Area Network
WPAN	Wireless Personal Area Network
ZVA	Z Vector Analyzer

CHAPTER 1

INTRODUCTION

1.1 BACKGROUND

WIRELESS communication of significant distance was first performed by Guglielmo Marconi in 1894, who used it for communication between sea ships. Marconi's discovery was the result of many years of attempts that started with the invention of the telegraph, produced by Samuel Mores in 1838, and followed by Alexander Graham Bell in 1870 who invented the telephone [1]. Marconi's invention in 1894 was based on electromagnetic propagation theory, which was formulated in 1873 by James Clerk Maxwell [2]. After the success of the initial wireless transmissions, its use was extended during the Second World War to radar and radio applications. In 1947, the first transistor was invented by American physicists John Bardeen and Walter Brattain in Bell Laboratories. This invention led to the

development of the first bipolar junction transistor in 1950 and hence the solid-state power amplifier (SSPA) was introduced [3, 4].

In the 1960s, this technology experienced a significant period of development that accelerate amplifier development for power generation, control and amplification. SSPA components became a critical factor in reducing the cost and size of communication sub-systems since it is a fundamental part of such system, where the size and price can be effected by it. The use of silicon substrates made it possible to integrate both active and passive components on the same substrate, hence the realisation of integrated circuits (ICs) and monolithic microwave integrated circuits (MMICs) [5].

In 1959, communication by satellite was first used. It has since enabled global communication, has supported telephone and TV channels, and is used for data links [6]. The combination of Marconi's invention and the integrated circuit, in addition to satellite communications led to the development of portable hand-held equipment. In 1973, Martin Cooper, a Motorola researcher, developed the first handheld cellular mobile phone. His first call was made to his rival at Bell Labs. However, these early mobile phone units were too big and heavy and heavy for practical use, and the battery also required an

extensive amount of time for recharging. Meanwhile, the number of users of the cellular phone system grew rapidly. This motivated competitive manufacturers to provide handsets with higher performance at a lower cost.

Several generations of cellular phones have been created since the first commercial handset was released in 1978. The initial generations were exclusively used for carrying voice and the early cellular network could only be used by a limited number of users due to frequency band limitations [7]. The second generation of the mobile phone network was able to handle larger number of calls, and it reduced the risks of interference and dropped calls [7]. The data rates of this generation were supported by the basic 2G networks, which were only 9.6 kbps. Therefore, this second generation was inadequate to provide any sophisticated digital services [8].

The third-generation (3G) systems had many significant new features, including higher data transmission rates and large capacity of data storage. This made the 3G system more suitable for high-speed data, in addition to the traditional voice calls. The benefits of higher data rates and greater bandwidth meant that 3G mobile phones were able to offer subscribers a wide range of data services, such as mobile

Internet access and multimedia applications. Nevertheless, the 3G system required a further development to support the new generation of applications, such as TV streaming, multimedia, video-conferencing, web browsing, e-mail, and navigational maps.

Fourth-generation (4G) systems provided many advanced services over the 3G system, such as a higher transmission rate of up to 1GB/s. Moreover, the 4G system can handle a large number of users and is better quality when compared to the previous generations [9]. In addition, 4G systems have the ability to exchange and use information from other wireless services, such as satellite, cellular wireless, WLAN (Wireless Local Area Network), WPAN (Wireless Personal Area Network) and systems for accessing fixed wireless networks [9].

Function multiplicity, such as calling and web browsing, in a single mobile device would allow for a reduction in weight and size because most of these functions are software-designed and require no extra hardware component. Meanwhile, the existence of these functions in addition to the power amplifier (PA) allows for high power consumption. Basically, a PA is used to convert the DC power into RF power, which enables the wireless transmission of the RF signal containing digital information from a transmitter to a receiver over larger distances.

Consequently, the PA is considered to be one of the most power-dissipating parts in a wireless system [10]. When the PA is more efficient, less DC power is required to deliver the same amount of RF power. For a hand-held application that uses a battery as the power source, poor efficiency leads to shorter talk time and standby time [11]. This can severely limit the competitiveness of the final product within the market. Poor efficiency also leads to a large amount of heat dissipation, which can incur extra cost for cooling.

Various types of PA designs have recently been proposed to optimise and achieve an efficient PA. However, despite the good results that have been achieved, these designs have not achieved the ambition of a PA that consumes little energy during a long time. Therefore, the challenge for the PA design community is to seek an appropriate optimisation solution.

Generally speaking, two approaches have been used for PA design: model- and measurement-based design [12]. In the model-based design, the device model is first developed and is then used within the design. The device is characterised experimentally to generate the actual model. In the measurement-based design, the transistor device is first characterised and then the measured data are used directly

within the design process. The key behaviours of the device (e.g., gain, efficiency and load-pull contours) are recorded. Based on the measured information, the designers start the PA design immediately. Prototypes are then made to test the designed auxiliary circuitry and tune the overall system performance. The design process is finalised once the designed PA successfully passes the test.

1.2 DEVICE CHARACTERISATION

Transistor characterisation can be categorized into three main types; DC, small, and large-signal RF measurements. The DC measurements produce current-voltage relationships and can be done under pulsed or continuous excitations [13]. Traditionally, the DC-IV measurement in combination with small-signal S-parameter measurements is used for the behavioural model extraction.

Small-signal (S-parameter) RF measurements can be performed using Vector Network Analysers (VNAs). This kind of RF measurement is linearly dependent because it is not valid under large signal conditions, where the DUT starts generating harmonics and behaving non-linearly, the power gain decreases and the output power saturates [5, 14].

Simultaneously capturing harmonic components and their phase relationship is essential to define a complete picture of the device [16].

Due to the lack of harmonic phase information, it is impossible to measure voltage and current waveforms using standard Vector Network Analysers (VNAs). Therefore, the recently developed Nonlinear Vector Network Analyzer (NVNA) versions provide for calibrated time-domain waveforms [17]. These systems have the potential to provide insight into the time-domain voltage and current waveforms.

Non-linear device characterisation has been extended to include not only measurement into a 50Ω environment but also into different impedances. This includes passive and active load-pull techniques, including the envelope load-pull. This capability provides control over the shape of the DUT waveforms, which gives designers the possibility to engineer the waveform directly for a high-efficiency PA design. For example, the Mesuro MB150 active load-pull system features a time-domain solution whereby a Tektronix digital sampling oscilloscope (DSO) is used as the primary receiver [18]. Error correction and assessment are the key in all of these RF measurements.

1.3 LOAD-PULL MEASUREMENT

Load-pull is an essential technique for nonlinear device characterisation, in which the measurements are carried out as a function of load impedance [19, 20]. These load changes have a significant impact on the transistor's performance, such as output power, gain, efficiency and linearity. Therefore, load-pull measurement has been performed using two different kinds of techniques: passive and active load-pull. The passive technique uses a passive tuner to alter the fundamental or harmonic load impedance [21, 22]. However, achieving sufficiently high reflection coefficients can be difficult due to the inherent losses within the tuners. Moreover, the complexity of the measurement configuration would have an impact on the calibration accuracy because more attenuation can affect the signal.

For the active load-pull approach [23] the passive tuner is replaced by an active signal to emulate a target load impedance. This has allowed designers to tackle the problem of the passive technique because the injected signal can be generated by a phase-controllable synthesiser and amplified to generate the required load impedance [24]. Several different types of active load-pull approaches have been presented in literature, all of which used either closed-loop configuration or opened-

loop configuration [25, 26]. Each of these techniques have advantages and drawbacks; for example, despite the oscillation problem of the closed-loop active load-pull, this technique does not need an additional signal generator and this lowers the system's costs. Meanwhile, the opened-loop active load-pull requires long characterization times due to required iterations but does not experience the stability problem that are experienced by closed-loop active load-pull.

Several approaches and configurations have been investigated to enhance the accuracy of the active load-pull technique and reduce its measurement time. For instance, several different algorithms have been investigated to improve the iterative search procedure, such as Newton-Raphson and using the poly harmonic distortion model (PHD), where the correct injected signal to synthesize a required load is predicted [27–29].

New microwave instruments have been used to speed up the measurement time, such as the system from Anteverta [30, 31] to facilitate the measurement of the device reflection coefficient over a wide bandwidth in a single data acquisition. These developments will be explored in more detail in chapter 2. They have allowed for fast measurement speed compared to the traditional approaches but still have to undergo

extensive developments to become a more extendible and customizable system with a high measurement speed for small- and large-signal parameters over a large dynamic range.

1.4 RESEARCH MOTIVATION

Despite the considerable efforts that have been made by engineers to optimise large signal measurement approach, in general, and in term of load-pull measurements in particular, the resulting measurement processes still have a number of significant problems. The active load-pull measurements are time-consuming and also complicated. These measurements take significant time due to the typical low execution speed of the measurement system used and the iterative nature of the active load-pull measurements. These problems have led the device manufacturing industry to employ DC and S-parameter pass/fail type measurement regimes rather than load-pull characterisation. The avoidance of these kinds of measurement introduces a lack of data for optimum design data and sub-optimum developments because there is not enough information about the DUT while being measured at different conditions. This also hinders the development and extraction of a global behavioural model because the latter requires comprehensive measurements over different conditions [28].

Developing a new high-speed load-pull measurement system that has a high degree of hardware and software flexibility is of vital importance because this would not only help in tackling the aforementioned problems but would also create a new version of systems that are capable of holding additional functionalities and other different kinds of RF measurements that might be required in the future. The restricted access to software of traditional measurement systems restricts, at present, the further development or increase of the functionality of the system. Consequently, once a new functionality is required, a new system has to be acquired. Moreover, the 'closed box' hardware of traditional measurement systems complicates any development of the system architecture unless we replace the whole system, which is expensive.

1.5 RESEARCH OBJECTIVES

The research work presented in this thesis is focused on two main areas; the first one is developing a new load-pull measurement system potential of performing hundreds of measurements within a short time, while the second one is automating the load-pull measurement and the behavioural model extraction process. As a consequence, the main objectives of this research will be as following:

- To develop a high-speed load-pull measurement system.
- To develop new strategies that can perform automated load-pull measurements within a practical time.
- Establish an efficient use of the measurement system and an informed decision for a measurement.
- To develop new measurements strategies that can extract a reliable behavioral model while avoiding perform extra measurements.

1.6 DISSERTATION STRUCTURE

This thesis is structured into six chapters. Following this Introduction, Chapter 2 will review of the recently published research literature related to device characterisation and non-linear measurement system trends. In this chapter, two main subjects are covered, the first presents the recent developments of transistor characterisation, including linear and non-linear measurement, and the basic structure of the measurement system that is used. In addition, it will also review the important techniques that have been used for the non-linear measurement, such as passive and active load-pull. Moreover, the important trends to speed up active load-pull measurement will be described in this chapter. Furthermore, a brief comparison between different strategies of load-pull measurement will be mentioned in this chapter.

Chapter 3 describes the presented measurement system and its structure. The calibration process will be described in this chapter, which includes system calibration, power and phase alignment of the receivers, and synchronization achievement. Verification of the measurement system will also be conducted in this chapter, which includes verification of the small signal calibration and waveform measurement.

Moreover, this chapter demonstrates the system performance in terms of speed, dynamic range, data processing, data quality, and finally the conclusion.

The focus then shifts to load-pull characterisation, which is introduced in Chapter 4. This chapter covers the automatic fundamental load-pull measurement. The automated process and fundamental load-pull measurement over different drive power levels will both be explained in detail in this chapter. Moreover, two methods for characterizing the test-set of the load-pull measurement system will be discussed and verified. This chapter also includes details about a second harmonic load-pull, including results and the utilized strategy to perform successful measurement.

In Chapter 5, the load-based Cardiff behavioural model will be exploited to automate the process of active load-pull measurement that can extract a verified behavioural model over a single or multi-input power levels. In this scenario, the optimum design space has been proposed to be up to the -3 dB power contours and also the efficiency contours. The exploited strategy has also been used to define the required model order and how the order has to change according to the measurement conditions. The approach given in this chapter

facilitates also an efficient active load-pull approach that can automatically define the -3 dB power contours and customizable efficiency contours within the same load-pull measurement. For further reduction of the number of load-pull measurements and toward efficient utilization of the measurement system, the linear interpolation between the extracted model's coefficients will be implemented in this chapter. This approach can mitigate the required number of load-pull measurements to generate a global behavioural model.

Chapter 6 concludes the whole work presented in this thesis, while concentrating on the strengths and weaknesses of the presented work. This chapter will also propose possible directions for future research and optimization.

REFERENCES

- [1] I. Brodsky, *Wireless: The Revolution in Personal Telecommunications*. Artech House, 1995.
- [2] E. Braun and S. MacDonald, *Revolution in Miniature: The History and Impact of Semiconductor Electronics*. Cambridge University Press, 1978.
- [3] M. Bujatti and F. Sechi, *Solid-State Microwave High-Power Amplifiers*. Artech House, 2009.
- [4] S. Marsh, *Practical MMIC Design*. Artech House, 2006.
- [5] K. Chang, *RF and Microwave Wireless Systems*. Wiley, 2004.
- [6] T. S. Rappaport, *Wireless Communications: Principles and Practice*, 2nd ed. Prentice Hall, 2002, vol. 2.
- [7] G. Gow and R. Smith, *Mobile and Wireless Communications: An Introduction*. McGraw-Hill Publishing Co., 2006.
- [8] S. C. Cripps, *RF Power Amplifiers for Wireless Communications*, 2nd ed. Norwood, MA: Artech House, 2006.
- [9] J. Agar, *Constant touch: A global history of the mobile phone*. Icon Books Ltd, 2013.
- [10] J. L. Walker, *Handbook of RF and Microwave Power Amplifiers*. Cambridge University Press, 2011.
- [11] Y. Neuvo, "Cellular phones as embedded systems," in *IEEE International Solid-State Circuits Conference*, Feb. 2004, pp. 32–37 Vol.1.
- [12] H. Qi, "Nonlinear data utilization: direct data look-up to behavioural modelling," Ph.D. dissertation, Engineering, 2004. [Online]. Available: <http://orca.cf.ac.uk/id/eprint/54764>
- [13] B. S. Virdee, A. S. Virdee, and B. Y. Banyamin, *Broadband Microwave Amplifiers*. Artech House, 2004.
- [14] S. A. Maas, *Nonlinear Microwave and RF Circuits*, 2nd ed. Artech House, 2003.
- [15] M. J. W. Rodwell, D. M. Bloom, and B. A. Auld, "Nonlinear transmission line for picosecond pulse compression and broadband phase modulation," *Electronics Letters*, vol. 23, no. 3, pp. 109–110, Jan. 1987.

- [16] P. Roblin, *Nonlinear RF Circuits and Nonlinear Vector Network Analyzers*. Cambridge University Press, 2009.
- [17] J. Benedikt, R. Gaddi, P. J. Tasker, and M. Goss, "High-power time-domain measurement system with active harmonic load-pull for high-efficiency base-station amplifier design," *IEEE Trans. Microw. Theory Techn.*, vol. 48, no. 12, pp. 2617–2624, Dec. 2000.
- [18] P. J. Tasker, "Practical waveform engineering," *IEEE Microwave Magazine*, vol. 10, no. 7, pp. 65–76, Dec. 2009.
- [19] P. Poire, D.-L. Le, and F. M. Ghannouchi, "A PC controlled fully automatic active load-pull measurement system using a pseudo-gradient algorithm," in *IEEE Instrum. & Meas. Tech. Conf.*, April 1995, p. 628.
- [20] F. M. Ghannouchi and M. S. Hashmi, *Load-Pull Techniques with Applications to Power Amplifier Design*. Springer, 2013.
- [21] C. Tsironis, A. Jurenas, and C. Liu, "Highly accurate harmonic tuners for load pull testing," in *Asia-Pacific Microwave Conference*, vol. 3, Dec. 2001, pp. 1311–1314 vol.3.
- [22] R. Stancliff and D. Poulin, "Harmonic load-pull," in *IEEE MTT-S International Microwave Symposium Digest*, April 1979, pp. 185–187.
- [23] Y. Takayama, "A new load-pull characterization method for microwave power transistors," in *IEEE MTT-S International Microwave Symposium Digest*, June 1976, pp. 218–220.
- [24] D. J. Williams and P. J. Tasker, "An automated active source and load pull measurement system," in *6th IEEE High Frequency Postgraduate Colloquium*, Sep. 2001, pp. 7–12.
- [25] J. Verspecht, P. Debie, A. Barel, and L. Martens, "Accurate on wafer measurement of phase and amplitude of the spectral components of incident and scattered voltage waves at the signal ports of a nonlinear microwave device," in *IEEE MTT-S International Microwave Symposium*, May 1995, pp. 1029–1032 vol.3.
- [26] A. Ferrero and V. Teppati, "A complete measurement test-set for non-linear device characterization," in *58th ARFTG Conference Digest*, vol. 40, Nov. 2001, pp. 1–3.
- [27] Verspecht and D. E. Root, "Polyharmonic distortion modeling," *IEEE Microwave Magazine*, vol. 7, no. 3, pp. 44–57, June 2006.

- [28] R. E. Leoni, S. A. Harris, and D. G. Ries, "Active simultaneous harmonic source and load pull assisted by local polyharmonic distortion models," in *IEEE MTT-S International Microwave Symposium Digest*, May 2010, pp. 1166–1169.
- [29] R. S. Saini, J. W. Bell, T. A. J. Canning, S. P. Woodington, D. Fitz-Patrick, J. Lees, J. Benedikt, and P. J. Tasker, "High speed non-linear device characterization and uniformity investigations at x-band frequencies exploiting behavioral models," in *77th ARFTG Microwave Measurement Conference*, June 2011, pp. 1–4.
- [30] M. Marchetti, T. Maier, V. Carrubba, S. Maroldt, M. Mußer, and R. Quay, "Examples of high-speed harmonic load pull investigations of high-efficiency gan power transistors," in *IEEE International Conference on Microwaves, Communications, Antennas and Electronic Systems (COMCAS)*, Nov. 2015, pp. 1–4.
- [31] M. Thorsell and K. Andersson, "Fast multiharmonic active load-pull system with waveform measurement capabilities," *IEEE Trans. Microw. Theory Techn.*, vol. 60, no. 1, pp. 149–157, Jan. 2012.

CHAPTER 2

LITERATURE REVIEW

2.1 INTRODUCTION

THE performance of a wireless system heavily depends on RF PAs, whose performance criteria are dictated by aspects such as linearity, efficiency and gain. These, in turn, are determined by an effective design process, which depends on aspects such as semiconductor technology, IC packaging and thermal management, integrated circuit (IC) design, architecture, RF characterisation, and transistor device modelling [1]. The design of RF and microwave devices requires a comprehensive and accurate device characterisation [2]. These kinds of measurement have gradually been developed over the past 60 years, starting from using traditional instruments to perform the linear measurements (e.g. power meter and the spectrum analyzer) and more recently using new instruments such as the Nonlinear Vector Network Analyser (NVNA) that enables a nonlinear measurement to be

performed. A comprehensive historical study of this system and the stages of its development can be found in [3]. The NVNAs have been extended to include not only characterisation into a fixed load but also the variation of device performance with response to different load conditions, which is known as a load-pull measurement.

The work of this thesis focuses on the development of a fast nonlinear measurement system and also load-pull measurements. This chapter will first discuss the development of device characterisation and the reasons behind the adoption of nonlinear measurements. It will include a brief description of the evolution of nonlinear measurement techniques, such as passive and active load-pull. At the end of this Chapter, the key developments and trends for the optimisation and enhancement of nonlinear RF measurement systems and load-pull techniques will be summarised.

2.2 LINEAR CHARACTERISATION

The traditional techniques that had previously been used such as a parallel high impedance probe for voltage measurement and a series low impedance probe for current measurement, would not allow for accurate microwave measurement due to the significant changes in the phase behaviour of the voltage and current at high frequencies over the physical extent of the component [4–6]. Consequently, the power of travelling waves (a & b) at the measurement ports has been measured with the input and outputs terminated into a relatively constant reference impedance. The relationship between travelling waves and the voltage and current quantities is defined below [4], where a and b is the incident and the reflected wave, respectively. The subscript i indicates the port index while Z is the complex impedance and Z_o is the characteristic impedance.

$$a_i = \frac{V_i + Z_i I_i}{2 \sqrt{|Z_o|}} \qquad b_i = \frac{V_i - Z_i I_i}{2 \sqrt{|Z_o|}} \qquad (2.1)$$

This realisation led to the scattering matrix representation, otherwise known as S-parameters, to provide a complete description of the circuit network [7]. S-parameter theory is applicable to any network that has any number of ports. Due to the ease of the measurement, S-

parameters have become one of the most important methods used for transistor characterisation [6]. These parameters were first formulated by Kurokawa in 1965 to define the relationship between the travelling waves (a & b) across a network [8]. To illustrate the S-parameter relationship, the 2-port network shown in Figure 2.1 will be taken as an example.



Figure 2.1: Two port network

Due to the relationship between incident wave (a) and reflected waves (b), this network includes four S-parameters. (s_{11}) and (s_{22}) represent the input and output match, respectively. Here, (s_{21}) represents the gain/loss of the DUT, and (s_{12}) indicates the isolation factor from the output port to the input port. Equation 2.2 illustrates the relationship between these parameters.

$$\begin{bmatrix} b_1 \\ b_2 \end{bmatrix} = \begin{bmatrix} s_{11} & s_{12} \\ s_{21} & s_{22} \end{bmatrix} \begin{bmatrix} a_1 \\ a_2 \end{bmatrix} \tag{2.2}$$

These parameters are measured by the VNA within the forward and reverse measurement scenarios. The forward measurement should be performed with matched source and load impedances to ensure there is no reflection a_2 from the terminated port 2, as shown in Figure 2.2. Using this measurement, (s_{11}) and (s_{21}) can be computed using the following formulas:

$$s_{11} = \frac{b_1}{a_1} \Big|_{a_2=0} \qquad s_{21} = \frac{b_2}{a_1} \Big|_{a_2=0} \tag{2.3}$$

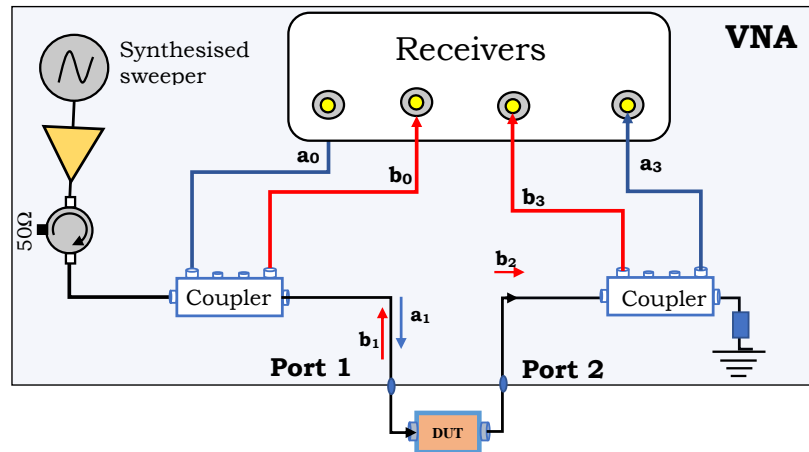


Figure 2.2: A 2-port forward VNA measurement on a DUT.

The reverse measurement should also be performed with matched source and load impedances, this time to ensure that there is no reflection a_1 from the terminated port 1 as shown in Figure 2.3. This measurement enables s_{22} and s_{12} to be computed with the following:

$$s_{22} = \frac{b_2}{a_2} \Big|_{a_1=0} \qquad s_{12} = \frac{b_1}{a_2} \Big|_{a_1=0} \qquad (2.4)$$

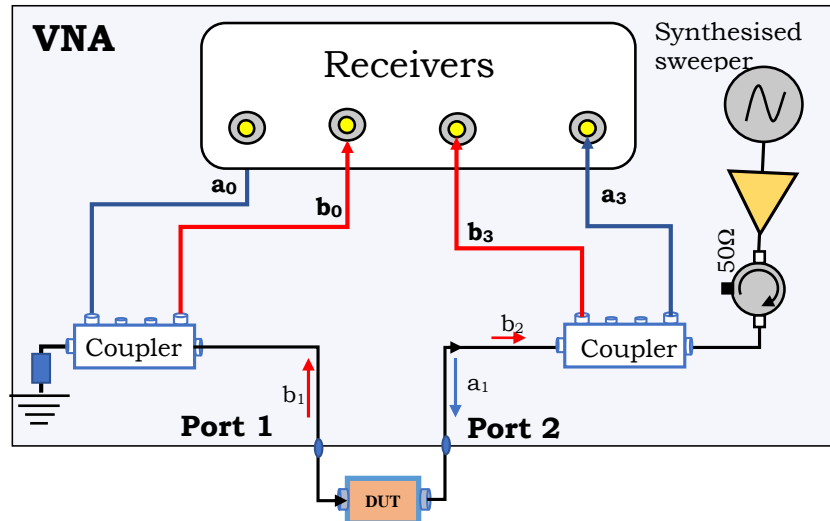


Figure 2.3: A 2-port reverse VNA measurement on a DUT.

The VNA configuration includes three main parts: signal generators, receivers, and a test-set. The signal generator injects the input signal to the DUT, while the receivers measure the incident and reflected waveforms of the DUT. Switches are sometimes used within the configuration to reduce the number of receivers and re-connect the port termination for the automated measurement of all four S-parameters.

The validity of S-parameter measurements has been proven for input signals that are relatively small [9, 10]. In other words, S-parameter measurements are only relevant when the relationship between input and output is linear. At high power levels, a significant amount of injected input power of the fundamental tone is transformed into harmonic signals. This harmonic generation causes high DC power consumption and is the direct consequence of the nonlinear behaviour of the device [11].

To describe the system nonlinearity, the harmonics must be accurately characterised. However, this kind of measurement could not be performed using the traditional VNA because it is unable to measure the phase relationship between the signal's harmonics.

2.3 NON-LINEAR CHARACTERISATION

Non-linear measurement, which is often called large signal characterisation, is performed to achieve one of three main purposes. The first purpose is to identify the optimum conditions required for a specific performance, such as load-pull measurements in which the optimum matching impedance required for high efficiency or high output power is defined [12]. The second purpose is related to device modelling, where the measurement is used for the device model generation and is utilised for the computer-aided design (CAD) software to design a RF PA [13, 14]. The third purpose is model validation, which serves the comparison between the simulated and the performance of the fabricated device. This require measurement of magnitude and phase of the fundamental and harmonic components, in addition to the phase relation between harmonics. These requirements have been achieved using different techniques that have been developed gradually during the last 40 years and will be detailed in the following section.

2.3.1 EVOLUTION OF NON-LINEAR MEASUREMENT SYSTEMS

Traditionally, spectrum analysers were used to measure the fundamental and harmonic signals generated by a DUT as its large bandwidth allowed for the measurement of the fundamental and harmonic contents. The absence of phase information of the measured signal reduces the applicability of characterising the nonlinearity of the DUT.

Oscilloscopes were used by Sipila et al. in 1988 to measure the high-frequency time-domain waveforms of a nonlinear microwave PA [15]. In this approach, the measured time domain waveforms were converted to the frequency domain using Fast Fourier Transform (FFT). This conversion is performed to allow for applying calibration error coefficients on the frequency domain components, since it can not be applied on the time domain waveforms. The frequency domain is then converted back to an accurate time domain waveform. However, the limitations of the oscilloscope's sampling rate would introduce a frequency range constraint, which is considered to be the main drawback of this approach.

The integration of the existing VNAs and a harmonic phase reference (HPR) was presented by Lott in 1989 [16]. This measurement setup allowed for waveform reconstruction as it captures the phase relationship between measured harmonics [17]. The adopted HPR technique was performed using either a diode circuit or additional signal generator and receiver to generate a full spectrum signal with a known phase offset between these different harmonics. However, using an additional generator and receiver increases the cost and the complexity of the system. Meanwhile, the use of the diode unfortunately introduced inaccuracies within phase reference measurements that resulted in incoherent phase differences between measured harmonics.

Several attempts have been made to improve nonlinear measurement systems [18–23]. One of those examples utilised the Microwave Transition Analyzer (MTA) by Demmler et al. in 1994 [24]. The MTA was introduced by Hewlett Packard company as a dual channel sampling oscilloscope with a dynamic range of 60 dB, which was able to measure magnitudes and phases of pulsed-RF signals with carrier frequencies from DC up to 40 GHz. Figure 2.4 shows how the MTA is combined with a test-set and synthesiser to measure magnitudes and phases of the fundamental and harmonic signals, hence allowing for the measurement of waveforms. This kind of measurement setup is also

referred as a Nonlinear Vector Network Analyser (NVNA), even though its fundamental mode of operation being based on signal sampling.

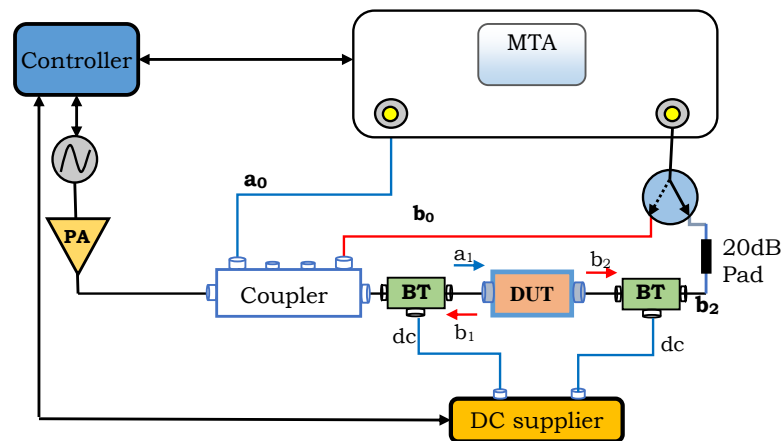


Figure 2.4: Generic block diagram of the nonlinear vector network analyser based on MTA

There are now several instruments and measurement techniques that have been developed for nonlinear measurement, such as the PNA-X (Phase Network Analyzer-X Parameter) from Keysight, with which harmonics can be captured. Another example is the ZVA (Z Vector Analyzer) from R&S (Rhode and Schwartz). However, many engineers are working to develop and improve these instruments for high accuracy and speed.

2.3.2 NVNA CALIBRATION

To provide accurate data, a calibration procedure has to be performed for all measurement systems that operate at RF and microwave frequencies. This is due systematic errors that are encountered by the RF-signals while passing through each non-ideal element of the system, such as couplers and cables [19]. These errors consist of six types: source and load impedance mismatches relating to reflections, crosstalk and directivity errors relating to signal leakage and frequency response errors caused by reflection and transmission tracking within the test receivers. Figure 2.5 illustrates systematics error of the two-port network.

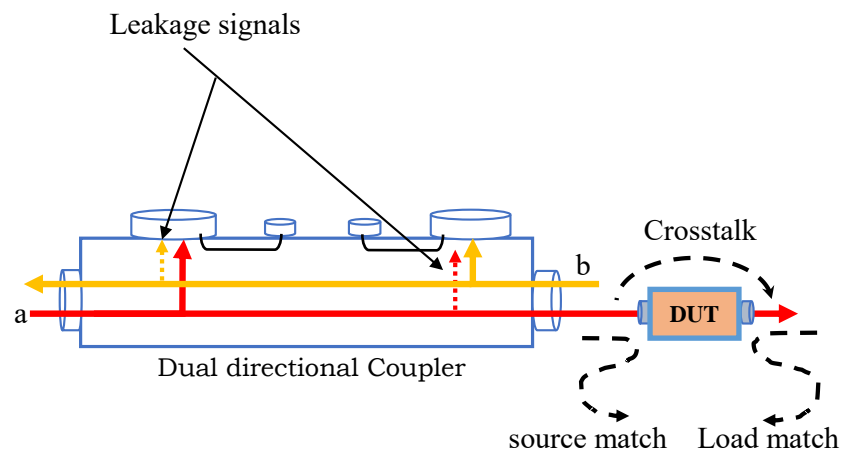


Figure 2.5: Systematic error of the two-port network

There are another two kinds of error that have impact on the RF signal; random errors and drift errors [25]. The main factors that cause the random errors are instrument noise (the IF noise floor and sampler noise), connector repeatability and switch repeatability. When using network analysers, noise errors can usually be decreased by increasing source power, by using trace averaging over multiple sweeps, or by narrowing the IF bandwidth. Thermal drift, which is the primary cause for drift error, should be monitored even if the instrument has good thermal stability, which are mainly caused by deviation in temperature and can be minimized by controlling the environment. Any errors that are not invariant with time are systematic errors and can be removed through a calibration process.

Calibration is the process of obtaining the error correction coefficients, which is achieved by measuring known standards to remove effects from subsequent measurements. A typical calibration requires several standards to determine error coefficients. The type of algorithm used in calibration determines the choice of the calibration standards. There are many types of calibration algorithms such as SOLT, TRL, etc [26–28].

Because it is impractical or impossible to obtain highly accurate calibration standards, especially on wafer, TRL calibration algorithm is generally used for on wafer measurements [29]. This because it depends on mathematical process to characterise the error box and is not on a model created by default from manufacturer that can be affected by many factors. The two-port error model of TRL calibration consists of two error-flow models: forward, when the RF signal is applied to port-1 (as shown in Figure 2.6a); and reverse, when RF signal is applied to port-2 (as shown in Figure 2.6b [22]).

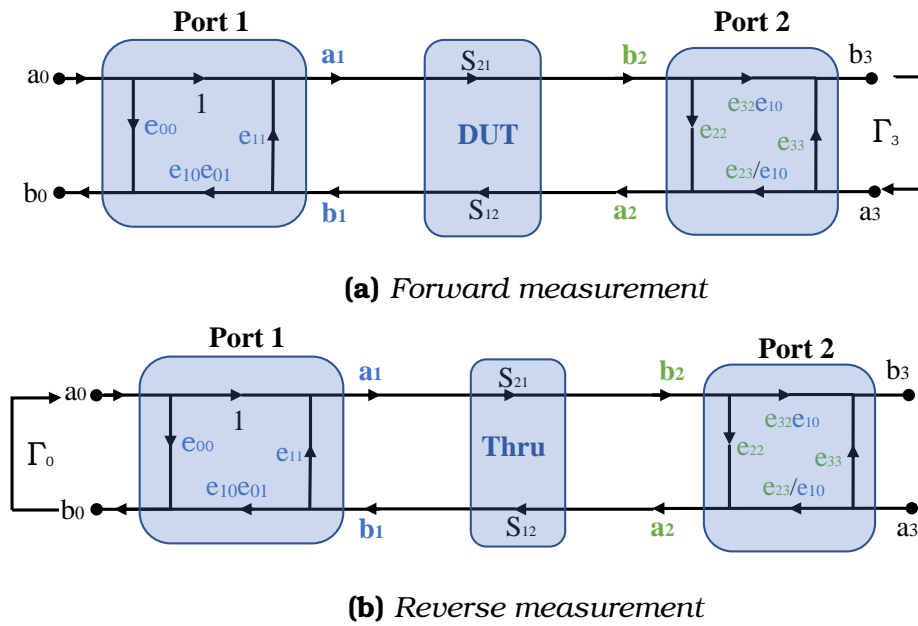


Figure 2.6: Error model of the small signal calibration.

As can be seen in Figure 2.6, this calibration method can provide the directivity errors (e_{00}, e_{33}), port mismatch errors (e_{11}, e_{22}), the reflec-

tion error ($e_{10}e_{01}$), transmission error ($e_{10}e_{32}$), and the tracking errors ($e_{23}e_{32}$, $e_{23}e_{01}$)[30, 22].

The drawback of this kind of calibration procedure is that they rely on S-parameters, which are defined as travelling wave ratios. Consequently, only relative measurements are performed and the absolute phase and power associated with incoming and outgoing waves remain undetermined. However, this ambiguity of the vector information would not allow for voltage and current waveform reconstruction at the terminals of the DUT. This is also the reason why some error terms cannot be determined separately. This restriction has been eliminated by extending the calibration procedure through a further calibration step, known as a large signal calibration (as shown in Figure 2.7 and 2.8 detailed in [22]).

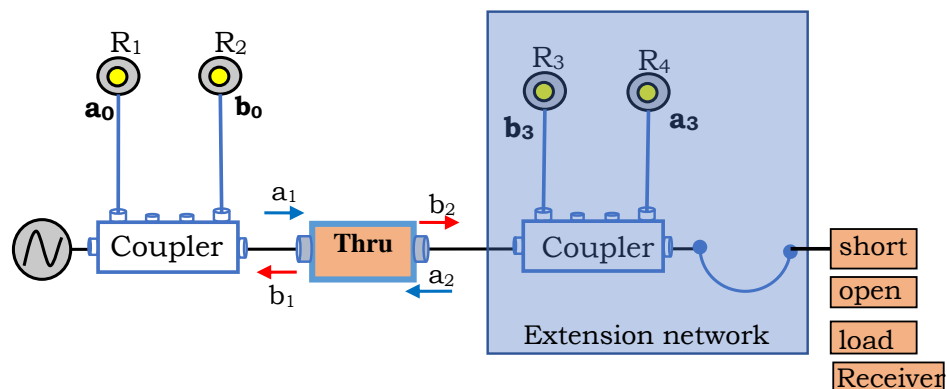


Figure 2.7: Configuration of the measurement setup during the extended calibration.

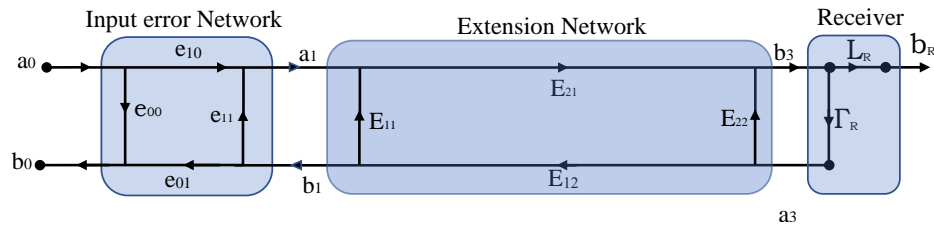


Figure 2.8: Error model of the extension calibration.

Here, an extension network is determined through the measurement of three calibration standards, giving s_{11} , $s_{21}s_{12}$ and s_{22} s-parameter terms. Because the extension network is symmetrical, the combined $s_{21}s_{12}$ term can be split into two parameters with equal magnitude and phase. During a fourth measurement, the extension network is connected to one receiver and the thru-response is measured. Because the extension network is known, its effect on the thru-measurement can be removed with e_{10} as the only remaining term, which can then be used to determine the individual error terms from the aforementioned products $e_{10}e_{01}$, $e_{10}e_{32}$ and $e_{10}e_{32}$. Performing the extended calibration allows us to measure the absolute magnitude and phase of the travelling waves at the measurement reference plane by determining the scaling parameter e_{10} .

2.4 LOAD-PULL MEASUREMENT

Load-pull is an essential element for nonlinear measurements, where the load termination of a DUT is varied to define the optimum load impedance. This technique was originally suggested by D. M. Snider in 1967 to investigate the variation of the DUT performance with response to different load conditions [31]. It ensures that an appropriate termination at the transistor output is achieved [32]. Defining the optimum impedance of a transistor is crucial to delivering optimal performance, such as high efficiency, gain, linearity and output power, and also providing a clear understanding of various modes of amplifier operation [11]. However, the load termination has to be controlled precisely for an exact definition of the impedance during measurements. Two fundamentally different concepts have been developed for the implementation of a load-pull system: passive and active load-pull.

2.4.1 PASSIVE LOAD-PULL MEASUREMENTS

The passive load-pull approach uses two different techniques to present the required reflection coefficient at the DUT ports, either by using electromechanical tuners (EMTs) or electronic tuners (ETSs) [14]. The EMT technique uses probes that move horizontally and vertically [33]. This movement represents the magnitude and phase of the reflected signal. Changing the probe along the vertical direction changes the magnitude of the reflection coefficient, while changing the tuner along the horizontal line causes the phase variation of the reflection coefficient.

The ETS technique employs electronic circuits such as PIN diodes, in which the termination changes electronically [34]. These diodes are connected in parallel and distributed in a precise manner along a transmission line. The desired load target is achieved by varying the impedance state of the PIN diodes and their location. This technique is limited by the number of load states which equal 2^N , where N is the number of diodes as there are two states of a diode. This led to the use of a cascade of ETSs to increase impedance resolution. Consequently, high loss in the reflected signal is introduced, which translates into

max Gamma ranging between $\Gamma_L = 0.8$ and $\Gamma_L = 0.92$ at the DUT's reference plane.

For passive harmonic load-pull, cascaded tuners can be connected in series. This configuration allows for more complexity and loss, in addition to the difficulty of controlling harmonics independently because any change occurring within one of the tuners influences the impedance of the other tuner. To solve this problem, triplexers with independent tuners have been used (as shown in Figure 2.9).

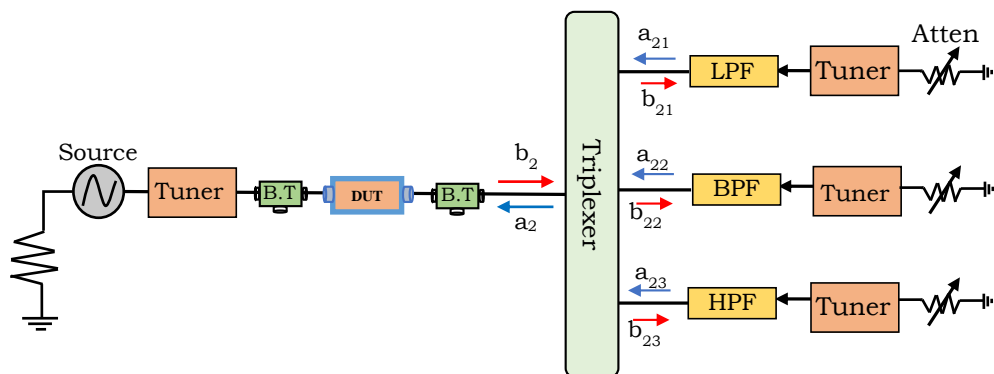


Figure 2.9: Generic system configuration of the passive harmonic load-pull

This facilitates independent fundamental and harmonic load-pull tuning [5]. The need for the triplexer to separate the harmonic signals allowed for the high insertion loss problem; however, it causes a limitation of the required injected signal [35]. To partially overcome

this problem, high reflection harmonic tuners have to be used and this results in the high cost of the implementation.

In conclusion, the passive load-pull approach suffers from several problems, including an inability to present a high reflection coefficient and the complexity of the system configuration [36]. In addition, EMT systems suffer from the relatively slow speed at which the impedances can be varied due to their mechanical nature. This is in contrast to the need for high load reflection coefficients at harmonics frequencies during the characterisation of high-power transistors, which requires impedances close to the edge of the Smith chart for their optimum performance [37, 38].

2.4.2 ACTIVE LOAD-PULL MEASUREMENTS

The shortcomings of the passive load-pull approach have motivated researchers to find alternative measurement system techniques and architectures, which led to the development of the active load-pull technique. In this technique, the reflection coefficient is synthesised electronically by injecting a signal (a_2) signal into the output of the DUT. The a_2 is computed according to the Equation 2.5, where the Γ is the load targeted and (b_2) is the associated DUT's response.

$$\Gamma = \frac{a_2}{b_2} \quad (2.5)$$

Based on the generation method of the injected signal, the active load-pull technique is divided into two categories: closed-loop and open-loop active load-pull.

2.4.2.1 CLOSED-LOOP ACTIVE LOAD-PULL

There are three basic techniques for the realisation of closed-loop active load-pull configurations: feedforward load-pull and feedback load-pull. The third alternative technique for achieving closed-loop

load-pull has been realised more recently and is called active “envelope load-pull” (ELP).

FEED-FORWARD ACTIVE LOAD-PULL

This load-pull technique was presented by Takayama in 1976 [39]. As shown in Figure 2.10, a splitter is used to divide the incident signal into two parts, by which there is no need for another signal generator. The DUT is fed by the first part while the second part is used for the load emulation loop, which includes a phase shifter, attenuator, and power amplifier to synthesise the desired reflection coefficient. Harmonic load-pull has been extended by Ghannouchi et al. [40].

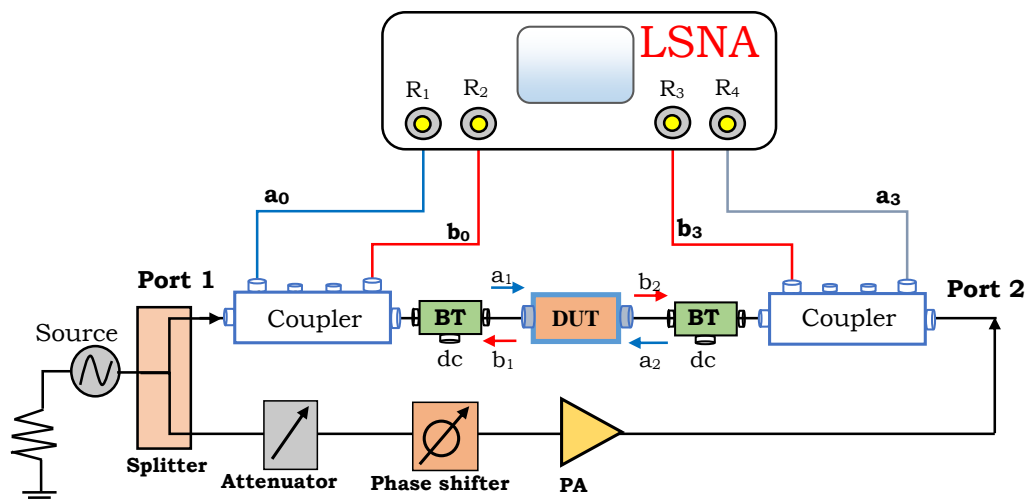


Figure 2.10: Feed-Forward Active Load-Pull System

To achieve waveform measurement, Benedikt et al. [41] presented a combination of vector corrected waveform measurements with active harmonic load-pull based on two channels MTA. Figure 2.11 shows a generic block diagram of this approach. Frequency multipliers and splitters are used here to generate the three harmonics injected signal a_{21} , a_{22} and a_{23} . These signals are adjusted by using the attenuator and phase shifter to achieve a load target while a triplexer component is used to combine the three harmonic signals to be injected into the DUT. It is clear that the synthesised reflection coefficients are dependent on the source signal and the signal modulation of the load-pull loop.

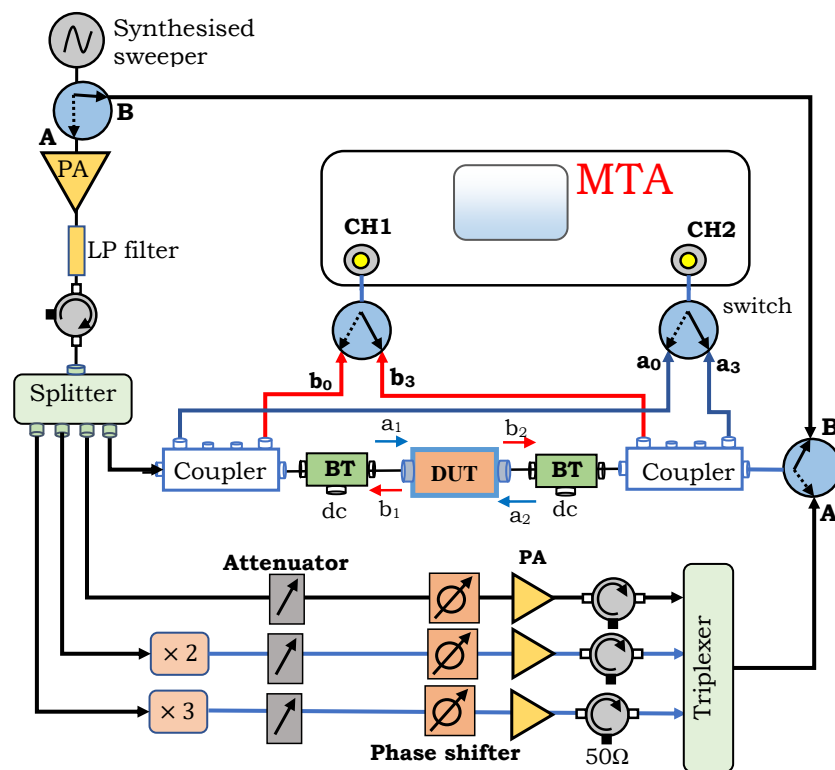


Figure 2.11: Schematic of the two-port time-domain load-pull system

This dependency makes the reflection coefficient of this active load-pull unpredictable and, hence, many iterations are needed to converge on a target load. Moreover, the unconditional stability of the DUT during the measurement might not be achievable when complex loop gains approach extremely high values [14].

An advanced configuration of feedforward active load-pull has been presented by Thorsell et al. [42], which is based on large-signal network analyser (LSNA) and digitally controlled vector modulators (as shown in Figure 2.12).

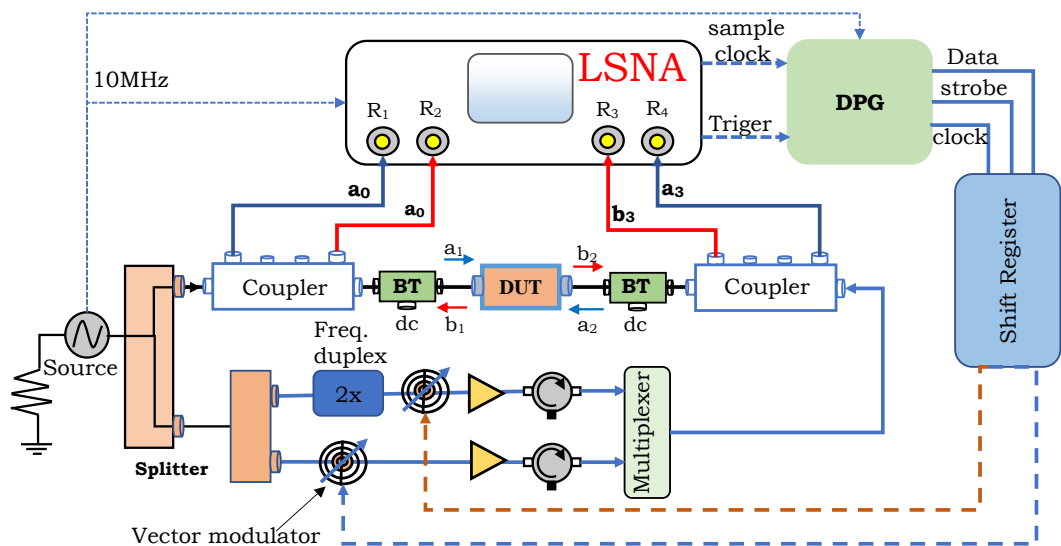


Figure 2.12: LSNA based multi-harmonic active load-pull system configuration

The LSNA was used to measure time-varying periodic signals while the time alignment between LSNA and the vector modulator is achieved

by using a 16-bit digital pattern generator (DPG). An oscilloscope and current probe were used to measure the time-varying bias current and, hence, reconstruct the voltage and current waveforms. The Newton Raphson algorithm has been used to adjust the vector modulator setting to emulate the desired fundamental and second harmonic loads [43].

In spite of high number of measurements that can be performed by this system, which approach 180 load states per 20 ms, this load-pull system does have some drawbacks. The complexity of the system's configuration is relatively high, which makes it difficult for compact realisation. Moreover, each load-pull measurement requires an extra two measurements due to the use of the Newton Raphson algorithm, which increases the number of states during each measurement by a factor of $2n+1$. Furthermore, the correct signal out of the vector modulator required five iterations to converge on a solution.

FEED-BACK ACTIVE LOAD-PULL

The feed-back active load-pull technique was introduced in the 1980s [44]. The emulation of the desired load is achieved by exploiting the DUT's output signal (b_2). Within this kind of load-pull measurement,

the phase and magnitude of the (b_2) signal are modified by an attenuator and phase shifter to emulate the desired load reflection coefficient through a complex feedback loop (as shown in Figure 2.13).

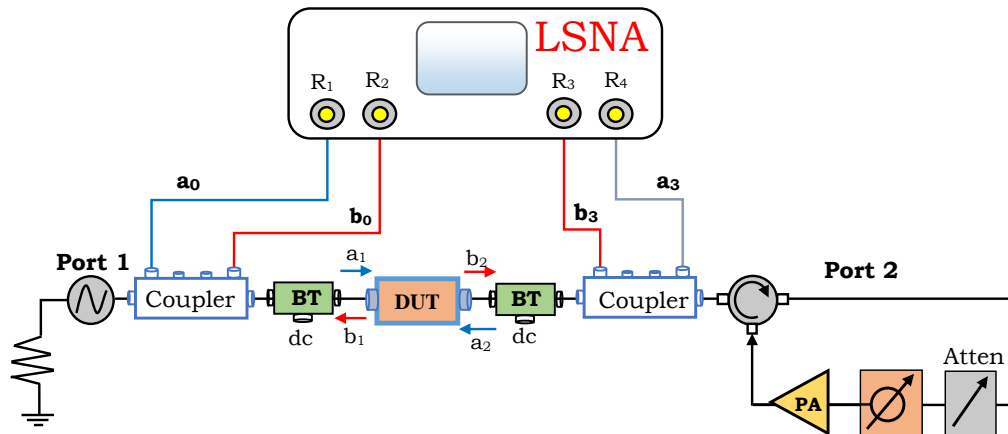


Figure 2.13: *Generic block diagram of feedback active load-pull architecture.*

Compared to the passive load-pull approach, this technique facilitates a faster characterisation process due to the availability of electronically tunable attenuators and phase shifters.

However, this technique is considered to be prone to oscillation because the loop gain cannot be selectively controlled over frequency [45] and, consequently, significant filtering is typically employed to reduce the risk of oscillation. Therefore, it is considered to be more suitable for small signal devices, where low power and relatively low load reflections are required and, hence, making oscillations less likely.

The envelope load-pull measurement system is shown in Figure 2.14 [46]. This measurement setup is in principle a variant of the feedback closed-loop active load-pull.

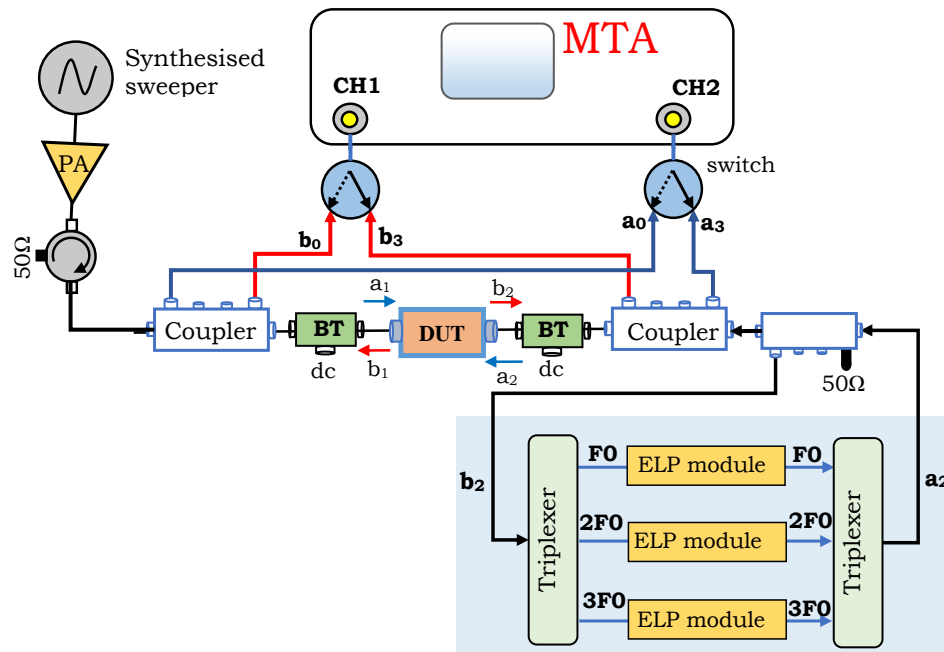


Figure 2.14: *ELP based load-pull measurement system*

The key difference is that the control loop is operating at the envelope frequency of the signal and not the RF signal. The reduction of the frequency allows digital signal processing to be employed and, therefore, it enables a precise control over the entire range of frequencies within the first Nyquist zone.

The ELP architecture is shown in Figure 2.15, where the signal is down-converted to an intermediate frequency using an I/Q demodulator and

is then manipulated to meet the required load through the use of a circuit with transfer function $F(x,y)$.

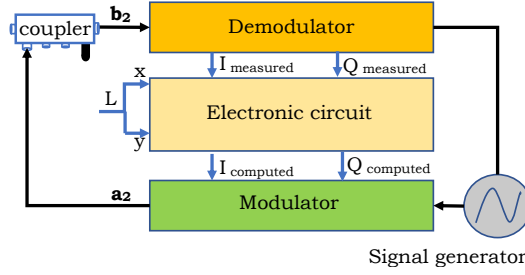


Figure 2.15: Control unit of the ELP system

The transfer function is used to compute the required injected signal to emulate the desired load ($\Gamma_{required}$) according to Equation 2.6 and 2.7.

$$\Gamma_{required} = \frac{(X + JY)_{setting}}{(X + JY)_{measured}} \quad (2.6)$$

$$(X + JY)_{setting} = \Gamma_{required} \times (X + JY)_{measured} \quad (2.7)$$

The computed signal is then up-converted by a quadrature modulator and fed back to the DUT output port.

The problem of presenting inaccurate loads by this approach has been solved by Hashmi et al. [47], where advanced hardware within the configuration were utilized that allowed for a new calibration technique to be implemented on the system. However, this approach requires multiple measurements to precalibrate the ELP loop, which consumes

more time before load-pull measurements can be carried out. This system achieved 36 measurements within 18 minutes; that is, 2 per minute.

The digital control of the TxRx (transmitter and receiver) with an on-board FPGA has been presented by Williams et al. [48]. This technique was used to improve the measurement speed. Due to the on-board FPGA and the broad bandwidth of the PXIe module, the speed of the measurement has been improved to 2 to 3 measurements per sec.

2.4.2.2 OPEN LOOP ACTIVE LOAD-PULL

The open-loop active load-pull method has been presented to overcome the stability and oscillation issues that were encountered in closed loop active load-pull systems [49, 50]. Indeed, this method ensures the possibility of presenting any load impedance at the fundamental frequency, including higher order harmonics with full Smith chart coverage. The open loop architecture is very similar to the setup of the feedforward closed-loop active load-pull, the key difference is the use of a signal generator to emulate the required impedance instead of splitting the input signal.

Figure 2.16 shows the measurement system setup of the open loop active load-pull that been demonstrated by Williams et al. [49], which is based on two-channel HP-MTA. This measurement setup allows us to perform source and load-pull measurement using programmable electronic signal generators (ESG) within a frequency range of 800MHz to 2GHz. The generators can be controlled individually for phase and magnitude using a GBIP bus. This property allows us to synthesise a target load without the need to use attenuators and phase shifters. The measured waveform is used to compute the injected signal required to emulate a specific load target.

This approach eliminated the time required to adjust the traditional load-pull components (attenuator and phase shifters). However, the nonlinearity of the DUT has made the prediction of the required injected signal challenging to achieved, in which several iterations were desired.

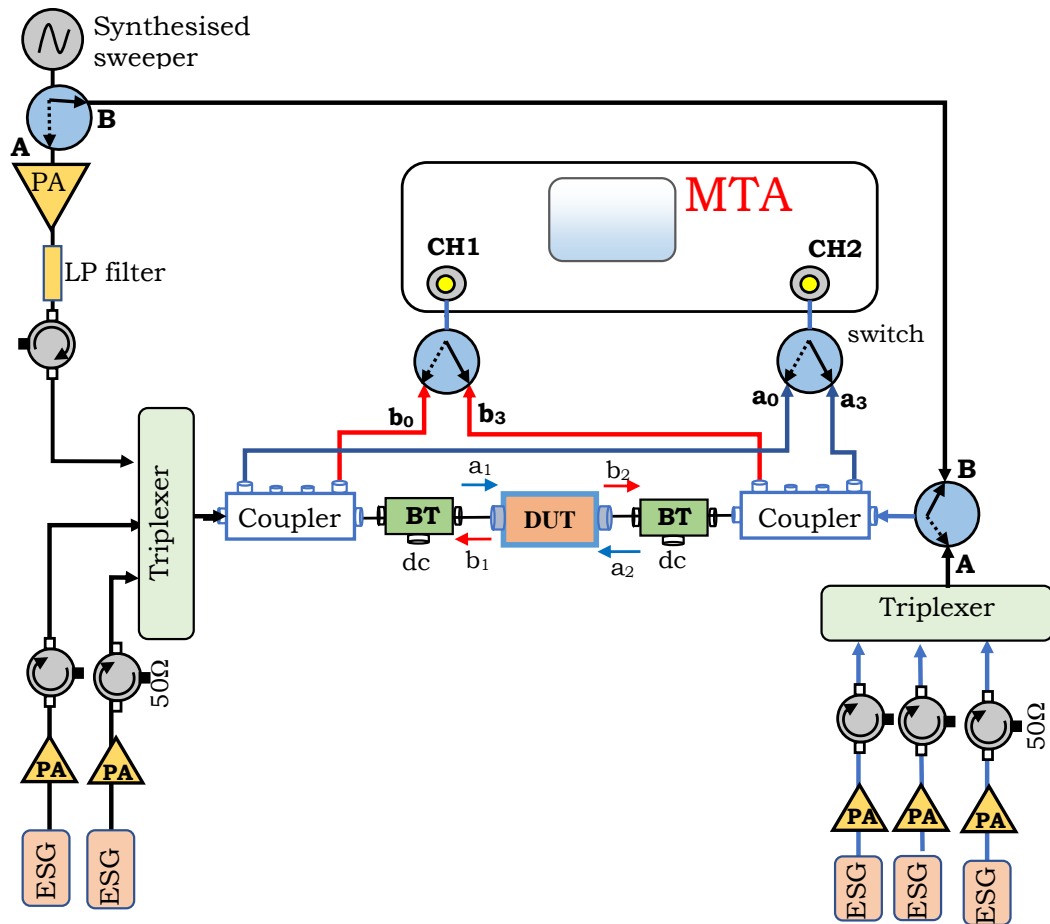


Figure 2.16: Generic digram of the open loop active harmonic load-pull configuration using two channel MTA.

Generally speaking, this process is considered to be relatively time- and computationally-expensive because it requires a combination of multiple processes, such as computation of the required injected signal for a load target and employing adjustment of the generated signal. Consequently, an iteration process is required to find the optimal injection signals to offer the desired reflection coefficients to the DUT [30].

Trends toward enhancing and developing the opened-loop active load-pull technique have continued and have progressed gradually towards shortening the time consumed during the measurement process and increasing throughput. Consequently, new measurement setups and new strategies have been used to achieve an effective measurement system.

The system configuration from Anteverta is shown in Figure 2.17 [51, 52]. Within this system, the reflection coefficients are synthesised by injecting signals into the DUT. These signals are generated by base-band arbitrary waveform generators (AWG) with 80MHz bandwidth then up-converted using in-phase/quadrature (IQ) modulators. All the AWGs and the A/D converters, which have a 45MHz bandwidth, are integrated in a PXI express platform and share the same time-base. The local oscillator signal, which drives the IQ mixers for the frequency up-conversion of the baseband signals, was obtained from a single RF source and is independent from the PXIe chassis reference signalling. Frequency multipliers are used to obtain the LO signals that drive the IQ mixers to generate the second harmonic signal. Moreover, an external shared LO, which is also independent of the PXIe chassis, is used for the frequency down-conversion after the signal is separated

into its harmonic components using power splitters and high-pass filters.

Using a mixed-signal IQ generation system allows for modulated signals to be used and, hence, the emulation of multiple load states within a single measurement cycle. This system can perform about 25 measurements per second and require about 16 seconds to set the values for source and load reflection coefficients [53].

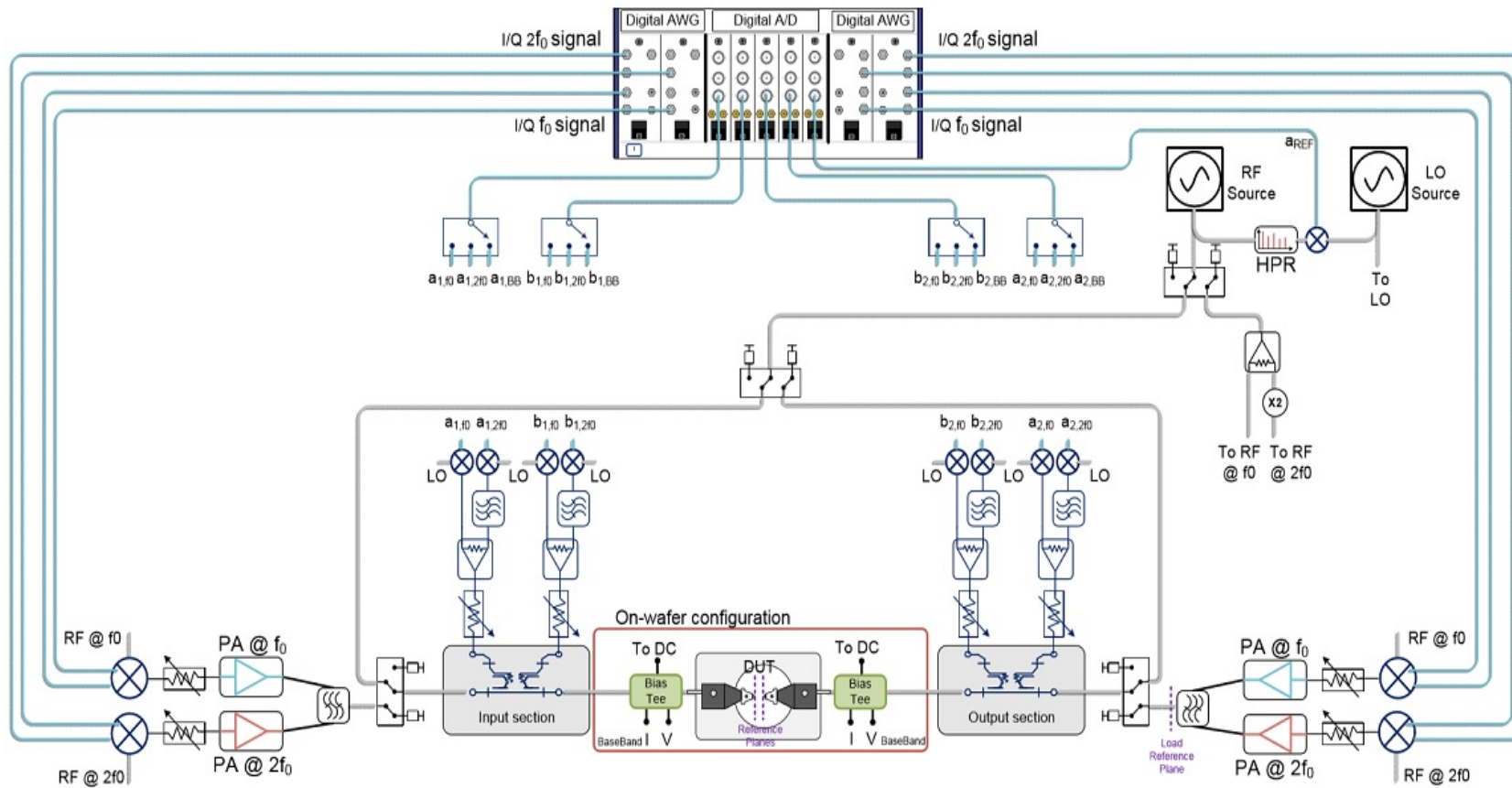


Figure 2.17: Open loop active load-pull system configuration by Antiverta [53]

2.4.2.3 BEHAVIOURAL-MODEL DRIVEN LOAD-PULL

Few previous studies have utilised the behavioural model to predict the desired injected signal to emulate a load target at the device reference plane. Utilizing such approach would allow for reducing the required number of iterations. For example, Robert et al. in [54] exploited locally generated poly-harmonic distortion (PHD) models to facilitate a reliable strategy for the determination of the optimum load and source termination. The proposed strategy consumed about 16 minutes to define the required termination for highest efficiency. This is due to the time consumption during the acquisition of the information, which is about 5 sec for a single state.

In another example, Saini et al. [55] utilised the linear third order mixing terms of the Cardiff behavioural model in Equation 2.8 to drive the opened-loop active load-pull system.

$$b_{2h} = K_{2,0,h} + K_{2,0,h} |a_{21}| \left(\frac{Q}{P} \right) + K_{2,-1,h} |a_{21}| \left(\frac{P}{Q} \right) \quad (2.8)$$

Thanks to the predictivity feature of the model and the load emulation nature during the opened-loop active load-pull, the model was able to locally predict the device response and, hence, compute the desired

injected signal to emulate a load target with the substitute Equation 2.8 in 2.9.

$$\Gamma_h = \frac{a_{2h}}{b_{2h}(a_{21}, a_{22}, \dots, a_{2h})} \tag{2.9}$$

The measurement was carried out using an automated open loop active load-pull system, which was developed at Cardiff University, with a four-channel Tektronix oscilloscope (as illustrated in Figure 2.18).

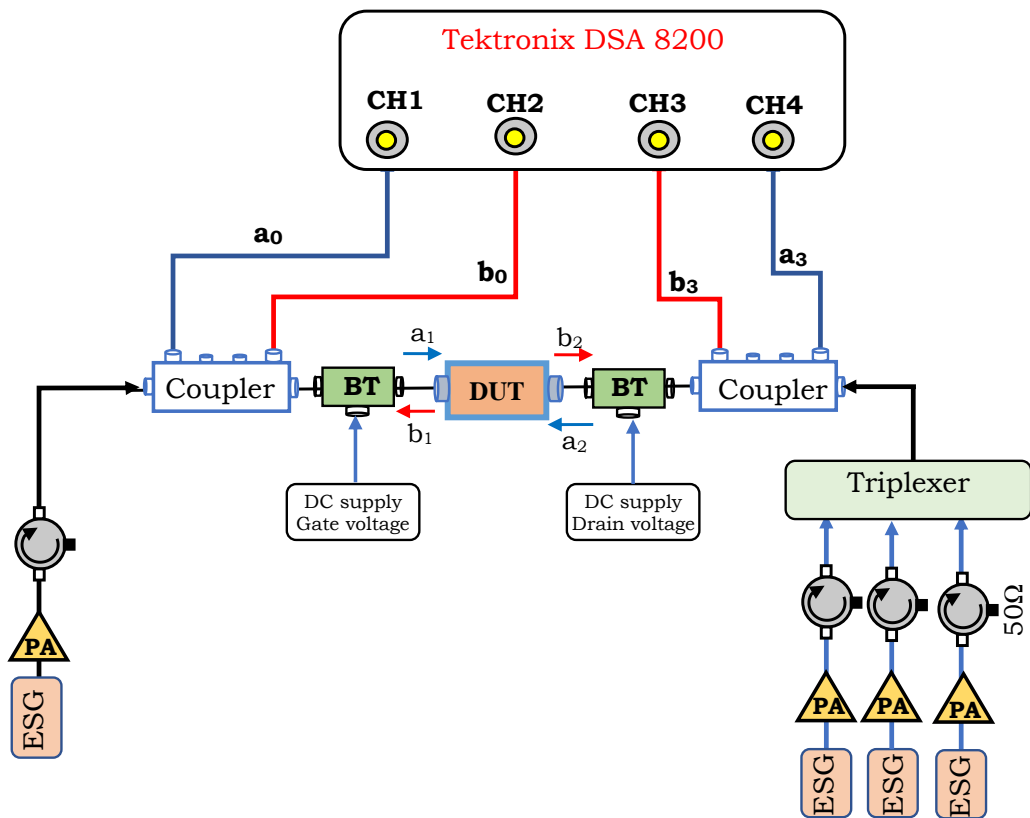


Figure 2.18: Generic diagram of the open loop active harmonic load-pull system.

To achieve a specific load target, a single, starting load-pull measurement followed by two offset measurements were required to generate a local model. The generated model was then utilised to predict the required injected signal to emulate the load target. A significant reduction of the number of iterations has been achieved by using this approach. The result shows that only 78 extra measurements were required to perform an example of 700 fundamental load impedances. These extra measurements were required for the model extraction and iterations. It is worth mentioning here that the time taken for this measurement was about 30 seconds per single load-pull measurement i.e 6.4 hours for the whole measurement. Moreover, the load-targeting on the Smith chart was around the optimum impedance, which had already been assigned before the measurements were conducted. Therefore, one of the objectives of this thesis will be to automatically define the optimum impedance of an unknown DUT.

2.5 CHAPTER SUMMARY

In conclusion, this chapter discusses the evolution of RF-measurement techniques, starting with the small-signal measurement using the VNA and progressing to the introduction of the NVNA for the large signal measurement, which was seen to be a large development in terms of the calibration and the measurement techniques. Given that load-pull measurement techniques are of key importance for nonlinear measurements, this has been an active area for further development in terms of execution speed, measurement accuracy, measurement strategies, and load-pull techniques.

Impedance tuners, or passive load-pull, are the dominant and mature load-pull technology and they are considered to be a key enabler in RFPA design. However, this approach has several well-known drawbacks.

Consequently, the closed loop active load-pull techniques, such as feedforward and feed backward closed loop systems, have been developed to overcome some of the shortcomings of the passive load-pull. Some of the advantages are speed, control of load impedances, and ease of integration into on-wafer measurement systems. The draw-

backs include potential instabilities and oscillations. Furthermore, the filtering that is used to address this issue results in a system that is rather narrowband.

These problems have been overcome by using open-loop active load-pull, where an independent software-controlled vector signal generator is utilised. This technique has eliminated the hardware-related oscillations. This is an iterative process because the injected signal is continually adjusted until the required impedance is obtained. However, these procedures slow down the load-pull process and increase the complexity of operating it.

The important trends of optimising the active load-pull measurement were discussed in this chapter. It was found that most of them were made to reduce the number of iterations or maximise the load-pull measurement speed, either by optimising the raw measurement speed or using suitable measurement strategies that reduce the need for iterations. Table 2.1 summarises and compares the important and relevant achievements and milestone load-pull measurement system.

Table 2.1: A summary and comparison of the important and relevant achievements of the load-pull measurement

LP ststem	LP category	Config. nature	System's setup	Signal inst. BW	Time-domain waveforms	Time-domain dynamic range	Number of Iterations	Convergence approach	LP measur. speed
A [53]	Passive Tuner	–	Power meter	+	No	-	Low	n/a	1/sec
B [56]	Passive-hybrid	–	VNA/NVNA	++	No/Yes	-/++	Low	n/a	15/sec
C [55]	Active	Opened Loop	4-Channel Oscilloscope	+	Yes	+	High	Behavioral, localised, low order	1.5/min
D [48]	Active	Closed loop-ELP	PXIe baseband + VNA/NVNA	++	No/Yes	-/++	High	Numerical iterations	2-3/sec
E [51]	Active	Opened Loop	PXIe baseband system	++	Yes	++	High	Numerical iterations	25/sec
F [57]	Active	Closed loop-Feedforward	LSNA	+	Yes	++	Medium	Numerical iterations	?

In conclusion, the key requirements of an unrestricted coverage for the Smith chart and stability under all load conditions favour the open-loop active load-pull system. Its limitations, as reported previously, are often due to the relatively low speed of the measurement unit and the need for iterations. Consequently, any further evolution of active load-pull systems should focus on these two limiting factors.

REFERENCES

- [1] A. Raghavan, N. Srirattana, and J. Laskar, *Modeling and Design Techniques for RF Power Amplifiers*. Wiley-IEEE Press, 2008.
- [2] C. Poole and I. Darwazeh, *Microwave Active Circuit Analysis and Design*. Academic Press, 2015.
- [3] D. Rytting, "ARFTG 50 year network analyzer history," in *71st ARFTG Microwave Measurement Conference*, June 2008, pp. 1–8.
- [4] D. M. Pozar, *Microwave Engineering*. John Wiley & Sons, 2011.
- [5] V. Teppati, A. Ferrero, and M. Sayed, *Modern RF and Microwave Measurement Techniques*, V. Teppati, A. Ferrero, and M. Sayed, Eds. Cambridge University Press, 2009.
- [6] H.-P. Test, "Measurement application note 95-1, s-parameter techniques for faster, more accurate network design," 1997.
- [7] F. Giannini and G. Leuzzi, *Nonlinear Microwave Circuit Design*. John Wiley & Sons, 2004.
- [8] K. Kurokawa, "Power waves and the scattering matrix," *IEEE Trans. Microw. Theory Techn.*, vol. 13, no. 2, pp. 194–202, March 1965.
- [9] R. J. Chaffin and W. H. Leighton, "Large-signal s-parameter characterization of UHF power transistors," in *IEEE G-MTT International Microwave Symposium*, June 1973, pp. 155–158.
- [10] W. H. Leighton, R. J. Chaffin, and J. G. Webb, "Rf amplifier design with large-signal s-parameters," *IEEE Trans. Microw. Theory Techn.*, vol. 21, no. 12, pp. 809–814, Dec. 1973.
- [11] S. C. Cripps, *RF Power Amplifiers for Wireless Communications*, 2nd ed. Norwood, MA: Artech House, 2006.
- [12] P. Aaen, J. A. Plá, and J. Wood, *Modeling and Characterization of RF and Microwave Power FETs*. Cambridge University Press, 2007.
- [13] B. Noori, P. Aaen, D. Abdo, and P. Hart, "The RF Power Behind Design Innovation," (2007). [Online]. Available from: <https://pdfs.semanticscholar.org/ca4e/2070feb6d6cfc614a626f9e94f09b33397dc.pdf>, accessed: 2018-10-12.

- [14] F. M. Ghannouchi and M. S. Hashmi, *Load-Pull Techniques with Applications to Power Amplifier Design*. Springer, 2013.
- [15] M. Sipila, K. Lehtinen, and V. Porra, "High-frequency periodic time-domain waveform measurement system," *IEEE Trans. Microw. Theory Techn.*, vol. 36, no. 10, pp. 1397–1405, Oct. 1988.
- [16] U. Lott, "Measurement of magnitude and phase of harmonics generated in nonlinear microwave two-ports," *IEEE Trans. Microw. Theory Techn.*, vol. 37, no. 10, pp. 1506–1511, Oct. 1989.
- [17] J. Verspecht, "Large-signal network analysis," *IEEE Microwave Magazine*, vol. 6, no. 4, pp. 82–92, Dec. 2005.
- [18] F. van Raay and G. Kompa, "A new on-wafer large-signal waveform measurement system with 40 GHz harmonic bandwidth," in *IEEE MTT-S International Microwave Symposium Digest*, June 1992, pp. 1435–1438 vol.3.
- [19] T. V. den Broeck and J. Verspecht, "Calibrated vectorial nonlinear-network analyzers," in *IEEE MTT-S International Microwave Symposium Digest*, May 1994, pp. 1069–1072 vol.2.
- [20] M. Demmler and P. J. Tasker, "A vector corrected on-wafer large-signal waveform system for novel characterization and nonlinear modeling techniques for transistors," in *workshop on New Direction in Nonlinear RF and Microwave Characterization, IEEE International Microwave Symposium*, 1996.
- [21] C. J. Clark, G. Chrisikos, M. S. Muha, A. A. Moulthrop, and C. P. Silva, "Time-domain envelope measurement technique with application to wideband power amplifier modeling," *IEEE Trans. Microw. Theory Techn.*, vol. 46, no. 12, pp. 2531–2540, Dec. 1998.
- [22] J. Benedikt, R. Gaddi, P. J. Tasker, and M. Goss, "High-power time-domain measurement system with active harmonic load-pull for high-efficiency base-station amplifier design," *IEEE Trans. Microw. Theory Techn.*, vol. 48, no. 12, pp. 2617–2624, Dec. 2000.
- [23] D. J. Williams, J. Leckey, and P. J. Tasker, "Envelope domain analysis of measured time domain voltage and current waveforms provide for improved understanding of factors effecting linearity," in *IEEE MTT-S International Microwave Symposium Digest*, vol. 2, June 2003, pp. 1411–1414 vol.2.

- [24] M. Demmler, P. J. Tasker, and M. Schlechtweg, "A vector corrected high power on-wafer measurement system with a frequency range for the higher harmonics up to 40 GHz," in *24th European Microwave Conference*, vol. 2, Sep. 1994, pp. 1367–1372.
- [25] D. K. Rytting, "Network analyzer accuracy overview," in *58th ARFTG Conference Digest*, vol. 40, Nov. 2001, pp. 1–13.
- [26] S. Rehnmark, "On the calibration process of automatic network analyzer systems (short papers)," *IEEE Trans. Microw. Theory Techn.*, vol. 22, no. 4, pp. 457–458, April 1974.
- [27] G. F. Engen and C. A. Hoer, "Thru-reflect-line: An improved technique for calibrating the dual six-port automatic network analyzer," *IEEE Trans. Microw. Theory Techn.*, vol. 27, no. 12, pp. 987–993, Dec. 1979.
- [28] Y. Liu, Y. Tian, B. Gao, and L. Tong, "An improved method for trl calibration," in *International Conference on Microwave and Millimeter Wave Technology*, May 2010, pp. 696–698.
- [29] M. B. Jenner and T. E. Kolding, "Test structures and techniques for on-wafer cmos trl calibration," in *IEEE Int. Microelectron Test Structures Conf.* Citeseer, 2001, pp. 137–141.
- [30] P. J. Tasker, "Practical waveform engineering," *IEEE Microwave Magazine*, vol. 10, no. 7, pp. 65–76, Dec. 2009.
- [31] D. M. Snider, "A theoretical analysis and experimental confirmation of the optimally loaded and overdriven rf power amplifier," *IEEE Transactions on Electron Devices*, vol. 14, no. 12, pp. 851–857, Dec. 1967.
- [32] A. Ferrero and M. Pirola, "Harmonic load-pull techniques: An overview of modern systems," *IEEE Microwave Magazine*, vol. 14, no. 4, pp. 116–123, June 2013.
- [33] M. S. Hashmi, F. M. Ghannouchi, P. J. Tasker, and K. Rawat, "Highly reflective load-pull," *IEEE Microwave Magazine*, vol. 12, no. 4, pp. 96–107, June 2011.
- [34] B. Leake, "A programmable load for power and noise characterization," in *IEEE MTT-S International Microwave Symposium Digest*, 1982, pp. 348–350.
- [35] P. Roblin, *Nonlinear RF Circuits and Nonlinear Vector Network Analyzers*. Cambridge University Press, 2009.

- [36] J. Muller and B. Gyselinckx, "Comparison of active versus passive on-wafer load-pull characterisation of microwave and mm-wave power devices," in *IEEE MTT-S International Microwave Symposium Digest*, vol. 2, May 1994, pp. 1077–1080.
- [37] S. Dudkiewicz, "Pulsed-bias pulsed-RF harmonic load-pull for gallium nitride (GaN) and wide band-gap (WBG) devices," in *IEEE International Conference on Microwaves, Communications, Antennas and Electronics Systems*, Nov. 2009, pp. 1–4.
- [38] C. Roff, J. Benedikt, and P. J. Tasker, "Design approach for realization of very high efficiency power amplifiers," in *IEEE MTT-S International Microwave Symposium Digest*, June 2007, pp. 143–146.
- [39] Y. Takayama, "A new load-pull characterization method for microwave power transistors," in *IEEE MTT-S International Microwave Symposium Digest*, June 1976, pp. 218–220.
- [40] F. M. Ghannouchi, F. Beaugard, and A. B. Kouki, "Large-signal stability and spectrum characterization of a medium power HBT using active load-pull techniques," *IEEE Microwave and Guided Wave Letters*, vol. 4, no. 6, pp. 191–193, June 1994.
- [41] J. Benedikt, R. Gaddi, P. J. Tasker, M. Goss, and M. Zadeh, "High power time domain measurement system with active harmonic load-pull for high efficiency base station amplifier design," in *IEEE MTT-S International Microwave Symposium Digest*, vol. 3, June 2000, pp. 1459–1462 vol.3.
- [42] M. Thorsell, "Nonlinear characterisation and modelling of microwave semiconductor devices," phdthesis, Department of Microtechnology and Nanoscience (MC2), Chalmers University of Technology, 2011.
- [43] P. Poire, D.-L. Le, and F. M. Ghannouchi, "A PC controlled fully automatic active load-pull measurement system using a pseudo-gradient algorithm," in *IEEE Instrum. & Meas. Tech. Conf.*, April 1995, p. 628.
- [44] G. P. Bava, U. Pisani, and V. Pozzolo, "Active load technique for load-pull characterisation at microwave frequencies," *Electronics Letters*, vol. 18, no. 4, pp. 178–180, Feb. 1982.
- [45] B. Hughes, A. Ferrero, and A. Cognata, "Accurate on-wafer power and harmonic measurements of mm-wave amplifiers and devices,"

- in *IEEE MTT-S Microwave Symposium Digest*, vol. 2, June 1992, pp. 1019–1022.
- [46] T. Williams, J. Benedikt, and P. J. Tasker, “Experimental evaluation of an active envelope load pull architecture for high speed device characterization,” in *IEEE MTT-S International Microwave Symposium Digest*, June 2005, pp. 4 pp.–.
- [47] M. S. Hashmi, A. L. Clarke, S. P. Woodington, J. Lees, J. Benedikt, and P. J. Tasker, “An accurate calibrate-able multiharmonic active load-pull system based on the envelope load-pull concept,” *IEEE Trans. Microw. Theory Techn.*, vol. 58, no. 3, pp. 656–664, March 2010.
- [48] T. Williams, B. Wee, R. Saini, S. Mathias, and M. V. Bossche, “A digital, pxi-based active load-pull tuner to maximize throughput of a load-pull test bench,” in *83rd ARFTG Microwave Measurement Conference*, June 2014, pp. 1–4.
- [49] D. J. Williams and P. J. Tasker, “An automated active source and load pull measurement system,” in *6th IEEE High Frequency Postgraduate Colloquium*, Sep. 2001, pp. 7–12.
- [50] Z. Aboush, C. Jones, G. Knight, A. Sheikh, H. Lee, J. Lees, J. Benedikt, and P. J. Tasker, “High power active harmonic load-pull system for characterization of high power 100-watt transistors,” in *European Microwave Conference*, vol. 1, Oct. 2005, p. 4.
- [51] M. Marchetti, M. J. Pelk, K. Buisman, W. C. E. Neo, M. Spirito, and L. C. N. de Vreede, “Active hharmonic load-pull with realistic wideband communications signals,” *IEEE Trans. Microw. Theory Techn.*, vol. 56, no. 12, pp. 2979–2988, Dec. 2008.
- [52] M. Squillante, M. Marchetti, M. Spirito, and L. C. N. de Vreede, “A mixed-signal approach for high-speed fully controlled multidimensional load-pull parameters sweep,” in *73rd ARFTG Microwave Measurement Conference*, June 2009, pp. 1–5.
- [53] M. Marchetti, “Mixed-signal instrumentation for large-signal device characterization and modelling,” Ph.D. dissertation, Microelectronics & Computer Engineering, Delft University of Technology, 2013.
- [54] R. E. Leoni, S. A. Harris, and D. G. Ries, “Active simultaneous harmonic source and load pull assisted by local polyharmonic

- distortion models,” in *IEEE MTT-S International Microwave Symposium Digest*, May 2010, pp. 1166–1169.
- [55] R. S. Saini, J. W. Bell, T. A. J. Canning, S. P. Woodington, D. Fitz-Patrick, J. Lees, J. Benedikt, and P. J. Tasker, “High speed non-linear device characterization and uniformity investigations at x-band frequencies exploiting behavioral models,” in *77th ARFTG Microwave Measurement Conference*, June 2011, pp. 1–4.
- [56] M. Marchetti, T. Maier, V. Carrubba, S. Maroldt, M. Mußer, and R. Quay, “Examples of high-speed harmonic load pull investigations of high-efficiency gan power transistors,” [Online]. Available from: <http://mwemedia.com/interlligentrif/MMarchetti.pdf>, Jan. 2007, accessed: 2018-10-12.
- [57] M. Thorsell and K. Andersson, “Fast multiharmonic active load-pull system with waveform measurement capabilities,” *IEEE Trans. Microw. Theory Techn.*, vol. 60, no. 1, pp. 149–157, Jan. 2012.

CHAPTER 3

HIGH SPEED MEASUREMENT SYSTEM BASED ON PXIE MODULES

3.1 INTRODUCTION

DEVELOPING a flexible and accessible high-speed RF measurement system is crucial. In particular, accessible system software can provide an opportunity to develop a scalable and user-defined RF measurement. For instance, this system can easily implement an automation process that can be tailored, changed and developed according to the user's preferences. Meanwhile, a fast measurement system would ensure that a large amount of data can be fetched from a DUT within a short time. For example, this system can quickly extract a reliable global behavioural model of a DUT. These features would also mitigate the effort and time required on behalf of the users. Moreover, traditional measurement systems are generally expensive, rigid, complex and cannot be readily extended, which is in contrast with the recent RF applications that have become increasingly more

complex and challenging. Consequently, a new measurement system that can be extended and reconfigured easily is now urgently required.

The aforementioned requirements can be achieved by using a new generation of software-designed and modular PXIe modules. These instruments allow for the development of a customisable and reconfigurable system that is able to keep up with the rapid pace of change in the RF and wireless industry while maintaining the required synchronisation and the desired measurement flow. Also, the speed of these instruments increases with modern, multi-core processors.

This chapter introduces a novel high-speed RF measurement system architecture that is based on commercially available PXIe modules. The data acquisition and processing of the presented measurement system allow for high measurement speed while maintaining a high dynamic range and accuracy. The existence of an efficient in-chassis controller and accurate synchronisation between generators and receivers provide for a high data throughput and enable rapid processing and analysis of large volumes of measurements. Signal processing at the sample level allows the system to continuously monitor its correct operation and adapt to the signals that are present at the DUT.

3.2 SYSTEM DESCRIPTION

The system architecture is based on PXIe modules [1] with an architecture similar to previously published non-linear measurement systems that are based on a NVNA [2]. A key difference is the special distribution of the PXI modules across chassis. The PXI modules do not share a common RF reference signal and are synchronised through the available clock signals, programmatic implementation of triggering and sample-level alignment.

In contrast to previously realised measurement systems, all RF instrument modules are based on IQ-architecture similar to software-defined transmitters and receivers that are utilised for the realisation of modern communication systems. Consequently, the realised measurement system shares a commonality with a wireless transceiver with a shared synchronisation channel. Figure 3.1 is a block diagram that shows the composition of the measurement system that was realised.

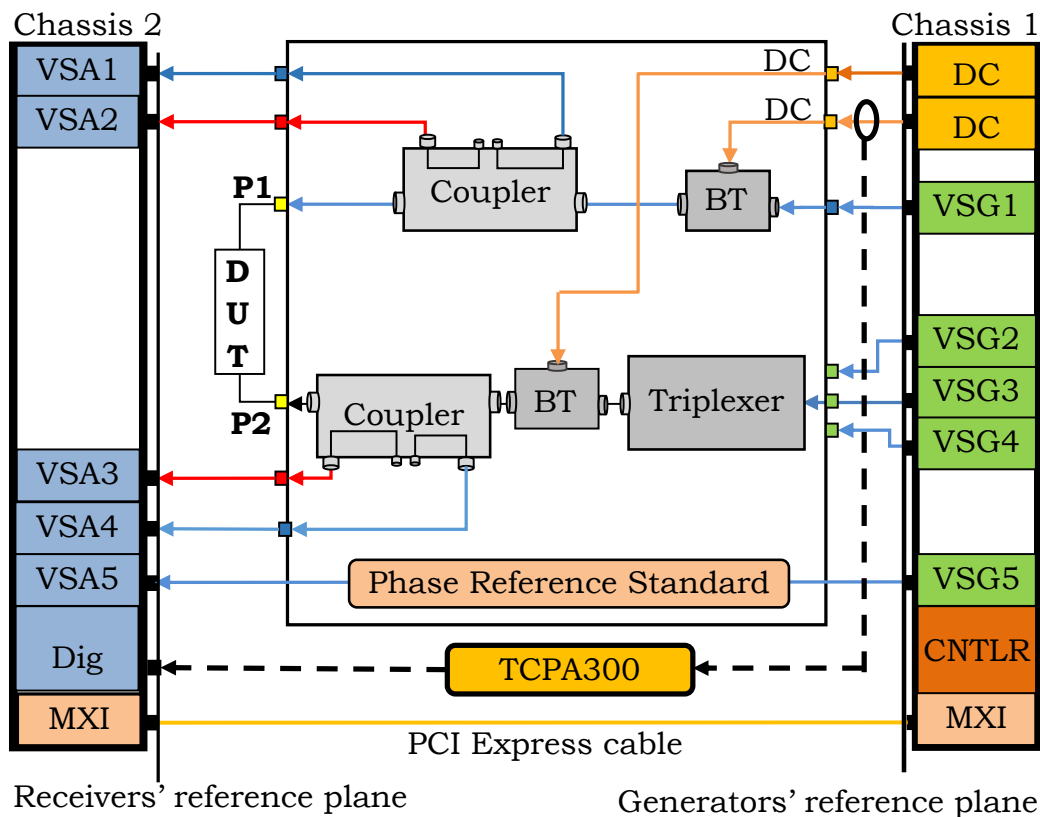


Figure 3.1: Generic block diagram of the PXIe modules-based measurement System

The system configuration includes two chassis (PXIe-1075) [3]. The first chassis has been assigned for vector signal generators PXIe-5673E (VSGs) [4]. It contains four VSGs: one to provide the fundamental input stimulus while other three are providing the fundamental and harmonic signals at the output of the DUT, hence facilitating an active harmonic injection load-pull. Moreover, RF signal synthesiser (PXIe-5652) [5] with a known phase output power amplifier has been assigned for generating the phase reference standard signal.

The second chassis has been used to hold five vector signal analysers PXIe-5663E (VSAs) [6]. Four of the VSAs are used to detect incident $a_{p,h}$ and reflected $b_{p,h}$ waves at the DUT terminals while the 5th VSA is used to monitor the harmonic spectrum of the phase reference standard. Moreover, two PXIe-5122 digitisers [7] are located within this chassis, which will be used as a high-speed current digitiser. The Agilent E3645A DC supply is utilised as the biasing unit, providing 2.2 A current up to 35 V and 1.3 A up to 60 V. This DC supply is controlled via a GBIP while a current probe amplifier (TCPA300) from Tektronix is used for high speed current measurement. As shown in Figure 3.1, the test-set consists of directional couplers, which are used to obtain the incident and reflected waveforms, and the triplexer is used to combine the injected harmonic signals. PAs can be inserted in the test-set to amplify the VSG signals to appropriate levels.

Figure 3.2 shows the generic structure of the measurement system. It illustrates the unique configuration of the load-pull system in which module-based generators and receivers are utilised.

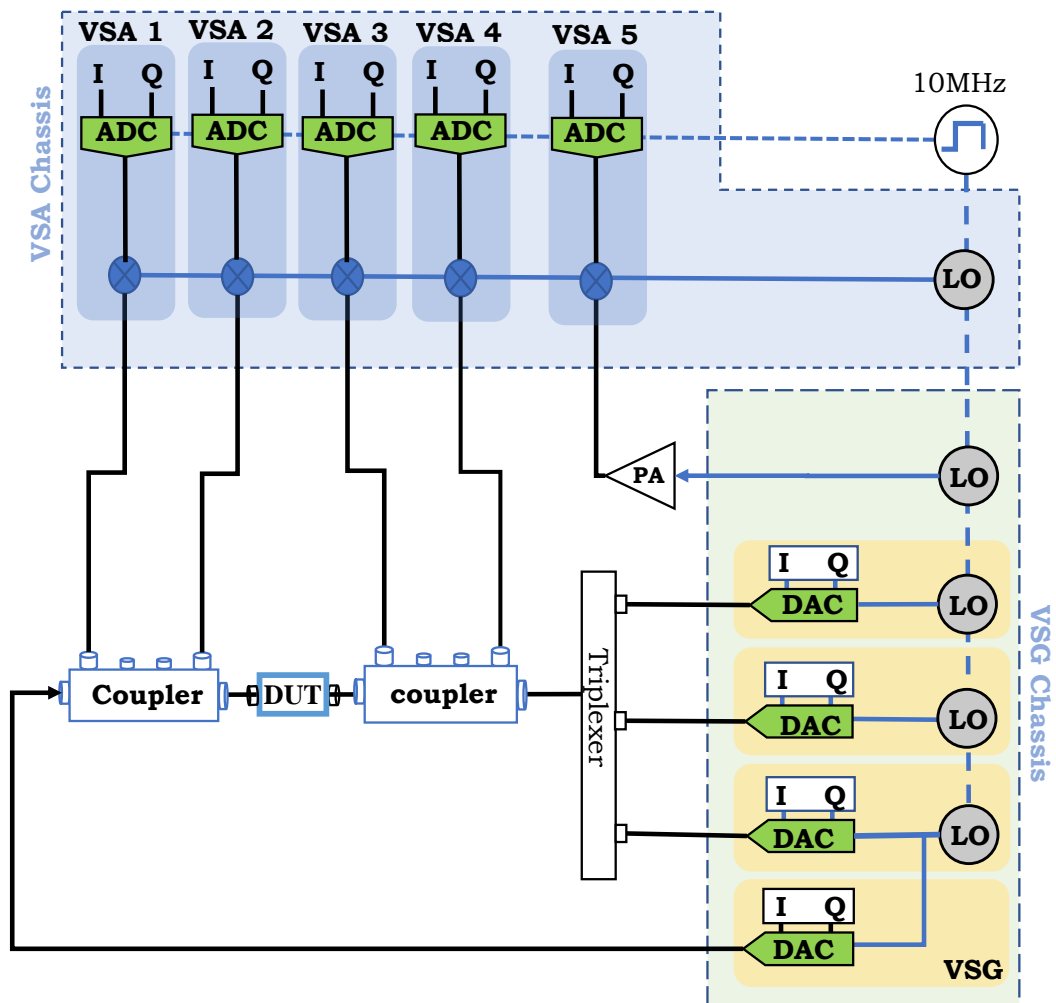


Figure 3.2: The generic illustration of the system architecture.

Three modules have been used to configure the VSG: IQ signal generator (NI PXIe 5450), digital to analogue converter (DAC) (NI PXIe-5611), and local oscillator (LO) (NI-PXIe 5652). Each VSA is composed of three modules: the local oscillator (NI PXIe-5652), down converter (NI PXIe-5601), and the analogue to digital converter (ADC) (NI PXIe-5622). All VSGs have the same instantaneous bandwidth of 50 MHz, allowing

for very fast load-pull sweeps. The RF phase synchronisation of the VSAs is aided through a shared LO signal, while time sampling of the down-converted input signals is controlled through a shared clock, as shown in Figure 3.2.

The VSAs have an instantaneous equalised bandwidth of 50 MHz, which can be moved anywhere between 10 MHz and 6.6 GHz through the control of the LO generator. The clock speed of the analogue-to-digital converters (ADCs) is software controlled with a maximum of 150 MS/second [8].

In case of Continuous wave (CW) measurements, the individual fundamental and harmonic I and Q signal components are down-converted in succession to DC, in which case the sampling frequency of the analogue-to-digital receiver is used to acquire multiple samples of the same DC measurement to facilitate rapid signal acquisition and processing. The direct down-conversion is utilised here to maximise the measurement speed because the maximum sampling rate of the VSAs is 150 MS/s¹ the system is capable of producing a maximum 150 million IQ samples per second, which can be used to average out

¹In a practical configuration, a lower sampling rate is utilised to comply with the equalised instantaneous bandwidth of 50 MHz.

the noise from the detected RF signal; hence, increasing the effective number of bits (ENOBs). Converting the signal down to an offset frequency F_{off} reduces the oversampling ratio (OSR) from F_s to $F_s/2F_{off}$ and, therefore, decreases the capability of reducing the noise within a given time.

Time delays within a single PXIe chassis are automatically compensated by the Trigger Clock (T-Clk) [9]. The T-Clk technology ensures time synchronisation across all linked channels and aligning the sample clock edges with a tolerance less than 500 ps. Additionally, manual tuning allows for further accuracy alignment approaching 4ps [10]. The two chassis are controlled by the same embedded controller (PXIe-8133) using the master-slave protocol.

Communication between the two chassis is established by using two modules Multisystem eXtension Interface (MXIe) PXIe-8370 and PXIe-8374, and Peripheral Component Interconnect Express (PCIe) cable. This link has the ability to transfer data at a rate of 10 Gbps in each direction simultaneously.

3.3 SYSTEM CALIBRATION

Calibration is a crucial process for microwave characterisation. Typically, it is used to correct data that has been delayed and attenuated by imperfect elements used within the test-set of the measurement system, such as cables and couplers [11]. For non-linear measurements, it is also important to obtain absolute power calibration of the receivers and their harmonic phase measurements aligned. For this, an absolute two-port calibration [12] has been implemented within the control software of this measurement system. Embedding and de-embedding routines are also included to move both reference planes towards the package, the device or an intrinsic plane. Moreover, dedicated calibration routines were introduced on the presented measurement system to establish the correct operation of the spatially distributed PXI modules. The first is used for the synchronisation between the two chassis to ensure a time-aligned generation and the acquisition of the I&Q data samples. The second dedicated calibration development was to achieve a phase alignment between receivers.

The system typically stores only the raw receiver data and applies the calibration for the analysis or to further process the measured data. This allows for the generation of an aggregate calibration that

combines the most appropriate calibration measurements from all three calibration steps. The aggregate calibration is then applied for the vector correction of the receiver data. The implementation of the aggregate calibration simplifies the calibration process because not all three steps have to be performed at the same time. In addition, the three different steps are associated with the sample-clock alignment, the correction of the receivers and the accounting for the impact of an RF test-set; hence, it allows for more localised error analysis of the measurement system in case of an erroneous calibration or system performance. A corrected calibration can then be also applied to raw data post measurements.

3.3.1 INTRA-CHASSIS TIME-BASED ALIGNMENT

Precise synchronisation between the two chassis is essential for simultaneous generation and acquisition. This has been achieved within the first calibration step by running the two chassis in master and slave configuration, with phase and sampling synchronisation being realised using a shared 10MHz clock and a trigger signal, respectively. The trigger is implemented using programmable function inputs and outputs (PFIs) [13], which are available at each of the PXI modules within the

specified margins. However, this is insufficient for phase-synchronised RF measurements due to the imperfection of the on-board synchronization techniques [10]. Moreover, transition time between successive measurements also has an impact on the measurement because unwanted measurements are added to the measured samples [14].

Figure 3.3 depicts the generation and acquisition process after the initial synchronisation and time-alignment of the sample clocks, with the different measurements separated by the different signal levels. As can be seen, an overlap between successive measurements is presented, with sampled data affected by the transition and sampling times within the utilised signal generators and receivers.

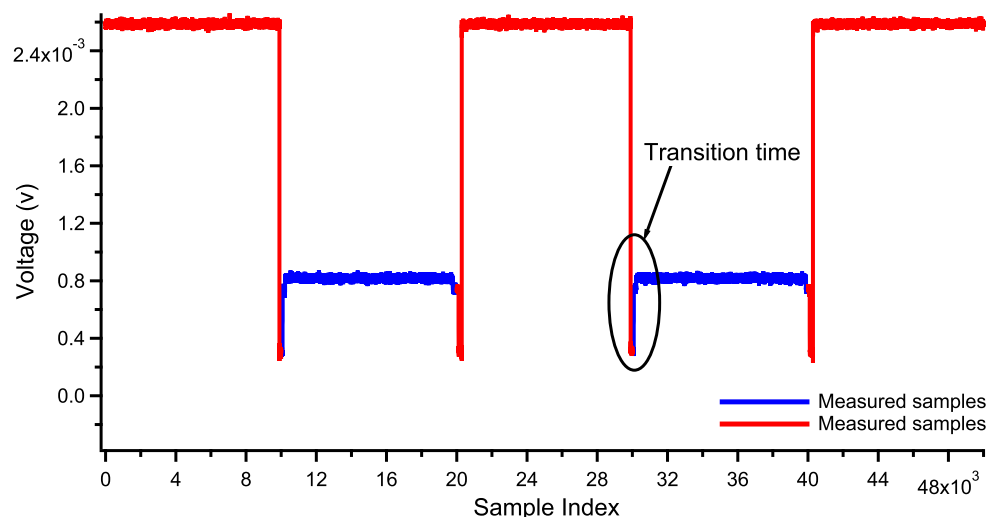


Figure 3.3: *Overlap problem between successive measurements with a sampling rate of 10MS/s set for vector signal generators and receivers.*

To ensure the correct data analysis and the system's dynamic range, the time interval for each measurement has been slightly increased to introduce guard bands between successive measurements. In addition, to compensate for the time delay between the two chassis the fetched samples (red trace) in Figure 3.3 can be shifted by a defined amount of time. This approach would allow for the suitable margin between the beginning of the measurement and the fetched samples.

Figure 3.4 shows a measured example where the generated samples (blue trace) and fetched samples that used for the averaging process (red trace).

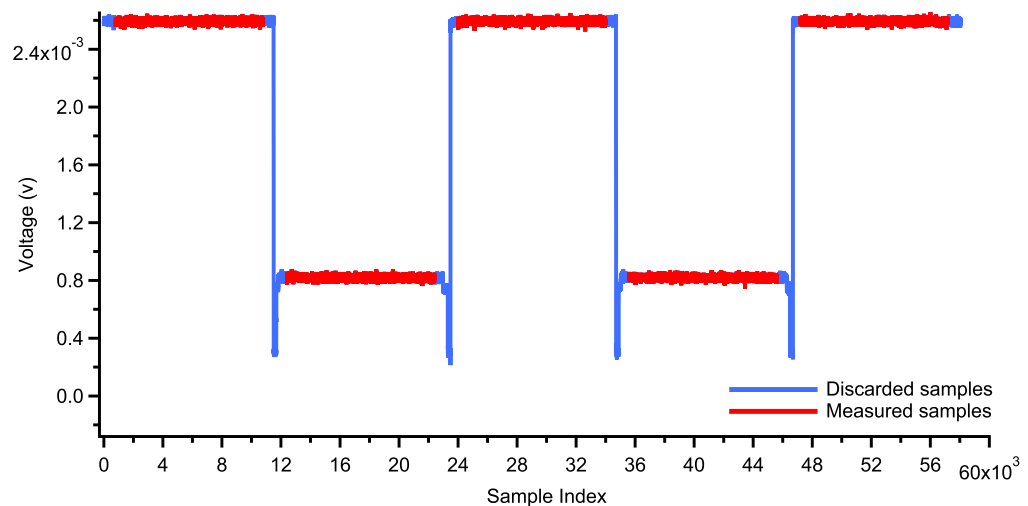


Figure 3.4: Actual example of the Synchronisation between the two chassis while measuring with the 10W Cree device.

In this example, the time delay to synchronise the generators and receivers has been set to 80µsec, while the guard band to account for the transition time is 80µsec either side of the measured samples. This increment in time requires a minimum number of samples per measured signal. Assuming a sampling rate (R) of 10MS/sec about 1600 sampling points are necessary for the implementation of the guard band. For a measurement of a signal that takes 10k samples per measurement, the measurement time per power level will be $11600 \times 10^{-7} = 1.16$ milliseconds, which provides a maximum of 862 measurements per second.

It should be noted that the number of the padded samples increases with an increasing sampling rate. This is due to the relatively constant timings within the set-up. Consequently, the measurement speed does not scale linearly with the sampling rate because at high sampling rates only a few measured IQ samples are obtained in comparison to the large number of dummy data. Moreover, the dramatic increase in the number of samples per measurement results in an increase in processing time.

3.3.2 RECEIVER PHASE AND POWER ALIGNMENT

Sharing common LO and a common reference clock does not guarantee sufficient phase coherence between receivers [10]. This problem is due to the difference in signal paths of the LO and the ADC sample clock, as shown in Figure 3.5.

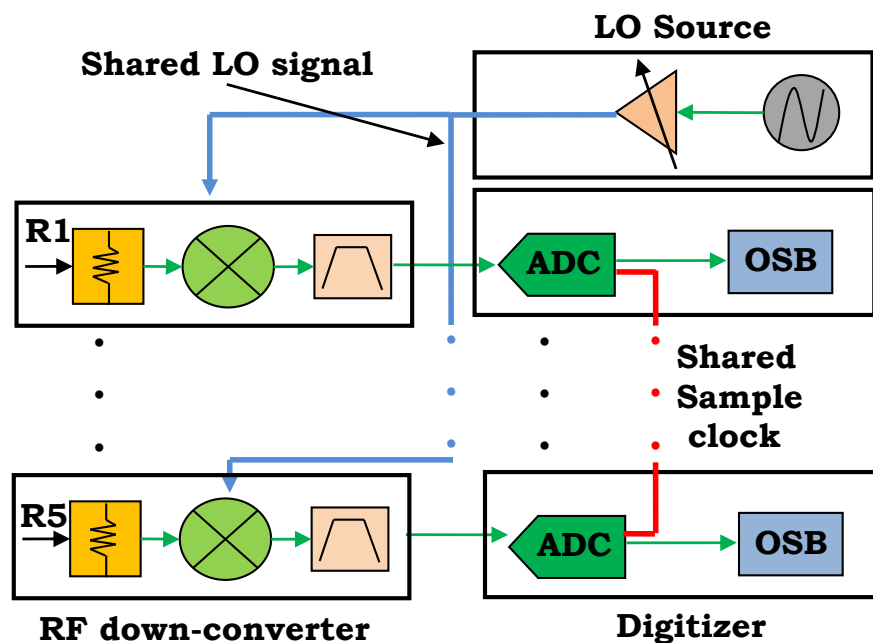


Figure 3.5: Block diagram of sharing LO between Receivers.

Moreover, because each receiver has a different internal temperature, is located on a different clock reference bus, and Tclk does not provide for a constant and unique solution, the length of the internal delays varies from one device to another. This relative difference causes phase offsets between VSAs [10].

Figure 3.6 shows the difference between the phase of each receiver and phase of reference receiver that is obtained during the receiver's phase and power alignment. The phase rotation represents a sub-sampled dataset due to the finite centre frequency resolution. The phase rotation does not represent a physical length of line due to active reconfiguration of the VSAs and VSGs during their operation.

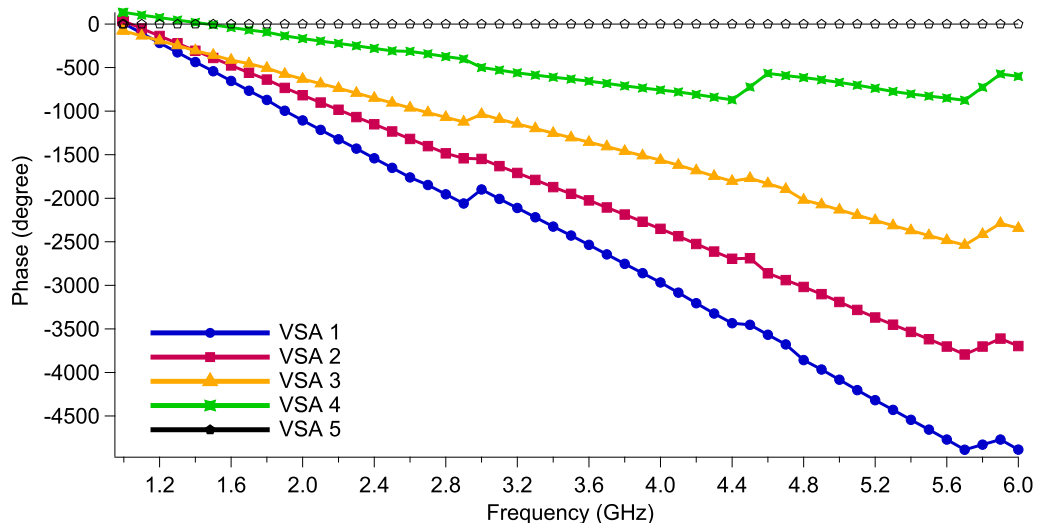


Figure 3.6: Phase difference between each VSA and a reference channel.

To achieve absolute power alignment and improve the accuracy of the signal power [15], the receivers' calibration routine also performs a power calibration of the receivers. Figure 3.7 shows a comparison between the power reading of VSAs and the power meter reading for the same input power level and it is clearly seen that the difference ranges from 0 to about 2.7 dBm.

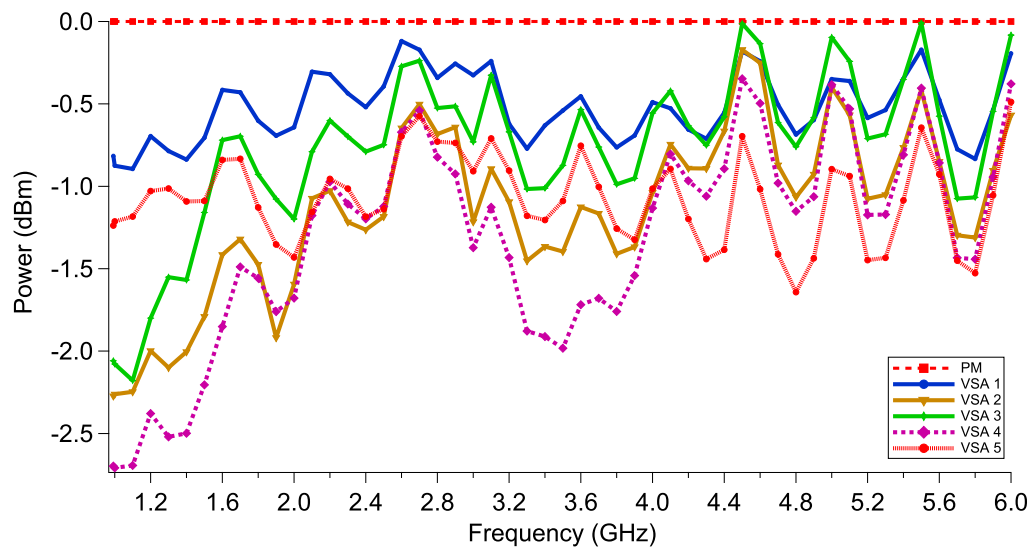


Figure 3.7: Normalized difference in power between each VSA and the power meter.

Phase alignment between harmonic signal components has been accomplished through comparisons of the same waveform measured by all VSAs. While the power alignment has been achieved by computing the differences between power meter reading and the VSAs' reading for the same input power level over a frequency grid.

The block diagram in Figure 3.8 shows a typical test set-up that been used to compute the phase difference between each receiver and the reference receiver, and also the power of each receiver and the power meter. The comparison is performed over a range of frequencies and the observed phase differences calculated and stored as phase error terms.

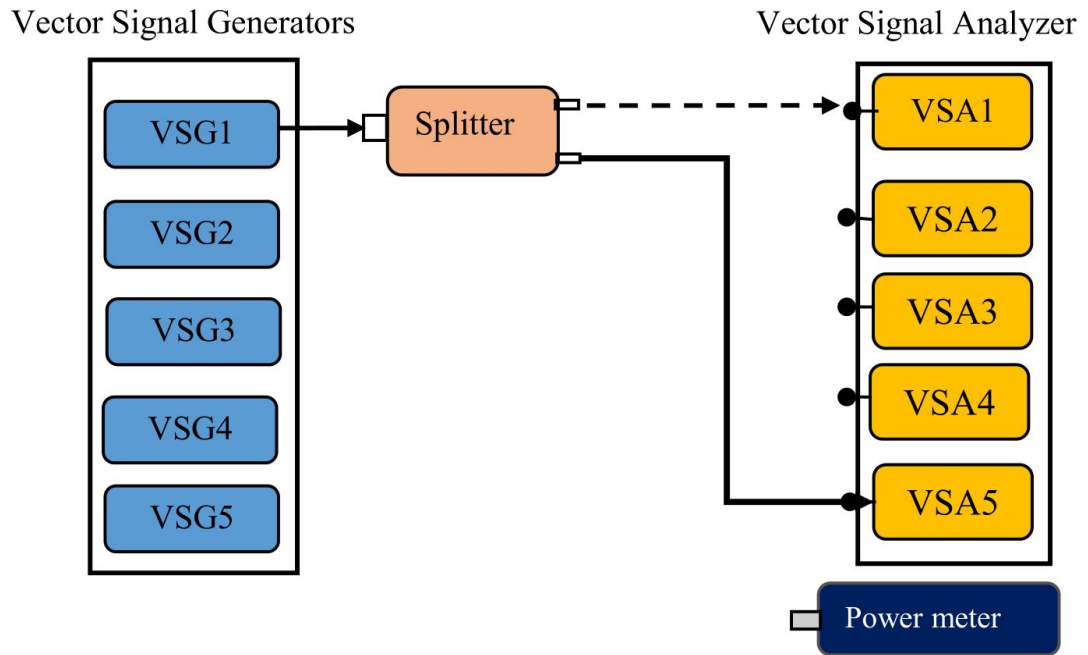


Figure 3.8: *Generic block diagram of the phase alignment measurement set-up*

The phase imbalance ($\Delta\phi^\circ$) of the power divider is taken into account through an additional measurement (M2), where cables are swapped between the reference receiver and another receiver; as shown in Figure 3.9.

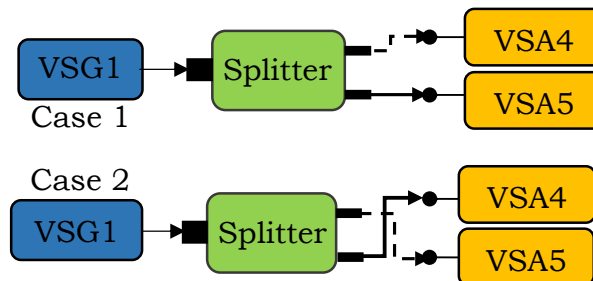


Figure 3.9: *Typical set-up of Splitter phase imbalance measurement.*

The difference of both measurements is directly related to the phase imbalance according to Equation 3.1 to 3.3.

$$M_1 : \phi_{R4} - \phi_{R5} = \phi_1 \quad (3.1)$$

$$M_2 : \phi_{R4r} - \phi_{R5r} = \phi_2 \quad (3.2)$$

$$\Delta\phi = \frac{(\phi_1 - \phi_2)}{2} \quad (3.3)$$

Applying phase and magnitude correction factors has allowed accurate calibrated phase and magnitude to be achieved at the device reference plane.

3.3.3 REQUIREMENT FOR A DEDICATED RECEIVER CALIBRATION

The requirement for a dedicated phase and magnitude calibration of the receivers has been investigated analytically and verified experimentally. Figure 3.10 shows the typical eight-term error model of a four-receiver measurement system after a small-signal calibration along its S_{00} response, an example is shown in Equation 3.4.

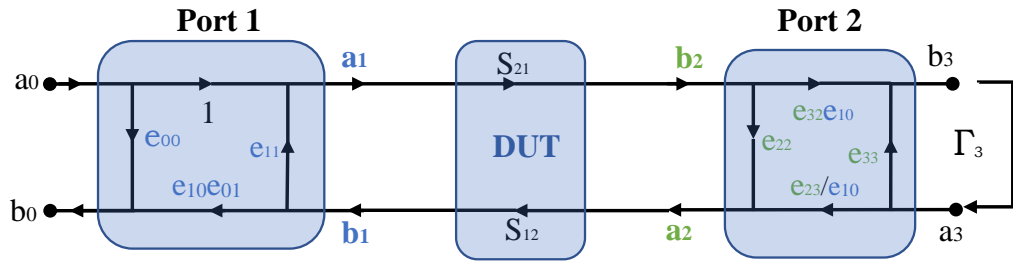


Figure 3.10: The eight-error terms error model after the small signal calibration.

$$S_{00} = e_{00} + \frac{(e_{01}e_{10}e_{22} - e_{01}e_{10}e_{22}e_{33}\Gamma_3 + e_{01}e_{10}e_{23}e_{32}\Gamma_3)}{(1 - e_{11}e_{22} - e_{33}\Gamma_3 - e_{23}e_{32}e_{11}\Gamma_3 + e_{11}e_{22}e_{33}\Gamma_3)} \quad (3.4)$$

To account for the spatial distribution of the receivers, Figure 3.11 includes phase delays between the receivers as separate parameters t_2 , t_3 and t_4 . Here, all of the time delays are referenced to receiver 1, which detect the a_0 signal.

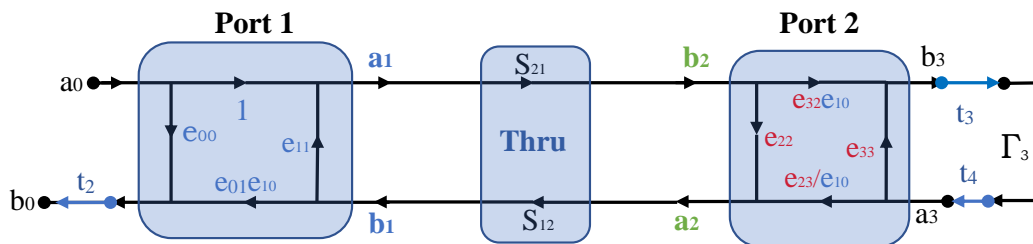


Figure 3.11: Forward error model revealing the effect of the receiver's asymmetry.

However, these additional parameters can be folded into the eight-term error model, which is depicted in Figure 3.12.

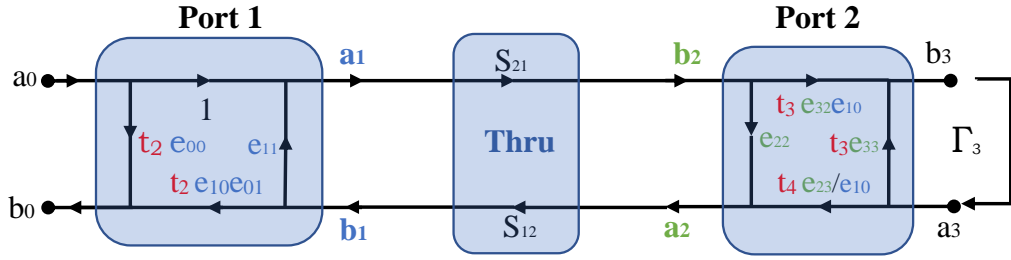


Figure 3.12: Forward error model revealing the effect of the receiver's asymmetry while they are folded within the error term.

Therefore, both error models in Figure 3.11 and 3.12 are able to correct for the systematic errors of the measurement system. For example, the S_{00} response is derived for both networks and shown in Equation 3.5.

$$S_{00} = e_{00}t_2 + \frac{e_{01}e_{10}e_{22}t_2 - e_{01}e_{10}e_{22}e_{33}t_2t_3t_4\Gamma_3 + e_{01}e_{10}e_{23}e_{32}t_3t_4\Gamma_3}{1 - e_{11}e_{22} - e_{33}t_3t_4\Gamma_3 - e_{23}e_{32}e_{11}t_3t_4\Gamma_3 + e_{11}e_{22}e_{33}t_3t_4\Gamma_3} \quad (3.5)$$

Because the two models produce the same S-parameter response, it is not necessary to model the delay parameters (t_2 , t_3 and t_4) separately for the correct S-parameters and large-signal measurements. The error correction model in Figure 3.11 has the delay parameters folded into the calculated error coefficients.

This situation changes during the large signal calibration stage where the combined error term $e_{10}e_{01}$ is separated [12]. During this stage,

Port 1 of the measurement system is connected to a receiver through a known extension network, as depicted in Figure 3.13.

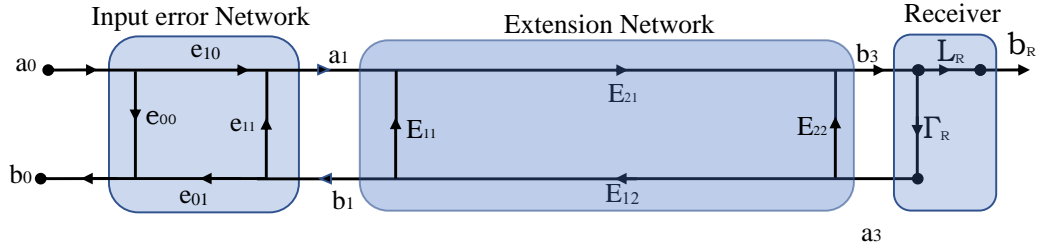


Figure 3.13: Flow graph of the error network during the extension scenario.

The extension network acts as an adaptor in case of connector mismatch between Port 1 and the receiver or in case both ports are inaccessible due to space restrictions. Because the s-parameters of extension network are known as a thru measurement², which determines the absolute phase and magnitude of the e_{10} error term as shown in Equation 3.6.

$$S_{21} = \frac{b_R}{a_0} = \frac{L_R \times e_{10} E_{21}}{1 - E_{11} e_{11} - E_{22} \Gamma_R - E_{12} E_{21} e_{11} \Gamma_R + E_{11} E_{22} e_{11} \Gamma_R} \quad (3.6)$$

To calculate e_{10} , it is vital that the receiver input port is close to 50Ω to minimise the reflection coefficient Γ_R and the delay within the receiver is close to zero $L_R = 1$. This assumes a minimal or zero phase delay

²In case the S-parameters are not known, a 1-port SOL calibration can be performed. Here, the extension network is attached successively to SOL standards instead of the receiver and Port 1 is used to perform calibrated s-parameter measurements. During the measurements, error-terms from the preceding small-signal calibration are utilised for Port 1.

between the receivers that are used for the s-parameter measurement. To meet this requirement, the receiver which is utilised during the thru calibration is required to have its delay parameter (either t_2 , t_3 and t_4) calibrated out. As a minimum, the delay parameter needs to be known. With the two assumptions, the S_{21} response of the thru measurement simplifies to $S_{21} = \frac{b_R}{a_0} = \frac{e_{10}E_{21}}{1 - E_{11}e_{11}}$, hence allowing for the extraction of the e_{10} error term.

To verify this analysis experimentally, a large-signal calibration was carried out without any preceding receiver calibration. In this case, the delay parameters (t_2 , t_3 and t_4) were present during the small- and large-signal calibrations. This includes the condition for the receiver delay $L_R = 1$ during the large-signal calibration, as shown in Figure 3.13, is not met. Figure 3.14 depicts the voltage and current waveform of a 10W Cree device in class-B bias at the output current generator plane.

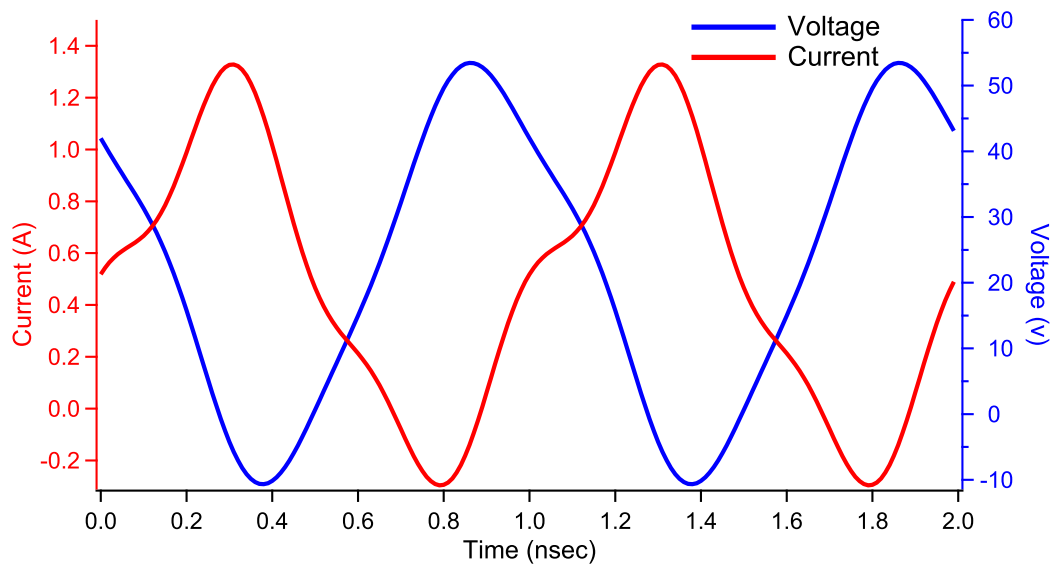


Figure 3.14: Voltage and current waveforms of 10W Cree device when the phase alignment between VSAs has not been applied at 1GHz frequency and class B biasing point.

It is seen in Figure 3.14 that the measured waveforms are not physically meaningful for a device operating at class-B condition. The current waveform has an unrestricted conduction angle with no sign of half-rectification. Figure 3.15 and 3.16 shows the waveform measurement and its associated load line of the same measurement with the receivers' calibration applied and the delay parameters (t_2 , t_3 and t_4) calibrated out before the small- and large-signal calibrations are carried out.

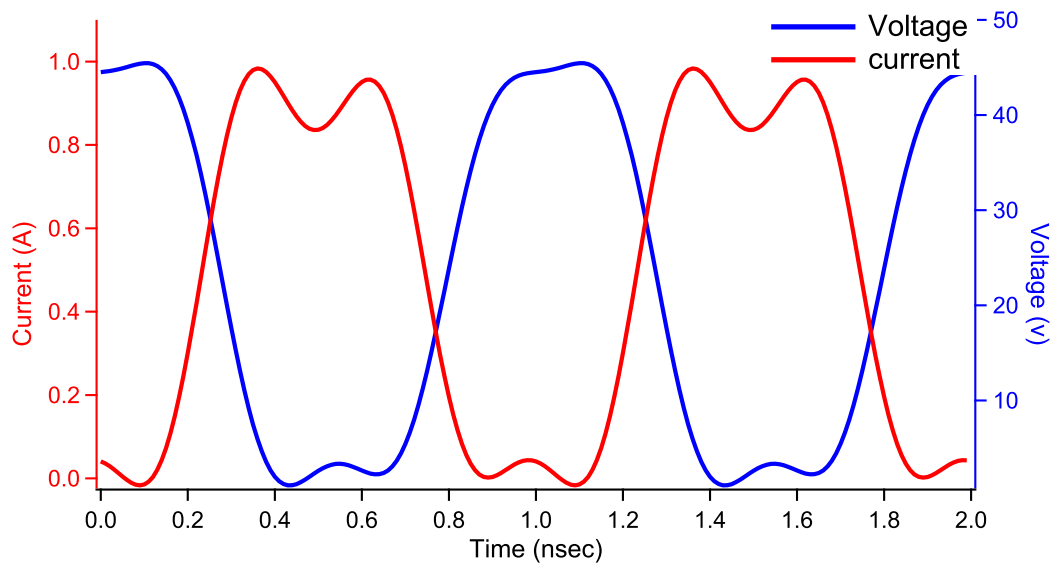


Figure 3.15: Voltage and current waveforms of 10W Cree device when the phase alignment between VSAs has been applied at 1GHz frequency and class B biasing point.

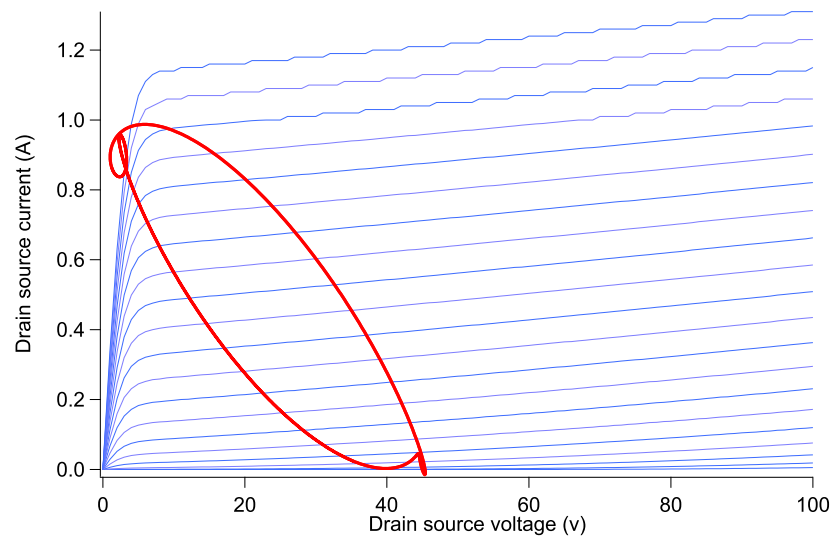


Figure 3.16: Load line of 10W Cree device at 1GHz frequency and class B biasing point.

As can be seen, the depicted measurements agree very well with the class -B theory of operation.

3.3.4 SYSTEM CALIBRATION AND VERIFICATION

An absolute calibration [12] is conducted to establish a reference plane at the input and output ports of the measurement system; that is, P1 and P2 in Figure 3.1. The resulting error coefficients are stored within a database. The system typically stores only the raw receiver data and applies the calibration for the analysis or further processing of measured data. The absolute two-port calibration has been validated on the presented measurement system using two methods: s-parameter and waveform measurements.

3.3.4.1 SMALL-SIGNAL CALIBRATION VERIFICATION

For the small-signal calibration, a TRL test-fixture was performed that consists of distinct thru-, reflect- and line-standards, which were mechanically milled out on Rogers TMM microwave laminates. To cover the entire 1-6.6GHz frequency range, only a single line element was employed. To estimate the quality of the calibration, the thru standard was re-measured and compared to its ideal values following the s-parameter calibration ($s_{11} = s_{22} = 0\angle 0$ and $s_{12} = s_{21} = 1\angle 0$) (as illustrated in Table 3.1).

Table 3.1: *Maximum difference between ideal and measured s-parameter of the through standard*

	S_{11}		S_{21}		S_{22}		S_{12}	
	Mag	$\Delta\phi^\circ$	Mag	$\Delta\phi^\circ$	Mag	$\Delta\phi^\circ$	Mag	$\Delta\phi^\circ$
Ideal diff.	0	0	0	0	0	0	0	0
Max. diff.	0.026	3.13	0.015	2.3	0.026	3.1	0.01	2.1

Considering the limitation of the realised TRL Cal-kit and the number of coaxial re-connections, the overall agreement is very good with less than -20dB for the magnitude and less than 4° for the phase. Moreover, a short and open standard that were not part of the small signal calibration were measured on Ports 1 and 2 over the whole range of frequencies 1–6.6 GHz. The results in Table 3.2 show the maximum difference observed between the ideal and measured S_{11} and S_{22} value over the whole frequency range, which again shows that the maximum magnitude difference is less than -20 dB within the S_{22} of short standard measurement.

Table 3.2: *The maximum difference between measured and ideal s-parameter of the short and open standard*

Standard	Short		Open	
	S11	S22	S11	S22
Ideal	0	0	0	0
Observed	0.053	0.09	0.065	0.08

To evaluate the small-signal calibration over the passive impedance plane, additional measurements on the thru-standard were performed under different load conditions. Here, the active load-pull emulated the load-reflection coefficients up to a magnitude of $\Gamma_{21} = 0.9$ using a spiral a_{21} injection pattern. The measured S_{21} values of the thru-standard are shown in Figure 3.17.

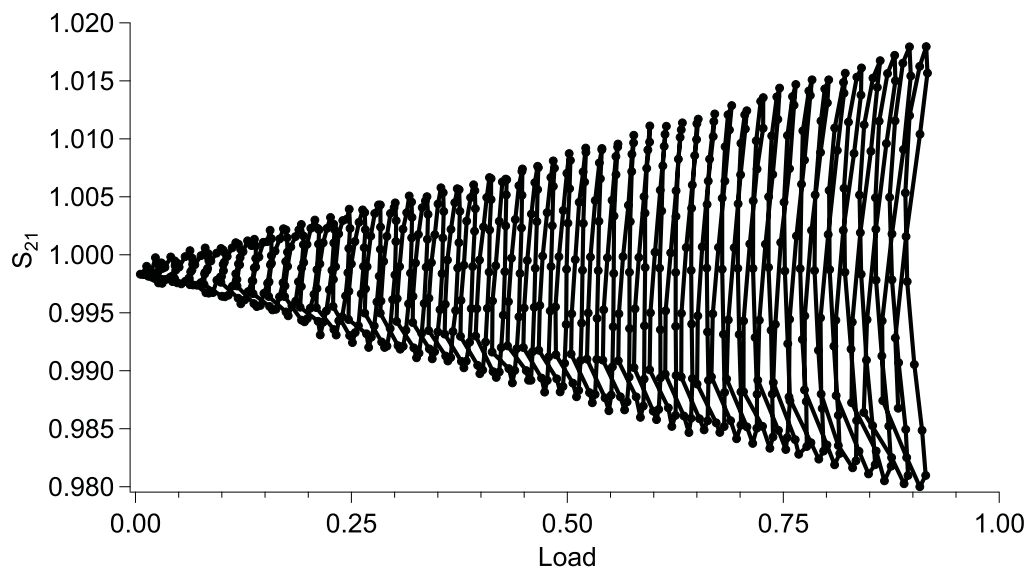


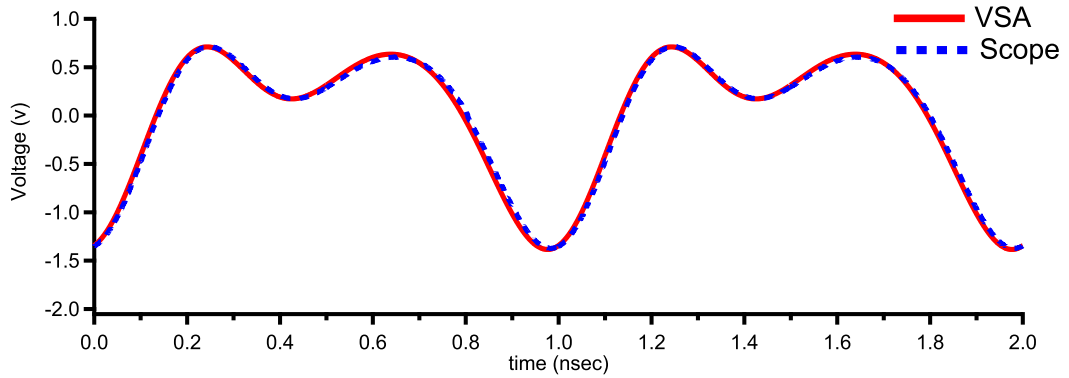
Figure 3.17: S_{21} of the thru standard over different load conditions and 1GHz operating frequency

The figure shows that maximum deviation from the ideal thru performance is less than 0.02, which indicates a source/load match error around -34 dB, and an excellent small-signal calibration validity over the Smith Chart.

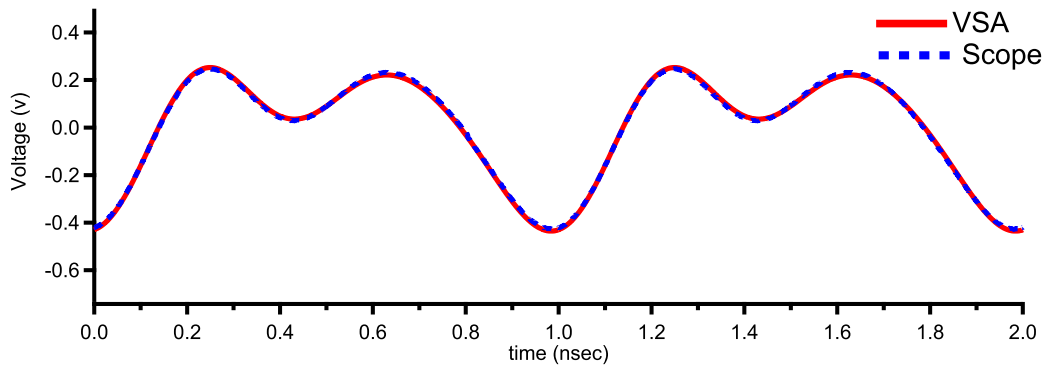
Given that the generated travelling waveform was directly inserted into the oscilloscope, no large signal calibration was required for its measurements, while the generated signal measured by the VSAs has been corrected by applying the calibration error model for the measurement system. Waveform measurements were conducted simultaneously by both receiver types at different fundamental power levels ranging over the combined dynamic range. The relationship between the harmonics was kept constant. A selection of the performed measurements is shown in Figure 3.19. The comparison has shown a good agreement between the two waveforms sets. Table 3.3 quantifies the maximum difference that has been observed over the three harmonics for 3 different power levels ranging from -20 dBm to 10dBm. It can be seen that both measurements produce almost the same time-domain waveform. The small differences are subscribed to the difference between the input impedance of the oscilloscope and the 50Ω termination that was used during the large-signal calibration.

Table 3.3: Comparison between waveforms measured by Scope (S) and the measurement system (M) for three harmonics (H)

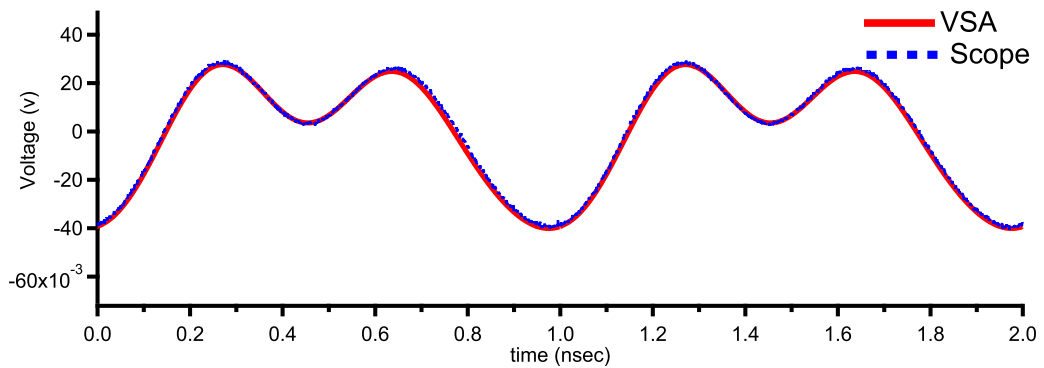
H	S(dBm)	M(dBm)	Δ(dBm)	S(ϕ°)	M(ϕ°)	Δ(ϕ°)
1FO	-22.05	-21.85	0.2	0.0 °	0.0 °	0.0 °
2FO	-24.58	-24.84	0.3	177.7 °	175.9°	1.78 °
3FO	-8.7	-9.04	0.32	-56.1°	-57.7°	1.61°



(a) high power ($F0 = 7.25dBm, 2F0 = 5.18dBm, 3F0 = -8.7dBm$)



(b) average power ($F0 = -2.4dBm, 2F0 = -4.5dBm, 3F0 = -17.5dBm$)



(c) low power ($F0 = -22.05dBm, 2F0 = -24.5dBm, 3F0 = -37.6dBm$)

Figure 3.19: Comparison between waveforms measured by oscilloscope and the measurement system at different power levels.

3.4 MEASUREMENT SYSTEM PERFORMANCE

To assess the system's performance and to evaluate its adaptability, quality of the measured data, dynamic range, standard deviation, and the quality of the samples distribution, power sweep measurements were performed on a packaged 10 W GaN HEMT operating at 1GHz while biased in class B using $V_{GS} = -3.2$ V and $V_{DS} = 28$ V.

3.4.1 DYNAMIC RANGE AND MEASUREMENT SPEED

The presented measurement system has first been evaluated in terms of the dynamic range and the measurement speed. Regarding the dynamic range, six harmonics of the 10 W Cree device have been measured over an input power range of 70 dB, as shown in Figure 3.20. The fundamental frequency of 1 GHz and the first five harmonics were chosen to cover the whole frequency range of the measurement system (1-6 GHz) while the device was terminated into 50Ω . The measurement result in Figure 3.20 shows that the dynamic range of the system approaches 100 dB.

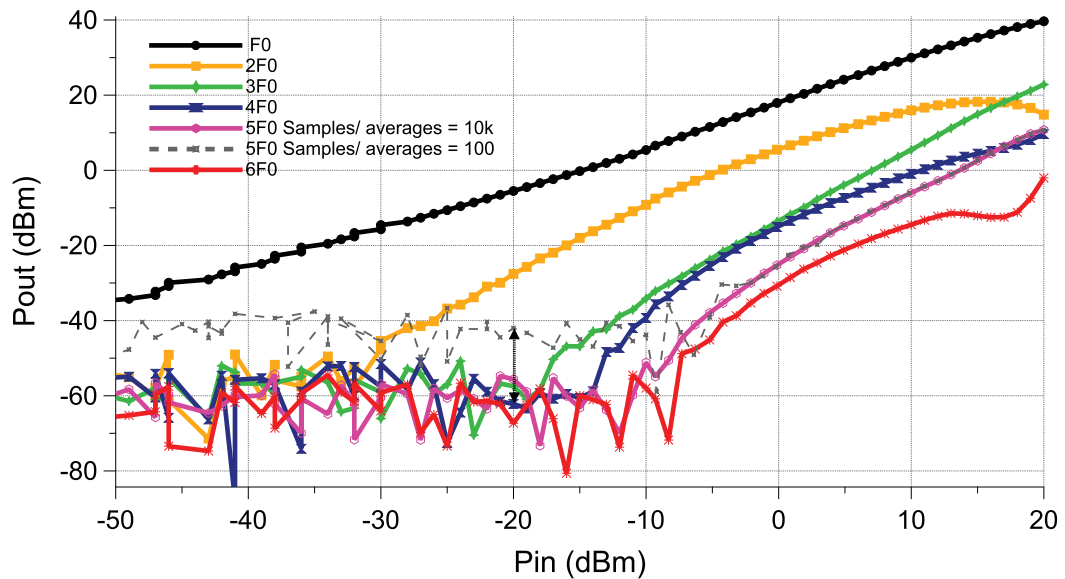


Figure 3.20: Harmonic measurement of the 10W Cree device while operating at 1GHz fundamental frequency and class B biasing condition.

To further verify the measurement system and its alignment with the theory, the influence of the averaging on the dynamic range has been investigated. An example is shown in Figure 3.20, where an additional 5th harmonic measurement utilising 100 averages was performed. The measured signal-to-noise ratio has increased, in accordance with theory, by about 20 dB. Because the measurement system directly detects the voltage, which has been down-converted to DC, the signal to- noise ratio should scale with $(1/\sqrt{N})$, with (N) being the number of averages. Therefore, the signal-to-noise ratio of a power signal $P \propto V^2$ should improve with an increasing $(1/\sqrt{N})^2 = 1/N$ number of averages per measurement. For 100 averages, the resulting improvement should be $10 \times \log(100) = 20dB$ and for 10,000 an increase of up to 40 dB. The

difference between both average settings is 20 dB, as confirmed by the 5th harmonic measurement.

The measurement speed of the system during the fundamental power sweep has been quantified. This was measured over various numbers of averages per measurement, ranging from 100 to 10K; as shown in Figure 3.21.

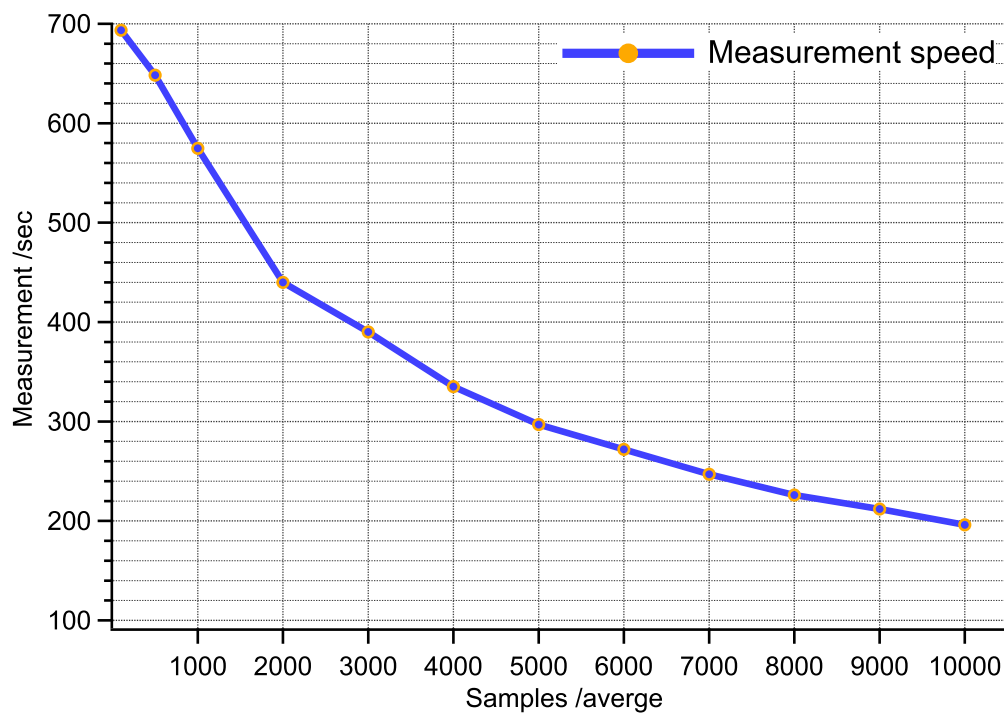


Figure 3.21: Execution speed of the PXIe based measurement system over different samples per average.

As predicted, the measurement speed is inversely proportional to the number of averages per measurement. The maximum measurement

approaches 700 measurements/sec at 100 samples/averages. This measurement speed includes the measurement time and processing of the data, and shows the results of the fundamental power sweep at sampling rate of 10MHz/sec.

3.4.2 STANDARD DEVIATION MEASUREMENT

The standard deviation of the raw measured samples provides an indication of the noise floor at the receiver plane. Consequently, the standard deviation of the measurement system has been assessed through different cases while measuring the second harmonic signal of 10 W Cree device at the same operating conditions that been applied through the previous measurement. In this case the sampling rate has been changed for two different values. For each value, the number of samples per measurement has been changed to 100 samples and 10 k samples. The resulting standard deviation is shown in Figure 3.22.

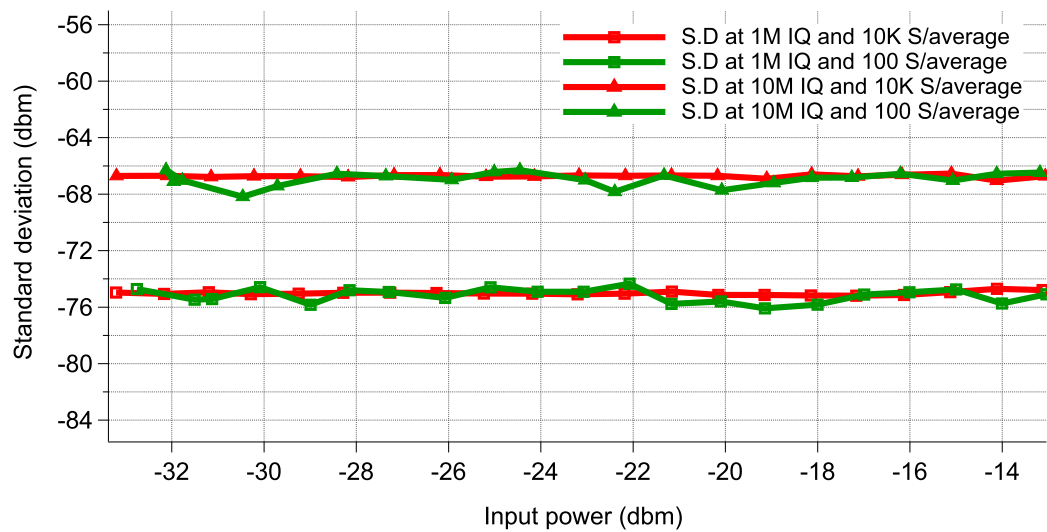


Figure 3.22: Standard deviation measurement of second harmonic signal

Figure 3.22 shows the dependence of the measurement on these different setting parameters. As can be seen, the standard deviation for both measurements using 100 and 10 K averages is the same. This agrees well with the theory because an increase in averaging does not decrease the noise floor but allows for a more accurate cancellation of the noise contributions contained within each measured sample.

The impact of the IQ sampling rate on the measurement system was also assessed. The measurements with 100 and 10K samples per average were carried out at a reduced IQ sampling rate of 1 MHz. Assuming a constant noise power spectral density, the noise f in dB should rise with the instantaneous measurement bandwidth (BW) by $10 \log_{10}(BW)$. Therefore, a drop from 10 to 1 MHz should improve

the signal-to-noise ratio by about 10 dB. This lines up well with the depicted noise floor of the second power sweep at about -76 dBm.

A calculation of noise power spectral density for both utilised IQ sampling rates delivers approximately the same and constant value over a range of measurement settings:

$$\begin{aligned} -67\text{dBm} - 10\log(10 \times 10^6) \text{ dB} &= -136\text{dBm/Hz} \\ &\approx -76\text{dBm} - 10\log(1 \times 10^6)\text{dB} = -136 \text{ dBm/Hz} \quad (3.7) \end{aligned}$$

This figure represents a compound of the noise contributions from the receivers, with a thermal noise floor at about -158 dBm/Hz [16], the phase noise within the signal, and the device output noise. The phase noise element is confirmed through an additional measurement with all signal sources being switched off, providing a figure that is about -2dB lower. Given that the system is set-up for power measurements up to 100 W, a 54 dB of attenuation in total is used between the DUT and the receiver. Therefore, the impact from noise floor at the device terminal can be assumed to be negligible, which suggest the potential application of the system for noise type characterisations with a more suitable test-set. These results also demonstrate the correct implementation of the system control software, the system

reconfigurability and the underlying quality of the measurement data in the presence of noise.

3.4.3 ANALYSIS AND UTILISATION OF DATA STATISTICS

Because the statistical data is directly linked (at least within the present set-up) to the fundamental behaviour of the PXIe instrumentation, it lends itself to the continuous monitoring of the correct operation of the measurement system. For instance, a misalignment of the sequencing within generators or the receivers will produce significant changes within the standard deviation of the measured signals. To illustrate this point, 10 k samples of the IQ measurements were taken from the high and low power level of the 2nd harmonic power sweep, as depicted in Figure 3.20, to generate histograms of two different power levels. The resulting graphs are depicted in Figure 3.23 (a), (b), (c), and (d).

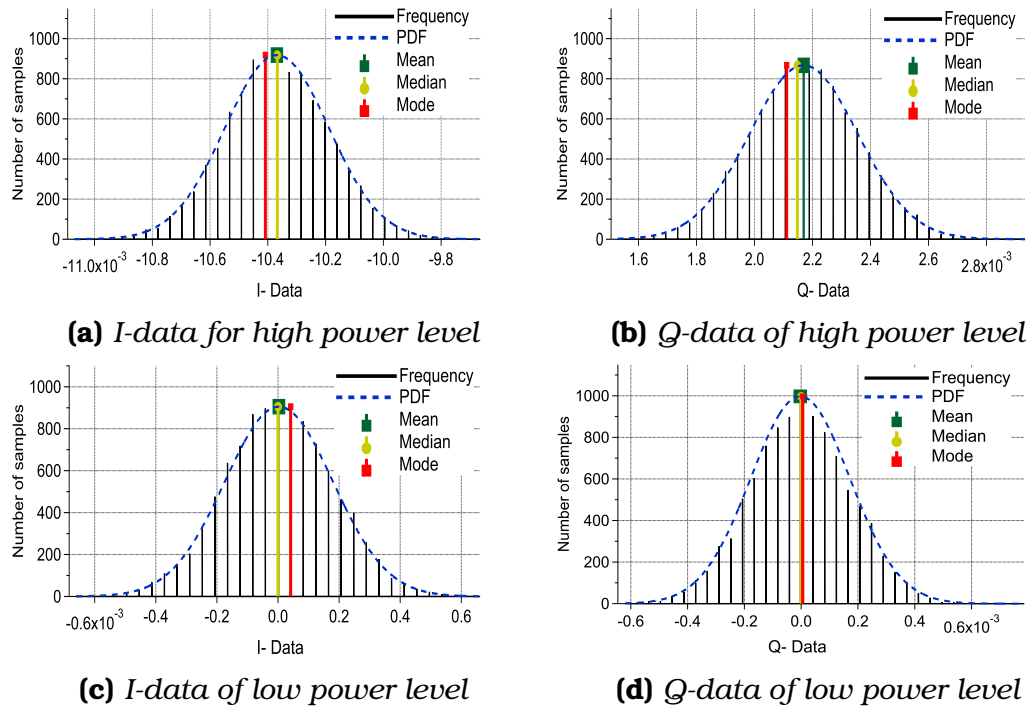


Figure 3.23: Histogram representation of measurements consisting each of 10k samples of the second harmonic signal (b_{22}) at two power levels measured from 10 W Cree device. Bias point: $V_{gs}=-3.2$ V, $V_{ds}=28$ V. Fundamental frequency 1GHz.

Figure 3.23a and 3.23b represent the I&Q data of a signal with a relatively high-power value and show the statistical distribution of the detected 10,000 samples during a single measurement. The histograms have a normal distribution of the samples that can be fit by a normally-distributed probability density function. This holds true also at lower power levels, as shown in Figure 3.23c and 3.23d.

For a robust representation of the measurement average, several averaging algorithms have been investigated, including mean, median,

and mode. The mean is the average of the all measured samples, while the mode is the result of taking the most common value within the measured samples. The median is the value of a sample correspondent to the index $\frac{(n+1)}{2}$ where “ n ” is the number of samples.

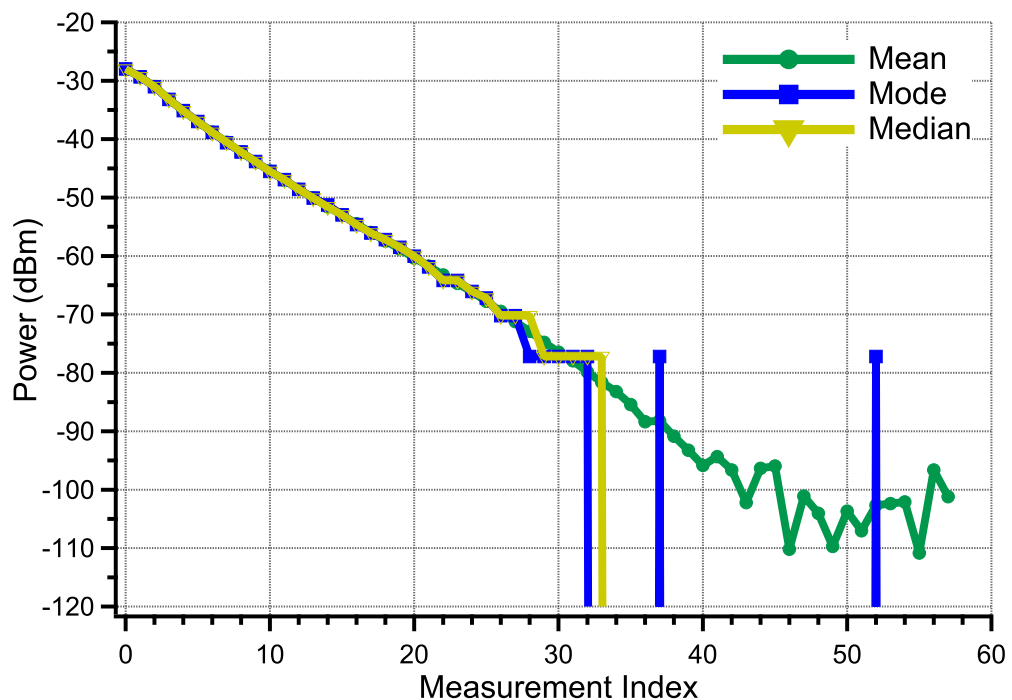


Figure 3.24: Comparison between the utilisation of mean, mode, and median for samples averaging process

Figure 3.24 shows the different averaging methods for the same 2nd harmonic power sweep as shown in Figure 3.20. It can be seen that the mean algorithm is the most consistent and stable across the entire range of power levels. The higher frequency of the zero value within the detected samples, as seen in Figure 3.23c and 3.23d, at low power levels (approaching -105 dBm) causes inconsistencies within

the median and mode results because the algorithms identify the sample that occupies the highest frequency, which is often a zero value in the measurement of low power signals.

3.5 CHAPTER SUMMARY

A high-speed non-linear RF characterisation system that is able to execute 200 measurements per second for the fundamental power sweep has been presented and validated. The system is configured by modular PXIe instrumentations distributed on two PXIe chassis, with a high degree of customisation, down to I/O pin level. The system can readily be re-configured and it delivers a high-level of flexibility, which provide for a software-defined nonlinear measurement system. In addition to the synchronization techniques that are provided by the PXIe instrumentation, a simple synchronization routine that guarantees fetching the correct samples during the characterization process has been implemented. Moreover, a suitable absolute 2-port calibration, which reflects the local distribution of the systems architecture has been implemented and verified. The verification has been achieved on several aspects, including the S-parameter measurement of the

Through standard. This kind of verification showed a good agreement with the ideal values that are expected to be measured. On the other hand and for further verification, the measured waveforms by the PXIe system were compared to measurements from the Tektronix sampling oscilloscope, which are again, a very good agreement between the two different measurement systems has been shown. By using suitable averaging methods and data processing, the system's dynamic range is shown to reach up to 100 dB with a noise floor at about -136 dBm/Hz. Monitoring the statistics of the measured samples allows for instantaneous and continuous evaluation of the status of the measurement system and the quality of the performed measurements.

REFERENCES

- [1] National Instruments, “*Configuring PXI Systems Using MXI-Express*,” (2010). [Online]. Available from:<http://www.ni.com/newsletter/51446/en/>, accessed: 2018-10-10.
- [2] P. J. Tasker, “Practical waveform engineering,” *IEEE Microwave Magazine*, vol. 10, no. 7, pp. 65–76, Dec. 2009.
- [3] National Instruments, “*NI PXIe-1075 User Manual*,” (2017). [Online]. Available from:<http://www.ni.com/pdf/manuals/372537c.pdf>, accessed: 2018-10-10.
- [4] National Instruments, “*PXIe-5673E Specifications*,” (2017). [Online]. Available from:<http://www.ni.com/pdf/manuals/375220d.pdf>, accessed: 2018-11-03.
- [5] National Instruments, “*PXIe-5652E Specifications*,” (2017). [Online]. Available from: <http://www.ni.com/pdf/manuals/375087b.pdf>, accessed: 2018-11-03.
- [6] National Instruments, “*PXIe-5663E Specifications*,” (2017). [Online]. Available from:<http://www.ni.com/pdf/manuals/375505b.pdf>, accessed: 2018-11-03.
- [7] National Instruments, “*PXIe-5122 Specifications*,” (2017). [Online]. Available from:<http://www.ni.com/pdf/manuals/376938c.pdf>, accessed: 2018-11-03.
- [8] National Instruments, “*PXIe-5663E Specifications*,” (2017). [Online]. Available from:<http://www.ni.com/pdf/manuals/375505b.pdf>, accessed: 2018-10-12.
- [9] S. Chaudhary and A. Samant, “Characterization and calibration techniques for multi-channel phase-coherent systems,” *IEEE Instrumentation Measurement Magazine*, vol. 19, no. 4, pp. 44–50, August 2016.
- [10] D. Hall, A. Hinde, and Y. Jia, “Multi-channel phase-coherent RF measurement system architectures and performance considerations,” in *2014 IEEE Military Communications Conference*, Oct. 2014, pp. 1318–1323.
- [11] D. M. Pozar, *Microwave Engineering*. John Wiley & Sons, 2011.

-
- [12] J. Benedikt, R. Gaddi, P. J. Tasker, and M. Goss, "High-power time-domain measurement system with active harmonic load-pull for high-efficiency base-station amplifier design," *IEEE Trans. Microw. Theory Techn.*, vol. 48, no. 12, pp. 2617–2624, Dec. 2000.
- [13] National Instruments, "*Reducing Test Time with RF List Mode*," (2010). [Online]. Available from:<http://www.ni.com/white-paper/10312/en/>, accessed: 2018-10-23.
- [14] V. Teppati, A. Ferrero, and M. Sayed, *Modern RF and Microwave Measurement Techniques*, V. Teppati, A. Ferrero, and M. Sayed, Eds. Cambridge University Press, 2009.
- [15] National Instruments, "*Five RF Measurements Everyone Should Know*," (2010). [Online]. Available from:<http://www.ni.com/newsletter/51446/en/>, accessed: 2018-10-10.
- [16] National Instruments, "*PXI Vector Signal Analyzers*," (2017). [Online]. Available from:<http://www.ni.com/pdf/product-flyers/pxi-vector-signal-analyzers.pdf>, accessed: 2018-10-10.

CHAPTER 4

AUTOMATED FUNDAMENTAL LOAD-PULL MEASUREMENT

4.1 INTRODUCTION

TO effectively capture a DUTs performance for a RF PA or system design, large-signal characterisations are required that entail a set of comprehensive load-pull measurements. Due to the time taken for these measurements, device manufacturing industries typically only employ a simplified and streamlined set of measurements, focusing more on DC and S-parameter pass/fail type measurement regimes [1]. The excessive time required for load-pull measurements is caused by several problems. First, the traditional active load-pull systems are typically operated by a human, where the bottle-neck becomes the speed at which a human can set-up and control the characterization process. For example, the location of the measurements grid and the optimum impedance has to be predefined to provide an initial estimate of optimum impedance.

Another related aspect is the nature of how active load-pull systems are driven and their reliance on a feedback mechanism to obtain target impedances and keep them over a range of DUT operating conditions, such as bias, frequency or drive power [2]. This measurement strategy would require many iterations to achieve load target with a sufficient accuracy when those iterations are consuming most of the measurement time. It has been reported that time taken by a single load-pull measurement is about 1 second when a passive load-pull system is used and is 0.4 second when an active load-pull system is used, while it is 0.19 sec when using a hybrid digital tuner [3, 4]. Even the fastest reported results would allow only 25 load-pull measurements per second [5], which is prohibitively slow within a manufacturing environment where hundreds of measurements are required within less than a second. In reality; any load-pull measurements would have to be added onto existing characterisation regimes, leaving only a fraction of second available.

This chapter will present an automated fundamental active load-pull measurement process by which human interaction and load-pull iterations can be reduced or even eliminated through the integration of a real-time behavioural model extractor within the measurement control software [6, 7]. The load-based Cardiff behavioural model has been

exploited to allow for the prediction of DUT response (b_{21}) at target load conditions. This has enabled the development of an automated model driven load-pull that can track and define the optimum impedance of an unknown DUT within a few seconds.

Moreover, the automated load-pull measurement process has been extended to define the optimum impedance at multiple power levels within one measurement session, further reducing the large signal DUT characterisation because the requirement to repeat the same process at every power level has almost been eliminated because there will be no need to conduct the process of finding the optimum impedance correspondent to the new power level. This approach has been extended to second harmonic load-pull measurements using load-based Cardiff behavioural mixed model.

4.2 AUTOMATED ACTIVE LOAD-PULL MEASUREMENT

Figure 4.1 shows the system configuration on which the process of the automated fundamental load-pull measurements was developed. The generic system configuration is similar to the measurement setup that was used in [7].

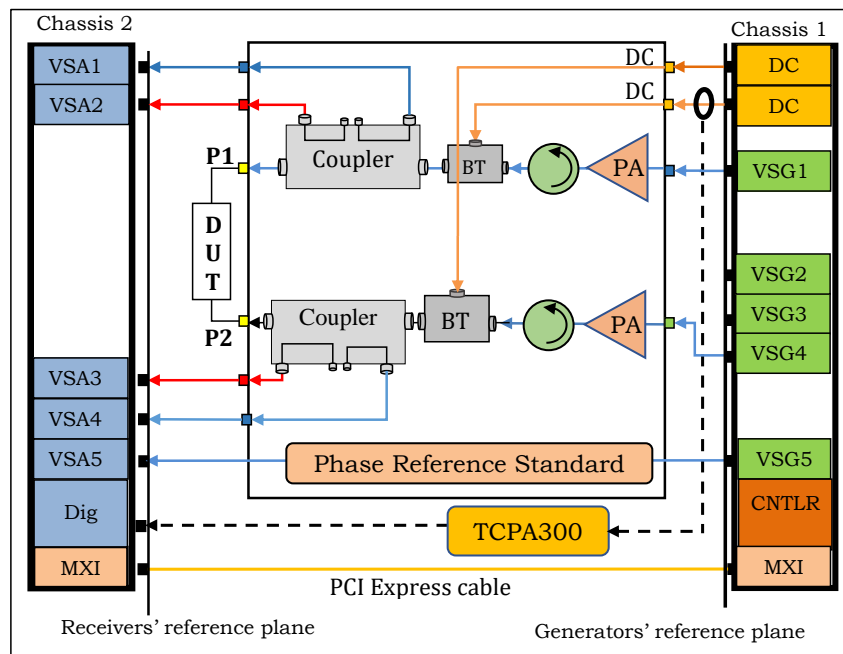


Figure 4.1: System configuration of the fundamental Load-pull measurement.

During the automated process, the decision for a measurement to be performed is paramount. Consequently, the automated measurement process follows simple and well-defined steps with continuous operational limit checks.

Figure 4.2 illustrates a simplified flow diagram of the whole measurement process.

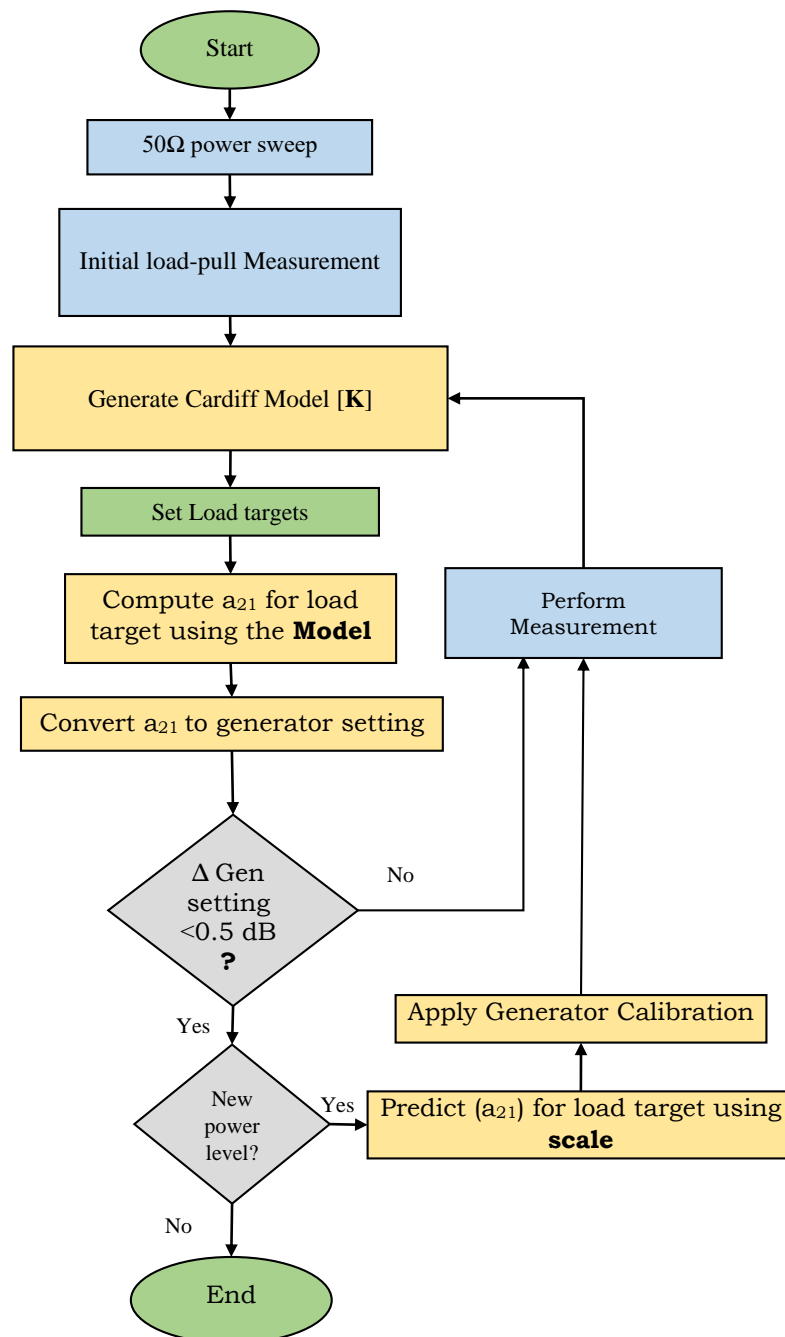


Figure 4.2: Flow diagram of the automated model-based active load-pull measurements

All of the operations and algorithms that have been included in the automated process have been implemented using LabVIEW software. According to the users preferences, the automated load-pull can locate optimum impedances required for the maximum output power or efficiency.

The process begins by placing the DUT into its safest operating point, here presumed to be the 50Ω system characteristic impedance that is standard in RF test- and characterisation. The initial power sweeps allow the suitable drive power range to be identified. The boundary conditions are used for an initial load-pull around the 50Ω system's impedance. Only small deviations from the centre of the Smith chart are performed here just sufficient to generate an initial nonlinear Cardiff model. The nonlinear model is then utilised to drive the active load-pull system. This uses a set of target impedances on the Smith chart to compute the required values for the load-pull signal to be injected to scan the desired impedance area. The use of a nonlinear model allows us to account for the DUT nonlinearities and eliminate any load-pull iteration within an impedance area for which the model has been generated. In case the targeted impedance space lies outside the definition of the Cardiff model, the software approaches the problem in multiple steps. The number of steps

depends on how far the Cardiff model is allowed to predict DUT nonlinear behaviour outside of its definition space. This parameter is a setting parameter within the system software. Any new measurements are continuously added to the Cardiff model, hence progressively expanding its definition area during the ongoing DUT characterisation.

This process assumes that no prior DUT characterisation took place and that no Cardiff model exists. However, if a model does already exist, then no initial power sweep or load-pull measurements are required.

4.2.1 INITIAL MEASUREMENTS

The automated load-pull process includes two initialisation steps: power sweep of the DUT, and initial load-pull grid measurement. The first measurement, which is terminated by the system's characteristic impedance, is performed to define a valid input power range over which load-pull sweeps can be performed and allows for an initial estimation of device gain. Typically, the maximum drive power is set to a value that limits the gain compression to -1 dB because it is within the range of the designer's interest. This sweep is also

exploited for computing system reflection coefficient Γ_L —which will be detailed in section 4.3—and ratio of the device response between successive measurements, which are essential for automated load-pull measurement over different drive power levels a_{11} at the input, section 4.2.4.

The second measurement of the automated process is the initial load-pull measurement grid, which is shown in Figure 4.3. This measurement is set around 50Ω while its maximum point is based on a $|a_{21}| = 10 - 20\%$ weighting of the measured fundamental reverse travelling waveform at the fundamental frequency $|b_{21}|$. The percentage that is applied to $|a_{21}|$ has been selected to keep the load-pull grid as close as possible to the 50Ω region, where the computed $|b_{21}|$ is still valid while the load impedances are still clearly differentiable. There are no specific impedance targets for this initial impedance sweep but the objective here is to obtain localised load perturbation around the 50Ω system characteristic impedance. Typically, a spiral shape is used for the injected $|a_{21}|$ signal grid because various magnitude and phase can be covered within the measured area efficiently, which enables a better load-based model to be generated [8].

4.2.2 LOAD-BASED CARDIFF BEHAVIOURAL MODEL

The initial load-pull measurements performed in the first steps are used to generate a load-based Cardiff model, as defined in Equation 4.1. Within the polynomial, the user-specified parameter M determines the model complexity while the $K_{p,q}$ values are the extracted model coefficients.

$$b_{21} = \sum_{D=0}^{D=1} \sum_{C=-(M-D)}^{C=+(M-D+1)} K_{|C|+2D,C} |\Gamma_{21}|^{|C|+2D} \left(\frac{\Gamma_{21}}{|\Gamma_{21}|} \right)^C \quad (4.1)$$

This is the previously published Cardiff model [7, 9, 10], which is reformulated to utilise impedance targets instead of the a_{21} travelling waveforms as the dependent variable. In order to extract the model coefficients, the least mean square algorithm (LMS) is involved, as illustrated in Equation 4.2, 4.3, and 4.4 to change the coefficient of the K matrix to allow for a computation of the model's best fit upon the provided measured data.

$$[b_{21}] = [\Gamma_{21}] \times [K] \quad (4.2)$$

$$[\Gamma_{21}]^H \cdot [b_{21}] = [\Gamma_{21}]^H \cdot [\Gamma_{21}] \cdot [K] \quad (4.3)$$

$$[K] = [\Gamma_{21}]^H [\Gamma_{21}] \cdot ([\Gamma_{21}]^H \times [b_{21}])^{-1} \quad (4.4)$$

The model's compatibility can be quantified by comparing the b_{21} predicted by the model to the b_{21} that been used to generate the model. Once the agreement between the two quantities is sufficient, the model can be used for the next impedance space. The quality of the generated model is affected by the model's complexity and measurement quantity, and also by the signal to noise ratio [10]. For example, if the number of load-pull measurement is less than the number of the exponents, then the model coefficient the LMS algorithm will not converge due to there being more unknown quantities than known quantities.

To define the required model order for the optimum impedance tracking process, several model complexities ranging from 3rd to 9th have been investigated. The result has been quantified by calculating the normalised mean square error (NMSE) Equation 4.5 [11] between measured and targeted loads as illustrated in Table 4.1.

$$NMSE = 10 \log \left(\frac{\sum |\Gamma_{meas} - \Gamma_{target}|^2}{\sum |\Gamma_{meas}|^2} \right) \quad (4.5)$$

The table shows that average error increases whenever a high order model is used during the optimum impedance tracking process. This refers to the intermodulation products that are generated through the measurement, in which third order model (relatively M=1 in Equ-

tion 4.1) would be convenient to present the measurement data with an average error around (-36 dB), while overfitting problem presents when 9th order is used.

Table 4.1: *NMSE of different Cardiff behavioural model complexities*

Complexity	3 rd	5 th	7 th	9 th
n	1	2	3	4
Error (dB)	-36	-35.3	-35.5	error

4.2.3 OPTIMUM IMPEDANCE TRACKING

If the impedance space, which is targeted during the load-pull measurements, lies outside the impedance area that was used to derive the Cardiff model, then the automated process switches to tracking the DUT performance utilising the variations located within a measured space. Here, the measured data are used to update the model while the local maximum of output power or efficiency are used as a starting point for the next set of target impedances. In essence, the automated process tracks these optimum values through a successive set of load-pull measurements until it reaches a global optimum, as shown in Figure 4.3.

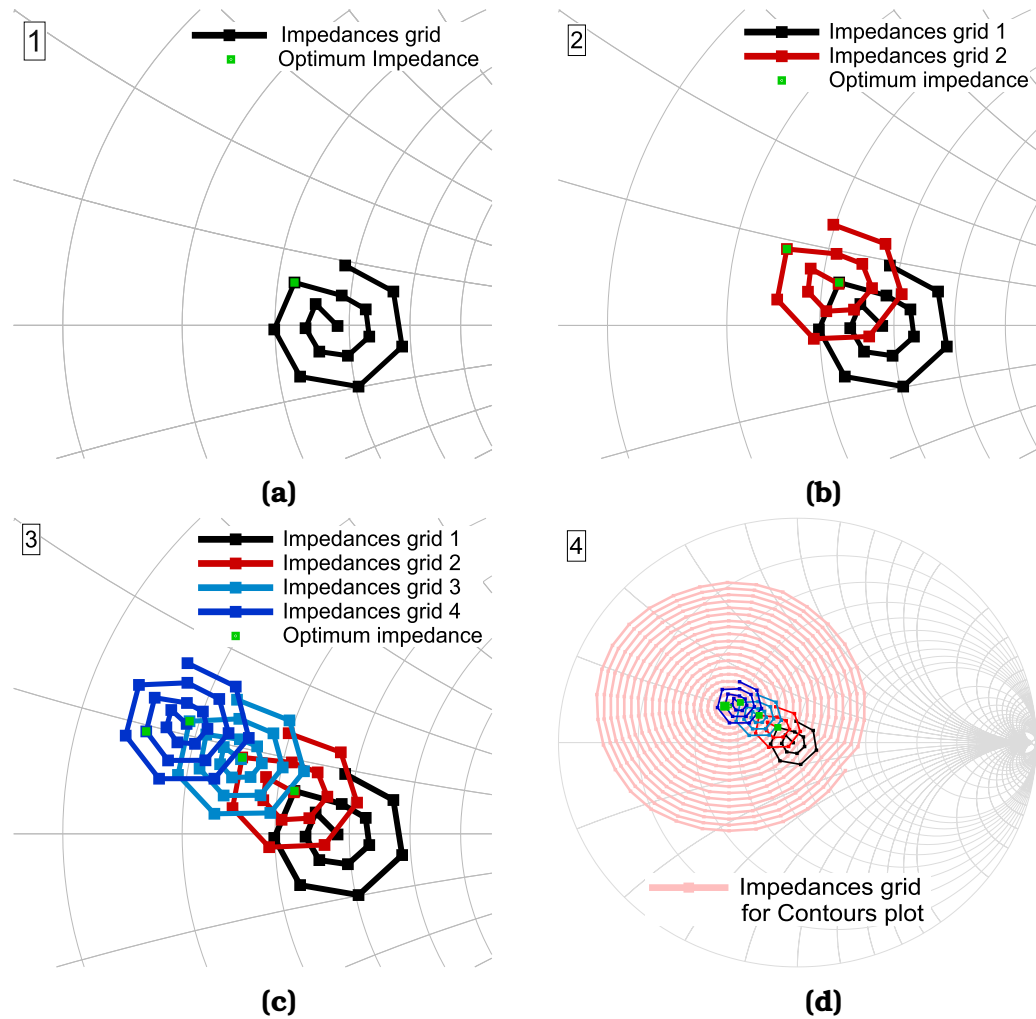


Figure 4.3: Example of the optimum impedance tracking process of 10W Cree device operating at 1GHz and class B condition and $a_{11} = 18.3dBm$

Here, the automated active load-pull measurement has been performed on a 10 W Wolfspeed packaged device at constant input drive power level, a 1 GHz operating frequency and a bias point $V_{GS} = -3.2$ V, $V_{DS} = 28$ V. To a certain degree, the Cardiff model can extrapolate the DUT behaviour beyond the measurement space [12]. The automated load-pull measurement somewhat relies on this model capability. As

shown in Figure 4.3, the successive load-pull grids are overlapping to ensure that the new set of target impedances is contained within the space over which the Cardiff model achieves correct extrapolation. In Figure 4.3, each new target grid is centred around the selected impedance that relates to the particular optimum the system is searching for. The maximum output power is calculated using Equation 4.6 [13], while the targeted grid size has been chosen to match the size of the previous grid.

$$P_{out} = \frac{|b_{21}|^2 - |a_{21}|^2}{2} \quad (4.6)$$

Once a new target location is decided, the device response b_{21} for those loads target impedance can be predicted using the previously generated load-based model $[K]$ by applying Equation 4.7 and then the required signal to be injected at the device reference plane a_{21} is computed using Equation 4.8.

$$[b_{21,pridected}] = [K] \cdot [\Gamma_{21,target}] \quad (4.7)$$

$$[a_{21,pridected}] = [\Gamma_{21,target}] \cdot [b_{21,pridected}] \quad (4.8)$$

To obtain a good prediction of the device response during the automated process, the model is generated by concatenating the previously measured data, as shown in Figure 4.4, achieving an NMSE between

measured and predicted b_{21} as low as -49.8 dB. The resulting NMSE error between target and measured loads is about -36dB.

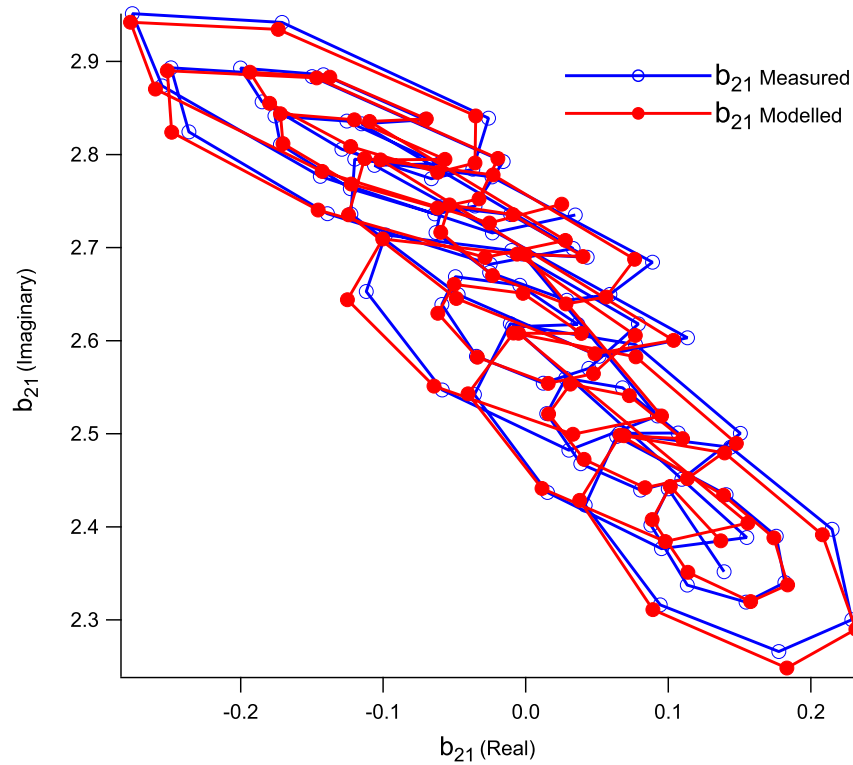


Figure 4.4: Comparison between concatenated measured and modelled b_{21s} when 3rd order model is used for load-pull measurement on a 10 W Cree device operates at 1 GHz and class B biasing point and $a_{11} = 18.3dBm$

It has been found that 15 measurements within each grid are sufficient to achieve successful tracking process. A further reduction of load impedances might cause an inaccurate determination of the optimum impedance.

To avoid excessive stress on the device due to high load reflection coefficients and to minimise the number of measurements, a comparison between targeted and predicted a_{21} values is continuously performed during the automated tracking process. Eventually, the model is re-populated with latest measurements and the same impedance space is re-measured. In case the new local maxima start decreasing, a final load-pull measurement is initiated that covers a larger impedance space to obtain relevant contour plots at a given power level; as shown in Figure 4.5.

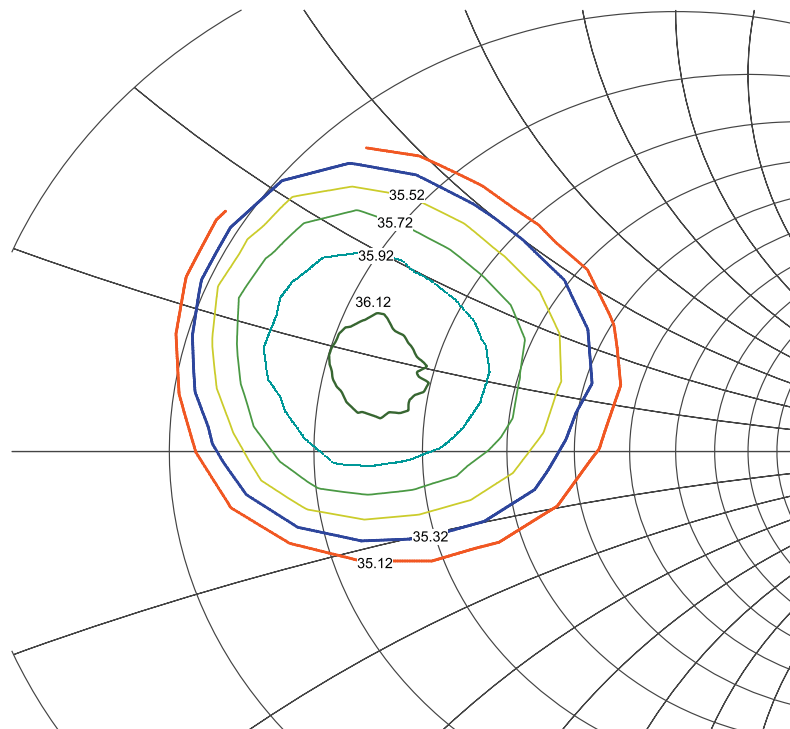


Figure 4.5: Load-pull power contours of 10 W Cree device at constant power level ($A_{11} = 18.3$ dBm) and 1GHz operating frequency. Bias point: $V_{GS} = -3.2$ V and $V_{DS} = 28$ V

The entire process of identifying the optimum contour plots as demonstrated here takes only a few seconds. In the case of the 10W Cree device, it took about 6.8 seconds (including a 50Ω power sweep grid consisting of 15 drive levels). It should be noted that in case the same device or similar is measured, then only the last step for the measurement of the contour plot is required [14]. In this case, the resulting measurement duration is only 1.4 sec, including pre-processing, acquisition, and post-processing of data.

4.2.4 LOAD-PULL OVER POWER-SWEEP

The realised tracking process assumes a constant drive power level. To facilitate load-pull measurements over a dynamic range, an efficient power scaling of the injected signal a_{21} is required. This is achieved using the scaling factor $S(i)$ computed during the 50Ω power sweep measurement; as briefly mentioned in section 4.2.1. These factors are the ratio between each two successive b_{21} measurements, as shown in Equation 4.9, where (i) is the drive power level index ($i > 0$), and PS referring to the power sweep measurement.

$$S(i) = \frac{|b_{(21,i)}|_{ps}}{|b_{(21,i-1)}|_{ps}} \quad (4.9)$$

This is used to predict the first power-scaled response of the measured device, as shown in Equation 4.10, with i representing a drive power level index while LP is an indication that the value was measured during the load-pull measurement. The underlying assumption here is that the curvature of a power sweeps remains relatively constant with the setting of the load impedance.

$$b_{(21,i)LP} = b_{(21,i-1)LP} \times S(i) \quad (4.10)$$

The power-scaled a_{21} values that are required for the load-pull at a different device drive level are obtained from the target impedances $[\Gamma_{21,Target}]$ of the previous power level. The resulting impedance grid is measured and then used to calculate a new load-based behavioural model. The same model is then populated by any new data that is produced by successive impedance sweeps that are necessary to identify a new optimum impedance region. An example of the power scaling is demonstrated in Figure 4.6.

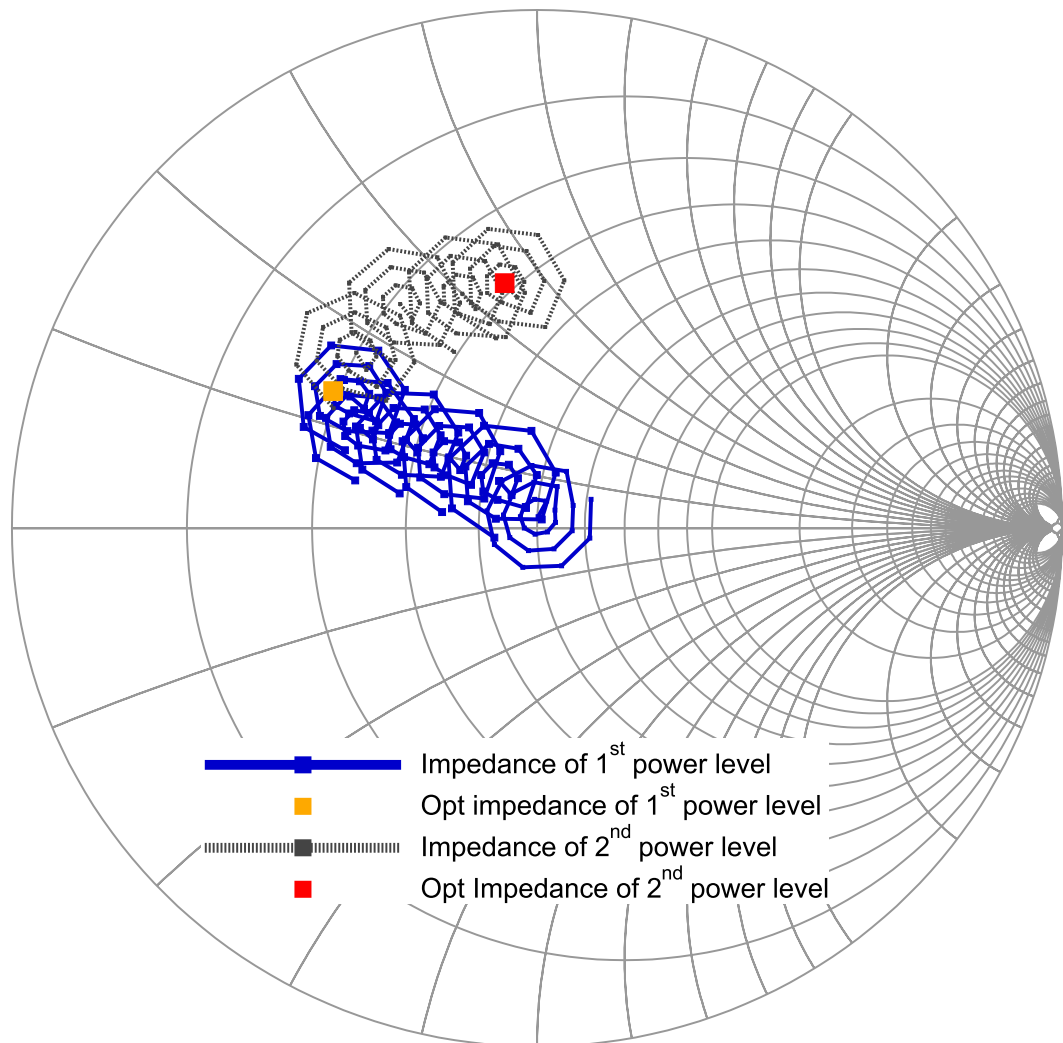


Figure 4.6: Tracking optimum impedances of the 10W Cree device for a two drive power levels ($A_{11} = 19.65$ dBm, and $A_{11} = 0.56$ dBm). Bias point: $V_{gs} = -3.2$ V, $V_{ds} = 28$ V. Fundamental freq. 1 GHz

Figure 4.6 depicts the continued tracking towards an optimum device impedance for a device drive power of 19.6 dBm after which the drive power is reduced to 0.56 dBm and a new tracking process is initiated. As can be seen, after a drop of the injected input power by about 19 dBm, a similar load-pull pattern is reproduced at virtually the

same location of the Smith chart. This power scaling process avoids any uncontrolled jumps in load-pull impedances for a large range of device input power values and ensures its safe operation during a fully automated load-pull process while greatly minimising the number of additional measurements. To give an example, an entire process of identifying optimum impedances at six different power levels, ranging from 5.6 to 19.6 dBm, which takes about 7.8 seconds.

4.3 CHARACTERISATION OF TEST-SET NONLINEARITIES

Two additional aspects have to be taken into account to achieve a good agreement between a target and measured impedances during the active load-pull measurements, which are: the measurement system mismatch, and the impact of the test-set components on the injected signal.

The system mismatch Γ_L , as illustrated in Figure 4.7, is caused by the imperfections of the load-pull components such as the circulator and the generator input impedance. The signal attenuation and gain also introduce a power dependent offset between the generator setting and the calculated a_{21} values at the measurement reference plane, which are required for the generation of targeted impedances.

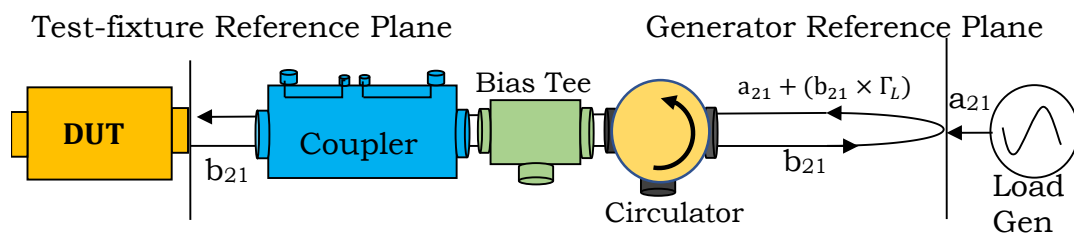


Figure 4.7: Illustration of the system's mismatch influence on the synthesised load impedance.

This mismatch is defined in Equation 4.11 with PS referring to the value being acquired during the power sweep step, which is performed at the beginning of the automated process. During this measurement, the load generator is off and only the source generator is on. In this case, there is an opportunity to measure the reflectivity of the load generator, wherein the reflected signal represents the $a_{21,ps}$ signal when the load generator is off, and $b_{21,ps}$ is the device output at the power sweep measurement. Thus, the value of the calculated Γ_L represents the reflectivity of the load generator. The signal contribution due to the measurement system mismatch Γ_L is taken into account using Equation 4.12.

$$\Gamma_L = (a_{21,ps}) / (b_{21,ps}) \quad (4.11)$$

$$a_{21,set} = a_{21,predicted} - a_{21,reflected} = a_{21,predicted} - (\Gamma_L \times b_{21,predicted}) \quad (4.12)$$

Several different approaches can be utilised in an effort to identify the power-dependent complex gain of the RF path within the test-set. A numerical technique [7, 15] allows us to compensate for any differences between the measured and target load values through the use of successive iterations. Relatively simple methods, such as Newton-Raphson (NR) algorithm, provide a robust and continuously improving approximation at the expense of a large number of iterations. To avoid the resulting drop in measurement's speed, an alternative approach

has been chosen. Within this work, the path of an injected signal has been modelled and then used to provide for an accurate link between the generator and measurement reference planes. Two different modelling approaches were investigated; a simple look-up table (LUT), and a behavioural model. These two methods have been implemented, verified, and embedded within the software of the presented measurement system.

4.3.1 LOOK-UP TABLE APPROACH

The look-up table approach is achieved using the measurement configuration that is illustrated in Figure 4.8. The setup includes all of the hardware required for the load-pull measurement to ensure that every loss and amplification is included in the model computation. This measurement requires port 1 and port 2 to be terminated to minimise unwanted signal reflections during the measurement of a travelling waves.

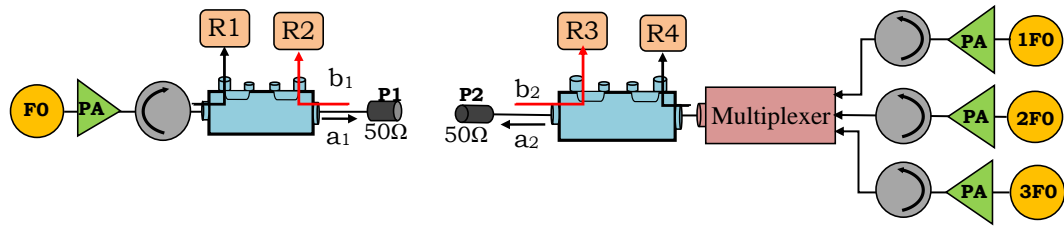


Figure 4.8: Generator calibration configuration

Given that the absolute AM-to-AM and AM-to-PM values of the load-pull power amplifier (LPA) exhibit relatively strong variations within the gain, especially when the LPA is driven at high power level. To keep the number of required measurements at a minimum, the utilised LUT model is based on choosing the nearest value to the desired power level. The table includes the indexed values of the measured a_2 as well as the phase and magnitude correction factors (CF). The values are then stored as correction factors, which are representing the magnitude and phase response of the RF test-set path.

$$CF = \frac{a_2}{a_{LP}} \quad (4.13)$$

The calculated magnitude CFs shown in Figure 4.9 (black trace) show a dependence on the gain of the LPA path. At the flat gain region, the value of the CFs are relatively constant, with an accelerating drop once the PA starts operating within the nonlinear region.

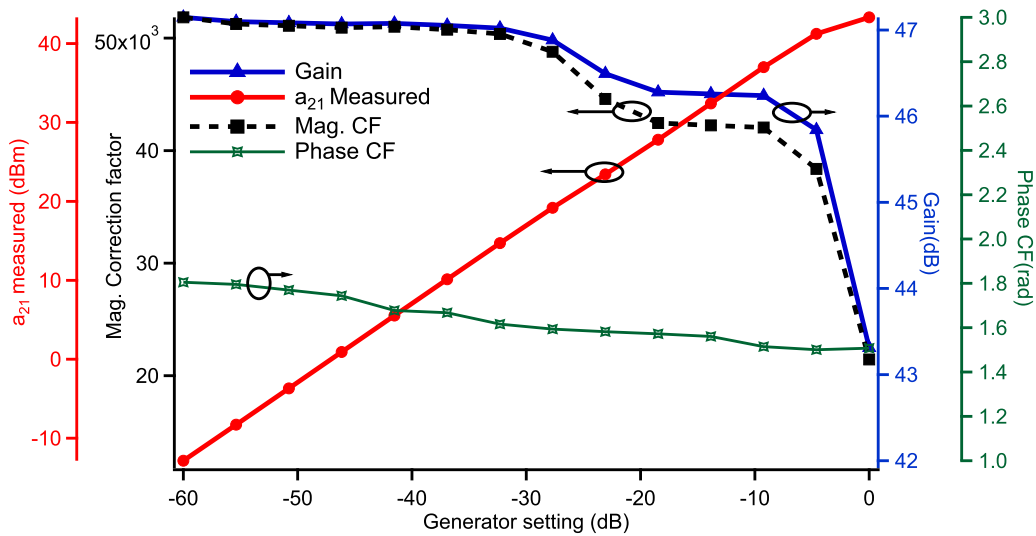


Figure 4.9: Generator setting versus a_{21} -wave measured, gain and associated correction factors of the PA.

The look-up table is used to translate the required a-wave signal at the DUT reference plane to its corresponding generator settings. For example, if the a-wave at the device reference plane is a_2 , then the related correction factor will be looked-up from the stored look-up table. To apply the correction factor, Equation 4.13 will be solved for a_{LIP} . The implementation utilises nearest value, therefore, for power values between the indexed a_2 data points, the nearest power index is looked-up and the associated magnitude and phase CF are used to compensate the loss and amplification through the signal path between the load-pull generator and the DUT reference plane.

To experimentally verify this approach over a set of generator settings, a direct comparison between the target and measured power points is illustrated in Figure 4.10. The comparison shows that both planes are almost identical after applying the generator calibration, with NMSE=-36 dB.

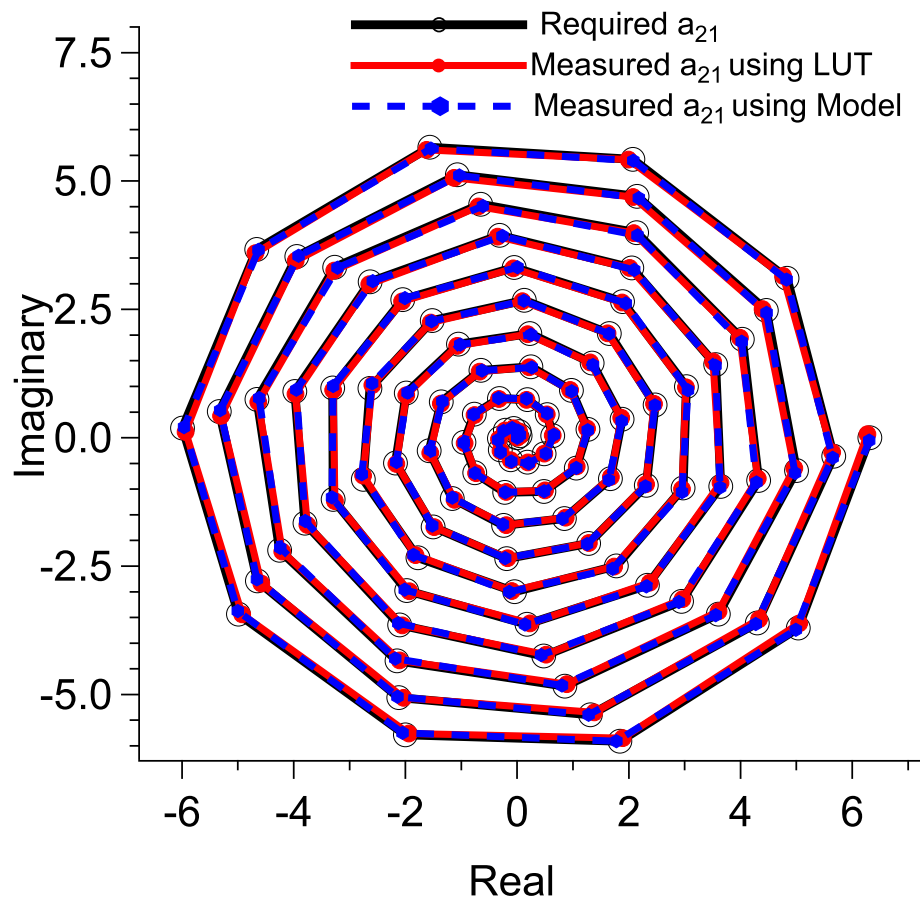


Figure 4.10: Practical verification of the model, and the LUT approach for predicting the generator setting

4.3.2 DESCRIPTIVE FUNCTION APPROACH

A polynomial equation can be used as an alternative approach to the look-up table to characterise the path of a DUT injected signal. The required measurement configuration to generate this model is the same as that shown in Figure 4.8.

Fundamentally, the nonlinear large-signal travelling wave response at the DUT output (a_2) of a PA in such measurement configuration is mathematically related to the generated travelling wave stimulus a_{LP} that is provided by the VSGs. The nonlinearity of the generated signal is a consequence of the PAs behaviour when driven at the high-power level. Therefore, the extracted model coefficient must quantify the generic relationship; $a_2 = F(a_{LP})$.

The load based-model Equation 4.1 that was mentioned in section 4.2.2, was specifically reformulated to Equation 4.14 to provide a simplified polynomial equation, where n is the equation order and K is the extracted model coefficients.

$$a_{LP} = \left(\frac{a_2}{|a_2|} \right) \sum_{n=0}^{n=\infty} K_{2n+1} |a_2|^{2n+1} \quad (4.14)$$

For the model generation, an a_{LP} spiral shown in Figure 4.11 is generated by the VSG and the a_2 response measured by a receiver (VSA) within the measurement system.

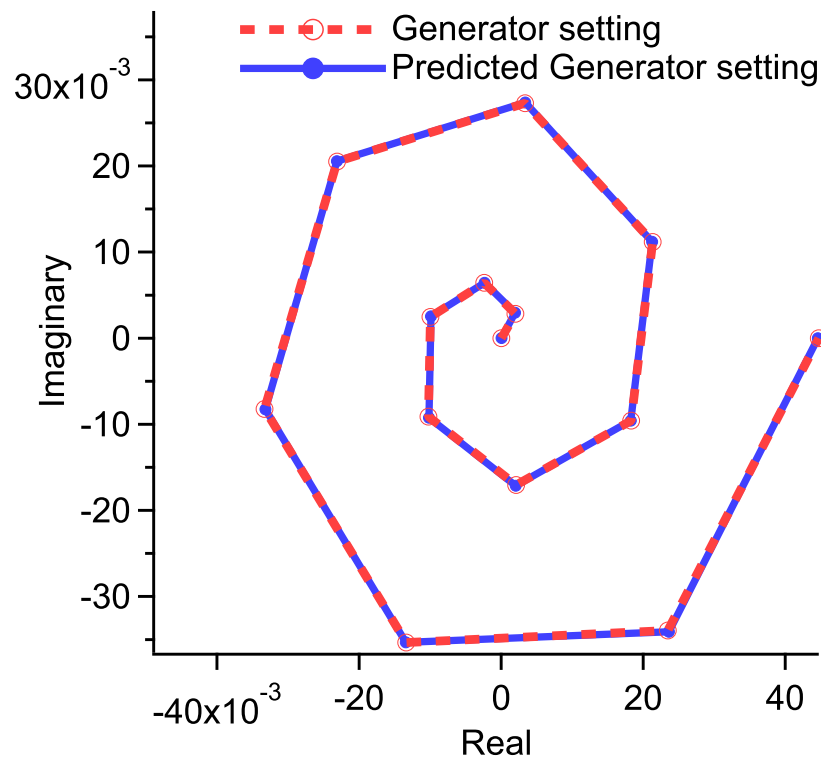


Figure 4.11: A 13th order generator calibration's model verification.

To achieve full utilisation of the load-pull power amplifier, the magnitude values span over the same dynamic range of the PA performance and within the compression region is shown in Figure 4.9. Typically, gain compression levels above 3 dB are avoided. This allows for the load-pull amplifiers to operate into their nonlinear regime and minimise their cost impact on the overall system.

Required model order has been investigated by computing the NMSE between the actual a_{LP} settings and the values predicted by the models. Table 4.2 show that minimum NMSE for the model is achieved when the 13th order is used, relatively (n)=6 in Equation 4.14. This has been shown clearly in Figure 4.11, where the high agreement between the actual a_{LP} settings and the values predicted by the model is achieved.

Table 4.2: Calculated NMSE from different model orders

Complexity	3 rd	5 th	7 th	9 th	11 th	13 th
n	1	2	3	4	5	6
Error (dB)	-25.1	-29.5	-34.7	-39.6	-44.34	-47

To practically verify the prediction of the generated model coefficient for an appropriate generator setting, a direct comparison between required and measured power points has been made and shown in Figure 4.10. The resulting difference in magnitude is shown in Figure 4.12.

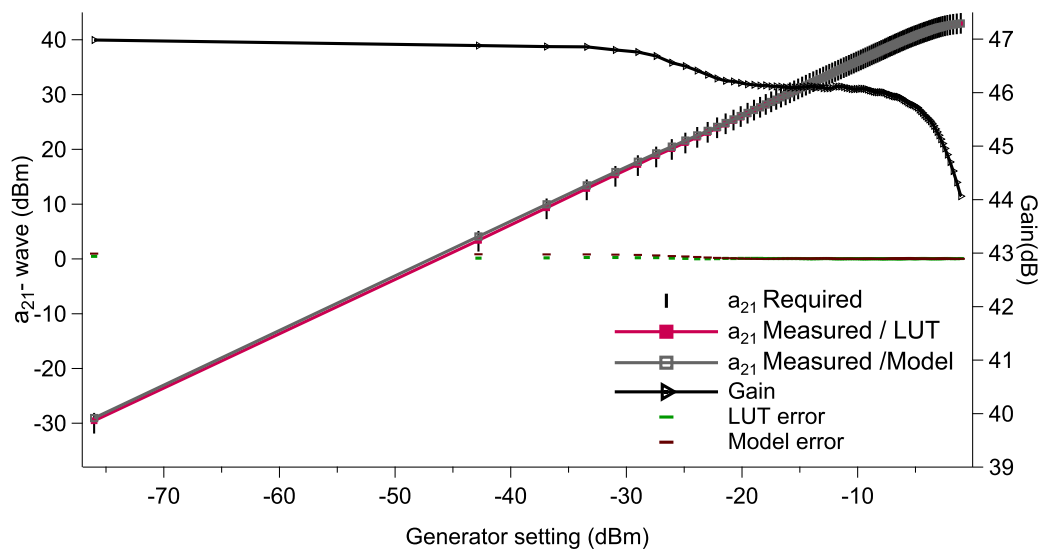


Figure 4.12: Comparison between required and measured a_{21} at a DUT reference plane

It is seen that excellent agreement is obtained over a dynamic range of 75 dB, including the 3 dB compression region of the PA, using a 13th order model. This figure illustrates also the average residual difference between target and measured powers for both the Cardiff model and the LUT, when they are obtained from the same power sweep shown in Figure 4.9 (i.e., 14 measurements are utilise. The average residual difference between target and measured powers is 0.1 dB for the Cardiff model. Meanwhile, when using the LUT, the average magnitude residual difference for the same number of measurements is slightly lower at approx. 0.06 dB.

This comparison has been expanded over a range of measurements, which is used for the generation of both models. The results are shown in Table 4.3.

Table 4.3: *NMSE comparison when different number of measurements are used to generate the Look-up Table (LUT) and Cardiff model (C.M)*

No. meas.	14	21	28	36
Er./C.M	-23.6	-23.5	-23.5	-23.4
Er./LUT	-23.3	-23.63	-23.7	-23.59

As can be seen, 14 measurements are sufficient for an accurate a_{LP} prediction. Both models exhibit similar error, approx. -23 dB, over the increasing number of measurements. In fact, the LUT model shows a slightly better overall performance, despite its simplicity.

The generated model has been experimentally used during a load-pull measurement to predict a generator setting required for emulating specific load targets on the Smith chart.

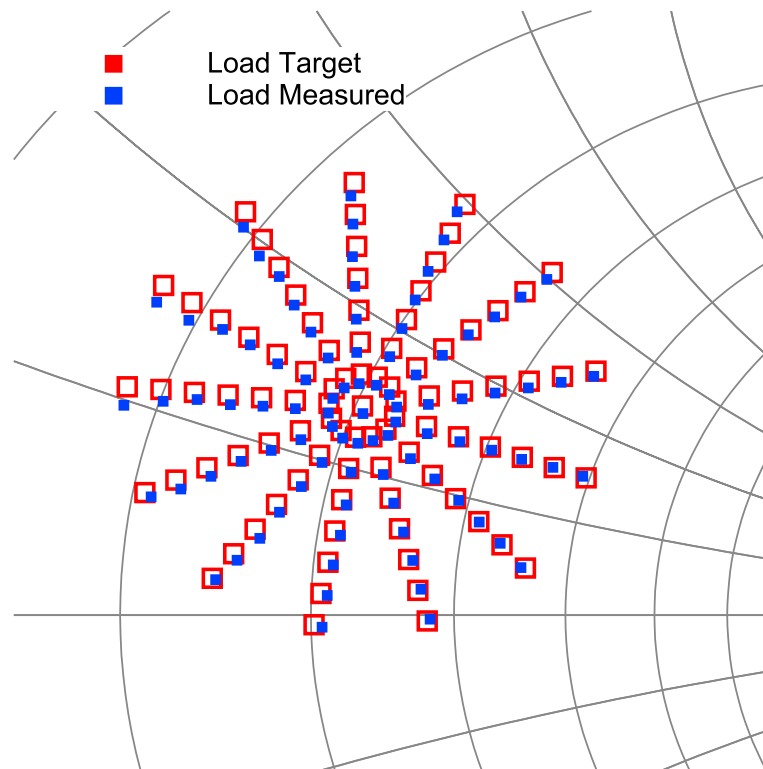


Figure 4.13: Comparison between target and measured loads at a DUT reference plane

Figure 4.13 shows clearly the agreement between the target and measured loads within NMSE equal to -34.4 dB. It should be noted that to obtain these results, a Cardiff model for DUT was employed to predict its nonlinear response. The DUT model constantly updates from any incoming measurement data. The comparison has shown again the high agreement between measured and targeted loads for a load-pull measurement performed on the 10 W Cree device at 1 GHz. The results might ultimately be a combination of both models (DUT and LPA) models.

4.4 SECOND HARMONIC LOAD-PULL

Upgrading the load-pull measurement capability to provide for harmonic load-pull is crucial for the nonlinear characterisation of RF devices. In particular, second harmonic load-pull capability would allow for the targeting of high efficiency PAs because it includes the optimum termination of the second harmonic impedance [16, 17].

Within the presented measurement system, an additional VSG has been assigned for the second harmonic signal while the triplexer, as shown in Figure 4.1, is used to combine the fundamental (a_{21}), and second harmonic (a_{22}) waves. The second harmonic load-pull measurement is carried out while the fundamental tone is kept at a constant at the optimum impedance for output power. All of the other higher harmonics were terminated into 50Ω . The flow graphs for performing this measurement are shown in Figure 4.14.

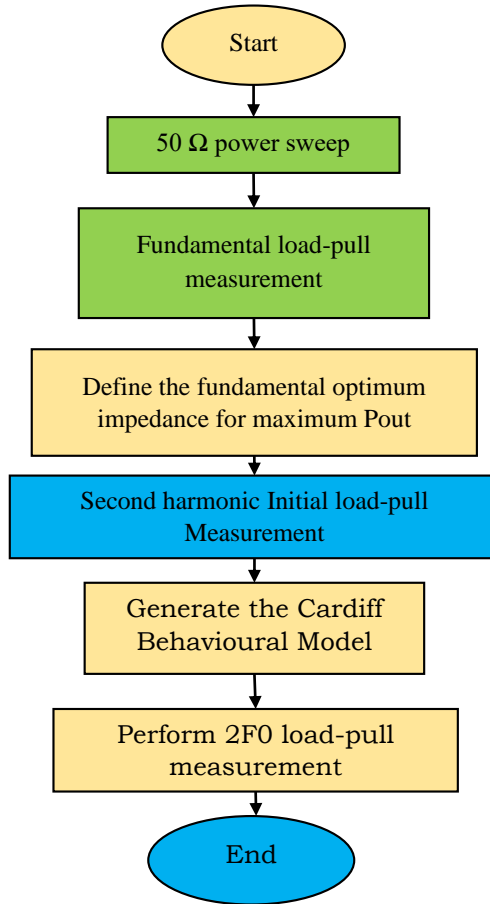


Figure 4.14: *The flow diagram of the 2F0 measurement*

This measurement is an extension of the fundamental load-pull measurement that was explained in section 4.2. To achieve a successful load-pull measurement at the second harmonic, the load-based Cardiff behavioural model Equation 4.1 has been reformulated to Equation 4.15.

$$b_{2h} = \sum_a \sum_b \sum_c \sum_d K_{a,b,c,d} |\Gamma_{21}|^a \left(\frac{\Gamma_{21}}{|\Gamma_{21}|} \right)^b |\Gamma_{22}|^c \left(\frac{\Gamma_{22}}{|\Gamma_{22}|} \right)^d \quad (4.15)$$

This equation is exclusive for a mixed load-based Cardiff behavioural model of the fundamental and second harmonic. The 'K' term is for the extractable coefficient while (a, b, c, d) are the associated exponents that are used for a model order. Table 4.4 shows an example of the exponents that have to be used when the mixed model of the F0 and 2F0 are 3rd and 1st respectively.

Table 4.4: Example of the mixed model exponents , (3rd order of F0 and 1st order of 2F0)

Exp. Index	1	2	3	4	5	6	7	8	9	10	11	12
$ \Gamma_{21} $ (a)	0	0	1	1	1	1	2	2	2	2	3	3
$\angle\Gamma_{21}$ (b)	0	0	1	1	-1	-1	2	2	0	0	1	1
$ \Gamma_{22} $ (c)	0	1	0	1	0	1	0	1	0	1	0	1
$\angle\Gamma_{22}$ (d)	0	1	0	1	0	1	0	1	0	1	0	1

Model generation of the second harmonic requires an initial load-pull measurement similar to the initial measurement of the fundamental load-pull. This measurement is set again around the 50Ω system impedance and the maximum power level for a_{22} set to (50-100%) of the b_{22} values that been obtained during the 50Ω power sweep. The maximum point has been selected to be sufficiently large to cover as large area as possible on the Smith chart while containing the load values within the passive impedance range. This would allow for the generation of a mixed model to predict the second harmonic response at any load condition.

An example of the initial second harmonic load-pull measurement is shown in Figure 4.15a, which clearly shows a skew within the distribution of the $2F_0$ harmonic loads. This initial data is then used to extract an updated Cardiff model. The resulting accuracy for setting $2F_0$ impedances across the entire Smith chart depends on the extrapolation capability of the generated mixed-model from the initial measurement. In this case, the second harmonic load targets are not sufficiently accurate, and a second iteration of the Cardiff model is computed utilising the additional data. Figure 4.15b shows the second harmonic load target after performing the second iteration.

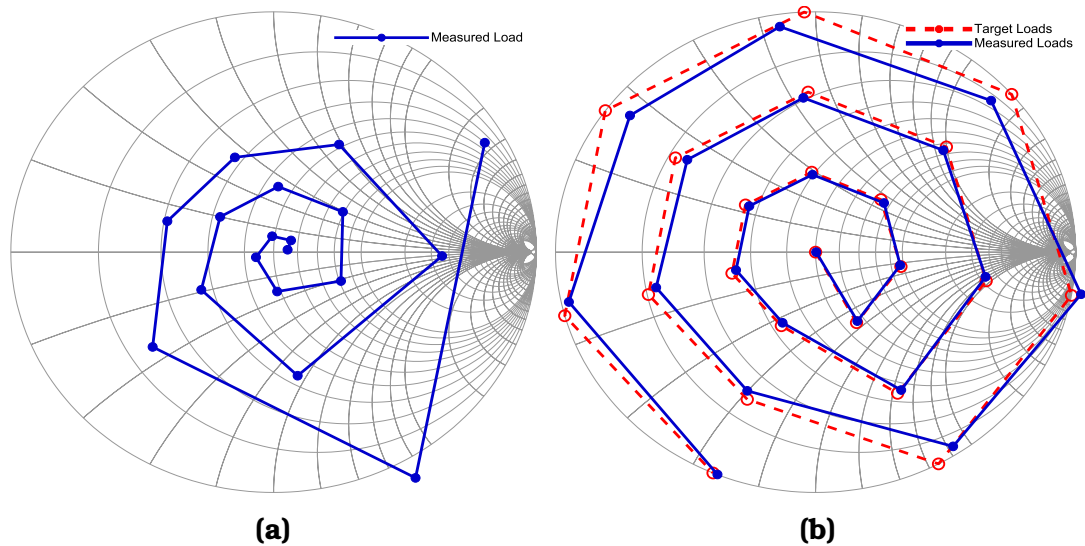


Figure 4.15: $2F_0$ Load-pull measurements, (a) initial load-pull measurements. (b) Comparison between measured and target $2f_0$ loads

Table 4.5 summarises the whole process of targeting several 2f0 loads on smith chart while using the load based mixed-Cardiff behavioural model.

Table 4.5: Summary of the second harmonic load-pull measurements

Iteration	Mag. of Γ_{22}	NMSE	Model Order	No. Measur.	Time(sec)
Initial	–	–	–	324	4
2 nd	0.7	-22.29	3 rd	+ 22	1.19
3 rd	0.9	-18.93	5 th	+22	1.19
4 th	1	-23.31	5 th	+22	1.03

4.5 CHAPTER SUMMARY

An integration of the load-based Cardiff behavioural model within a high-speed measurement system has achieved a fully-automated nonlinear measurement process for RF devices. Only 6.8 seconds are required to identify optimum impedances of an unknown device, including the plotting of its output power contours. The automated nonlinear characterisation process has been extended to include different drive power levels within one measurement session. To minimise the number of additional measurements, prior data from an initial power sweep has been utilised. Consequently, the identification of optimum impedances at five additional power levels takes less than 1.2 seconds, with a total of less than 8 seconds when including the load pull measurements of the first power level. In addition, the nonlinear measurements has been extended to include load-pull at harmonic frequencies. The results shows the ability of the mixed load-based Cardiff behavioural model to successfully predict the required injected signal for emulating a 2F0 load target located at $|\Gamma_{22}| = 0.7$ from the first iteration within an NMSE = -22 dB. The mixed model generation required for the second harmonic load-pull requires an initial measurement similar to the initial load-pull measurements that are performed during the fundamental load-pull measurement.

Moreover, an investigation of the different approaches for the modelling of the nonlinear RF test-set path has been carried out. The models have been experimentally validated under large-signal excitations and their performance compared. Both methods have shown a very good agreement between measured and targeted powers, wherein the average magnitude residual difference for the same number of measurements is 0.1 dB. It has been found that 14 measurements are enough to generate sufficiently accurate models with an average NMSE error at approx. -23 dB. This investigation has clearly demonstrated that increasing the complexity of the nonlinear models offers little to no benefit and suggests a straight-forward method for the further improvement of an open-loop active load pull system.

REFERENCES

- [1] H.-P. Test, "Measurement application note 95-1, s-parameter techniques for faster, more accurate network design," 1997.
- [2] A. Ferrero and M. Pirola, "Harmonic load-pull techniques: An overview of modern systems," *IEEE Microwave Magazine*, vol. 14, no. 4, pp. 116–123, June 2013.
- [3] M. Marchetti, "Mixed-signal instrumentation for large-signal device characterization and modelling," Ph.D. dissertation, Microelectronics & Computer Engineering, Delft University of Technology, 2013.
- [4] T. Williams, B. Wee, R. Saini, S. Mathias, and M. V. Bossche, "A digital, pxi-based active load-pull tuner to maximize throughput of a load-pull test bench," in *83rd ARFTG Microwave Measurement Conference*, June 2014, pp. 1–4.
- [5] M. Marchetti, T. Maier, V. Carrubba, S. Maroldt, M. Mußer, and R. Quay, "Examples of high-speed harmonic load pull investigations of high-efficiency gan power transistors," in *IEEE International Conference on Microwaves, Communications, Antennas and Electronic Systems (COMCAS)*, Nov. 2015, pp. 1–4.
- [6] R. E. Leoni, S. A. Harris, and D. G. Ries, "Active simultaneous harmonic source and load pull assisted by local polyharmonic distortion models," in *IEEE MTT-S International Microwave Symposium Digest*, May 2010, pp. 1166–1169.
- [7] R. S. Saini, J. W. Bell, T. A. J. Canning, S. P. Woodington, D. FitzPatrick, J. Lees, J. Benedikt, and P. J. Tasker, "High speed non-linear device characterization and uniformity investigations at x-band frequencies exploiting behavioral models," in *77th ARFTG Microwave Measurement Conference*, June 2011, pp. 1–4.
- [8] J. J. W. Bell, R. Saini, J. Lees, J. Benedikt, S. Cripps, and P. J. Tasker, "X-band behavioral model analysis using an active harmonic source- pull and load-pull measurement system," in *Asia-Pacific Microwave Conference*, Dec. 2011, pp. 1430–1433.
- [9] S. Woodington, T. Williams, H. Qi, D. Williams, L. Pattison, A. Patterson, J. Lees, J. Benedikt, and P. J. Tasker, "A novel measurement based method enabling rapid extraction of a rf waveform look-up table based behavioral model," in *IEEE MTT-S International Microwave Symposium Digest*, June 2008, pp. 1453–1456.

- [10] J. J. Bell, R. Saini, S. Woodington, J. Lees, J. Benedikt, S. Cripps, and P. J. Tasker, "Behavioral model analysis using simultaneous active fundamental load-pull and harmonic source-pull measurements at x-band," in *IEEE MTT-S International Microwave Symposium Digest*, June 2011, pp. 1–4.
- [11] F. M. Ghannouchi, O. Hammi, and M. Helaoui, *Behavioral Modeling and Predistortion of Wideband Wireless Transmitters*. John Wiley & Sons, Ltd, Jun 2015.
- [12] R. S. Saini, J. J. Bell, T. Williams, J. Lees, J. Benedikt, and P. J. Tasker, "Interpolation and extrapolation capabilities of non-linear behavioural models," in *78th ARFTG Microwave Measurement Conference*, Dec. 2011, pp. 1–4.
- [13] M. Thorsell, K. Andersson, and C. Fager, "Characterization setup for device level dynamic load modulation measurements," in *IEEE MTT-S International Microwave Symposium Digest*, June 2009, pp. 1197–1200.
- [14] R. S. Saini, J. W. Bell, T. A. J. Canning, S. P. Woodington, D. Fitz-Patrick, J. Lees, J. Benedikt, and P. J. Tasker, "High speed non-linear device characterization and uniformity investigations at x-band frequencies exploiting behavioral models," in *77th ARFTG Microwave Measurement Conference*, June 2011, pp. 1–4.
- [15] M. Thorsell and K. Andersson, "Fast multiharmonic active load-pull system with waveform measurement capabilities," *IEEE Trans. Microw. Theory Techn.*, vol. 60, no. 1, pp. 149–157, Jan. 2012.
- [16] P. J. Tasker and J. Benedikt, "Waveform inspired models and the harmonic balance emulator," *IEEE Microwave Magazine*, vol. 12, no. 2, pp. 38–54, April 2011.
- [17] D. J. Williams and P. J. Tasker, "An automated active source and load pull measurement system," in *6th IEEE High Frequency Postgraduate Colloquium*, Sep. 2001, pp. 7–12.

CHAPTER 5

AUTOMATING THE DETERMINATION AND VERIFICATION OF NONLINEAR BEHAVIOURAL MODELS

5.1 INTRODUCTION

A robust and reliable dataset for behavioural model extraction is crucial. This data would provide an accurate prediction for a behavioural model and, therefore, would support an accurate design process. In this work, because an accurate prediction of the power amplifier's output power and drain efficiency as a function of load impedance is critical for the design, a set of measurements along load-pull power and efficiency contours has been considered as the optimum dataset for the behavioural model extraction. Extracting these contours accurately and directly from the measurement data requires a high number (>100) of measurements because there is no prior knowledge about their locations. This process can thus be very

time consuming and measurement strategies that can considerably speed up this process are crucial.

This chapter introduces a strategy that allows for the rapid identification of load-pull power and efficiency contours by further exploiting the load-based Cardiff behavioural model formulation. The presented strategy allows for a direct comparison between measured and predicted contours, which enables the model to be verified. Moreover, the presented approach has been extended to automatically define the output power contours, and hence generate verified behavioural model over different input power levels while targeting a specified accuracy tolerance. In this chapter, the high-speed nonlinear measurement system that was presented in chapter 3 will be used to carry out measurements on a 10 W Cree device operating at 1 GHz frequency, at a class B bias point.

5.2 OPTIMUM DESIGN SPACE SEARCH ALGORITHM

Automating the accurate extraction of the behavioural model is an extension to the automated process of defining the optimum impedance for maximum output power. Figure 5.1 shows the generic flow diagram of the load-pull measurement scenario that is used to define the optimum dataset that will be used to generate a CAD behavioural model.

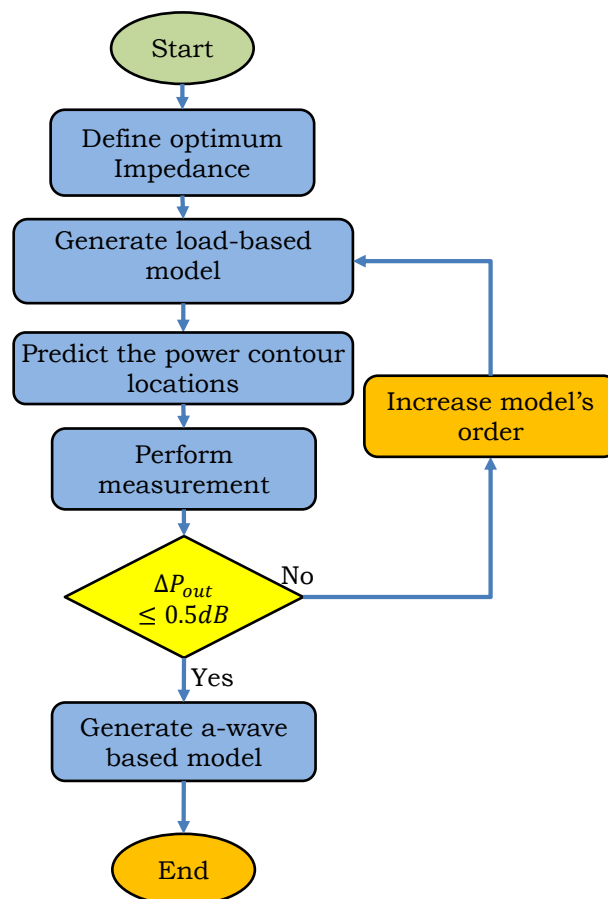


Figure 5.1: Generic flow diagram of the optimum design space search algorithm.

Once the location of the load for maximum power is determined, as shown in Figure 5.3 (gray color), the next step is to identify an appropriate load-pull dataset to generate the CAD behavioural model. Here, the same nonlinear model that was generated during the identification of the optimum impedances can be employed to predict the injected signals a_{21} that are required for specific power contours. In this case, we target the set of load-pull measurements that provide constant power.

The initial dataset is predicted using the 3^{rd} order load-based model as defined by Equation 5.1. The model extraction is performed with the previously measured load-pull data that was used to determine the location of maximum output power.

$$b_{21} = \sum_{D=0}^{D=1} \sum_{C=-(M-D)}^{C=+(M-D+1)} K_{|C|+2D,C} |\Gamma_{21}|^{|C|+2D} \left(\frac{\Gamma_{21}}{|\Gamma_{21}|} \right)^C \quad (5.1)$$

A 3rd order load-based behavioural model is defined for M=1; hence, six $K_{x,y}$ coefficients are extracted, as shown in Equation 5.2:

$$\begin{aligned}
 b_{21} = f(\Gamma_{21}) = & K_{0,0} \times |\Gamma_{21}|^0 \left(\frac{\Gamma_{21}}{|\Gamma_{21}|} \right)^0 + K_{1,1} \times |\Gamma_{21}|^1 \left(\frac{\Gamma_{21}}{|\Gamma_{21}|} \right)^1 + \\
 & K_{1,-1} \times |\Gamma_{21}|^1 \left(\frac{\Gamma_{21}}{|\Gamma_{21}|} \right)^{-1} + K_{0,2} \times |\Gamma_{21}|^0 \left(\frac{\Gamma_{21}}{|\Gamma_{21}|} \right)^2 + \\
 & K_{2,2} \times |\Gamma_{21}|^2 \left(\frac{\Gamma_{21}}{|\Gamma_{21}|} \right)^2 + K_{3,1} \times |\Gamma_{21}|^3 \left(\frac{\Gamma_{21}}{|\Gamma_{21}|} \right)^1
 \end{aligned} \quad (5.2)$$

The power contours prediction can be achieved by a set of calculated load targets centred around the location of the maximum output power and covering a wide area on the Smith chart to guarantee inclusion of the -3dB compression region, as shown in Figure 5.2.

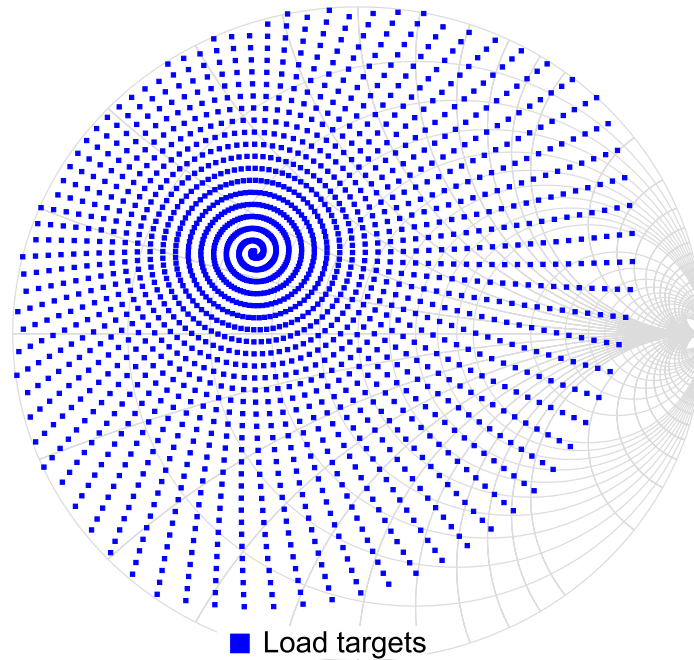


Figure 5.2: A set of load targets on Smith chart required to define the load-pull power contours.

Because b_{21} is predicted by the load-based behavioural model, a_{21} , the corresponding output power data points can be computed using Equation 5.3 and 5.4, respectively.

$$a_{21,predicted} = \Gamma_{21,target} \times b_{21,predicted} \quad (5.3)$$

$$P_{out,predicted} = \frac{b_{21,predicted}^2 - a_{21,predicted}^2}{2} \quad (5.4)$$

The predicted P_{out} can be exploited to filter out the targeted power contours locations, as shown in the example in Figure 5.3. This greatly reduces the number of a_{21} signals that are required for the measurement of output power contours.

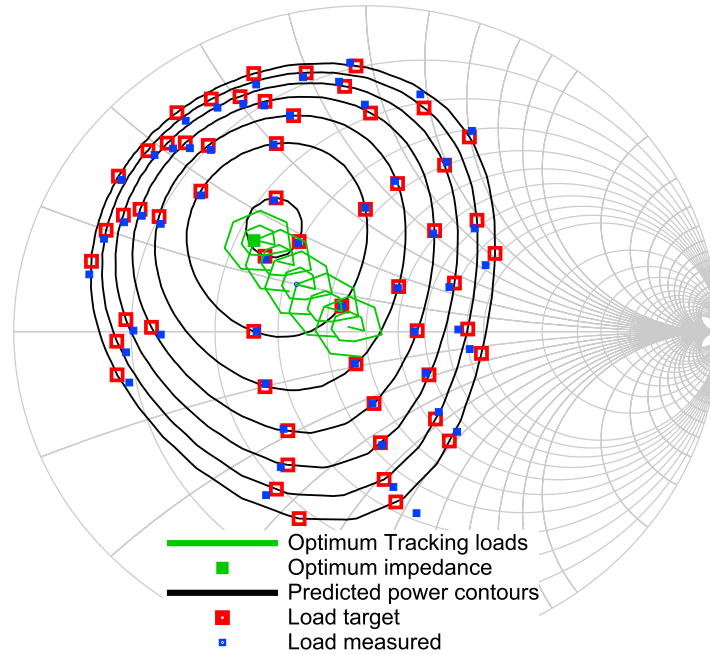


Figure 5.3: Initial prediction of the power contours using the 3rd order load-based model.

The locations of the predicted power contours are now targeted directly during the load-pull measurements instead of measuring a large grid. In this case, the number of the load-pull impedance measurements that cover the -3 dB power contour region can be reduced without compromising the accurate extraction of the behavioural model, while at the same time meeting the requirements for model verification. For example, a 7th order model in theory, in case of appropriate data point selection, requires only 14 measurements because the number of coefficients is 14.

Figure 5.3 shows an example of the chosen load impedances (red markers) that will be used to determine the selected power contours. The selected 36 impedance points are more than sufficient for the extraction of the 7th order model. The first guess using 3rd order model does not accurately predict the power contours, as shown in Figure 5.4, where a comparison between 36 measured and targeted load locations shows that the NMSE is about -12.9 dB.

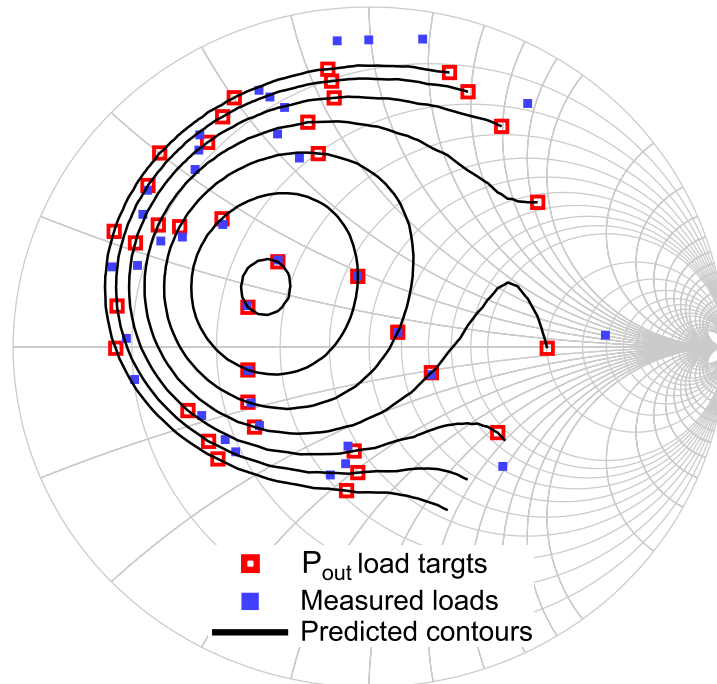


Figure 5.4: Comparison between predicted and measured power contours of 10 W Cree device at 1 GHz operating frequency and class B bias point for the first iteration while using 3rd order model.

The accuracy of predicting the location of the load-pull contours has been displayed in Figure 5.5, which shows the difference between predicted and measured b_{21} and P_{out} along all the targeted contours.

Figure 5.5 shows that the residual difference between P_{out} predicted and measured is presently more than 6 dB. The disagreement between actual and predicted measurements is linked to the extrapolation limitation of the 3rd order load-based behavioural model when extending beyond the 1 dB power contour.

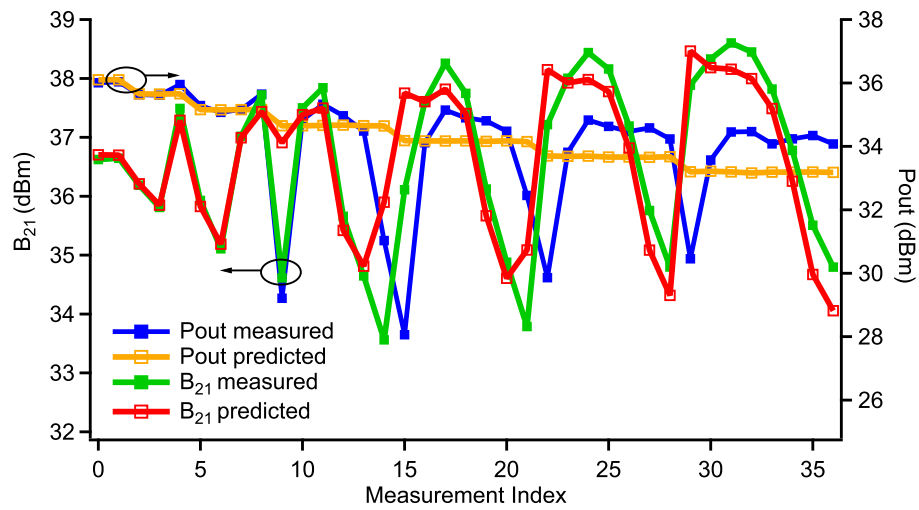


Figure 5.5: Comparison between predicted and measured P_{out} and b_{21} at 1 GHz and constant $A_{11}=19$ dBm, using 3rd order load-based behavioural model.

To address this error, the automated process now performs a second load-pull iteration. In this case, the new measured dataset shown in Figure 5.4 (blue markers) will be used to extract an improved, higher order, load-based behavioural model. A 5th order (i.e. $M=2$ in Equation 5.1) is now used. This new model is used to update the array of Γ_{21} load targets of the selected power contours.

The measurement results show that in this iteration most of the load-pull impedance targets have been achieved with the NMSE being reduced to about -33.6 dB. In this case, the worst-case comparison between predicted and measured P_{out} shows that the maximum difference is now reduced to about 0.7 dB. This enhancement is due to

both exploiting an improved set of measurement data, better covering the target power contours, and a model with increased complexity (i.e. higher order). This is achieved with a relatively small number of measurements. It is interesting that just repeating the characterisation process from the same model order did not yield any significant improvements. This is the reason why the model order increased straight after the model failed to meet the required accuracy.

Because the agreement between predicted and measured P_{out} is still not within the tolerance of 0.5 dB, a third load-pull iteration will be performed. Again, a model with complexity is increased now to 7th order, is extracted using the new dataset and is then used to compute a new set of load locations on the targeted power contours. Figure 5.6 shows the result of the third iteration. There is now excellent agreement between targeted and measured load impedances.

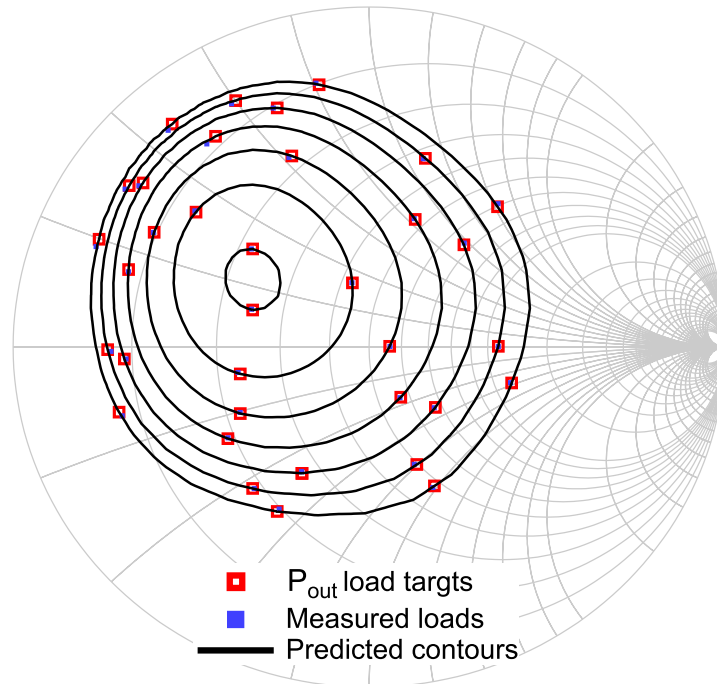


Figure 5.6: Comparison between predicted (red markers) and measured (blue markers) loads of 10 W Cree device operating at 1 GHz frequency and class B bias condition. A 7th order load-based behavioural model is used.

The NMSE is now reduced to -35.1 dB, while the worst-case comparison between measured and predicted P_{out} is less than 0.5 dBm; as shown in Figure 5.7. The total number of measurements required to accurately define the power contours region, up to -3 dB, was only (75+3×36=183) measurements; including the load-pull data that was measured to identify the optimum impedance.

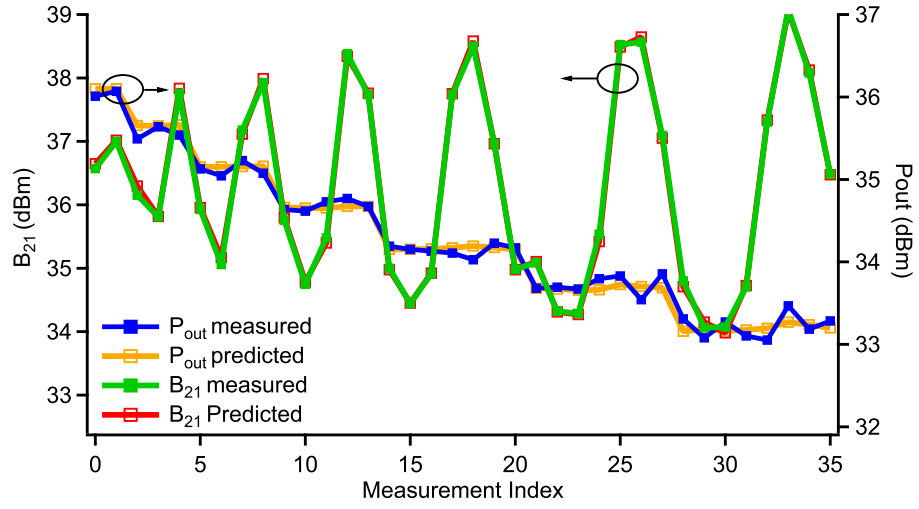


Figure 5.7: Comparison showing the prediction of the load-pull contours and the measured load locations at 1GHz, while using the 7th order model.

5.3 PREDICTION OF THE EFFICIENCY CONTOURS

The direct measurement of the output power contours can be accompanied by drain efficiency contours. This can be achieved by computing the drain efficiency as a function of load, as illustrated in Equation 5.5

$$[b_{21} \quad I_{20}] = \sum_{D=0}^{D=1} \sum_{C=-(M-D)}^{C=+(M-D+1)} K_{|C|+2D,C} |\Gamma_{21}|^{|C|+2D} \left(\frac{\Gamma_{21}}{|\Gamma_{21}|} \right)^C \quad (5.5)$$

This equation is an updated version of the load-based behavioural model equation 5.1, where the efficiency is computed using b_{21} and DC output current (I_{20}), and power, using b_{21} , is used to define load

locations that now target both power and efficiency contours. Similar to the prediction of power, the efficiency model is updated through iterations to achieve a good agreement between predicted and measured efficiency; hence, once again the appropriate data for the model extraction can be achieved.

To speed up the process, the measurement of efficiency and output power contours is performed in parallel. Model coefficients are extracted using the least mean square algorithm (LMS), as illustrated in Equation 5.6 to 5.8:

$$[b_{21} \quad I_{20}] = [\Gamma_{21}] \times [K \quad K_E] \quad (5.6)$$

$$[\Gamma_{21}]^H \cdot [b_{21} \quad I_{20}] = [\Gamma_{21}]^H \cdot [\Gamma_{21}] \cdot [K \quad K_E] \quad (5.7)$$

$$[K \quad K_E] = [\Gamma_{21}]^H [\Gamma_{21}] \cdot ([\Gamma_{21}]^H \times [b_{21} \quad I_{20}])^{-1} \quad (5.8)$$

Figure 5.8 shows the prediction of the efficiency contours resulted from the 4th load-pull iteration while using the 9th order load-based model.

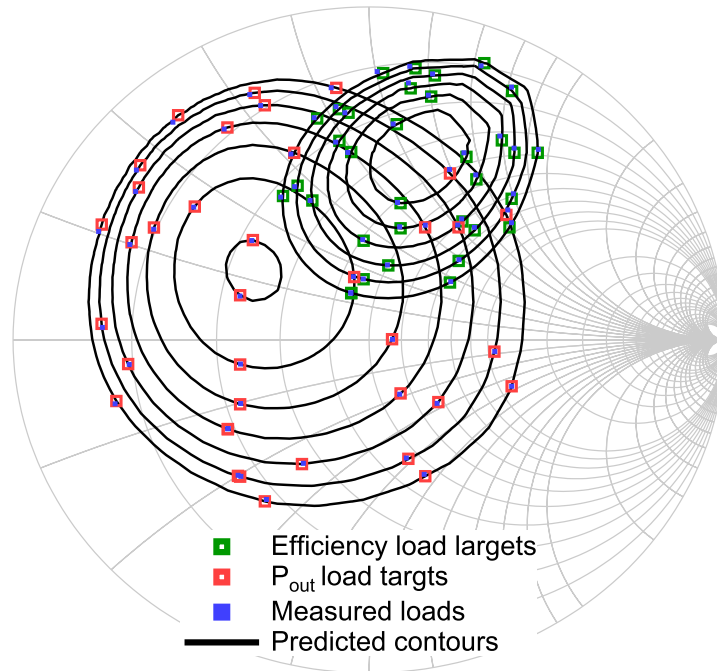


Figure 5.8: Comparison between the measured and predicted load-pull efficiency and the P_{out} contours of 10 W Cree device at 1GHz operation frequency and class B biasing condition when the 9th order load-based behavioural model is used.

The predicted efficiency and power contours have been compared to the measured values. Figure 5.9 shows that maximum difference between predicted and measured efficiency (ΔE) is less than 3%, while ΔP_{out} is less than 0.25 dB.

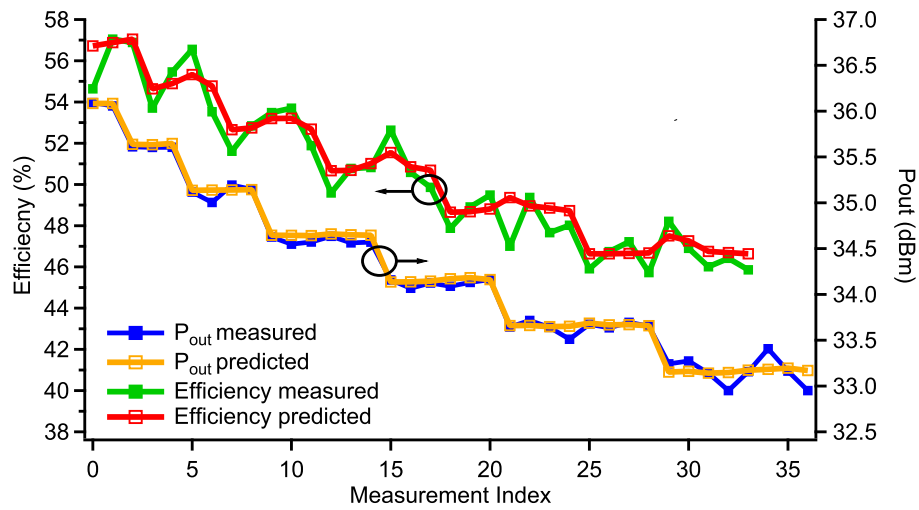


Figure 5.9: Comparison between measured and predicted efficiency and power contours of 10W Cree device at 1 GHz operation frequency and class B biasing condition when 9th order load-based behavioural model is used.

It is worth highlighting at this point that most of the differences between measured and predicted quantities are due to the slight disagreement between load targets and load measured, as shown in Figure 5.8. Moreover, the inclusion of the efficiency contours increased the number of measurements to 361, resulting in a measurement time of about 12 seconds. The measurement details are summarised in Table 5.1.

Table 5.1: *Measurement Summary.*

	Model Order	NMSE	ΔP_{out}	ΔE	No. Meas.
Define Opt.	3 rd	–	–	–	75
1 st Iteration	3 rd	-12.9	6.11	12.8	73
2 nd Iteration	5 th	-36.69	0.7	6.63	71
3 rd Iteration	7 th	-35.15	0.19	4.2	71
4 th Iteration	9 th	-35.15	0.22	2.35	71
Total number					361
Total time					12 sec

5.4 BEHAVIOURAL MODEL EXTRACTION AND VERIFICATION

A key design objective for the model is to accurately predict load-pull contours [1], a dataset targeting load locations on an array of power and efficiency contours within this design space was considered to be better than just the simple grid approach. In this optimal dataset, load-pull contour targeted measurements have been exploited in the extraction and verification of the conventional a-wave based Cardiff behavioural model [2, 3]. The a-wave based model format is a compatible CAD tool formulation [4]. Equation 5.9 shows the updated version of the a-wave based model formulation by which the I_{20} , hence, the efficiency can be predicted in addition to the prediction of b_{21} .

$$[b_{21} \quad I_{20}] = P \times \sum_{D=0}^{D=1} \sum_{C=-(M-D)}^{C=+(M-D+1)} L_{|C|+2D,C} |a_{21}|^{|C|+2D} \left(\frac{Q}{P}\right)^C \quad (5.9)$$

In this equation, P is the phase of the input a_{11} stimulus, while Q is the phase of the output a_{21} stimulus. The user defined parameter M , defines the model complexity, while $L_{p,q}$ are the extracted pairs of model coefficients required to determine b_{21} and I_{20} , respectively.

The necessary a-wave model order has been investigated by testing different values of M , beginning with $M=1$ (effectively 3^{rd} order) and ending with $M=5$ (effectively 11^{th} order) as shown in Table 5.2.

Table 5.2: Error of the model's complexity

Model Complexity	3^{rd}	5^{th}	7^{th}	9^{th}	11^{th}
n	1	2	3	4	5
Er. L.B.M(dB)	-34.8	-41.9	-46.9	-48	-48.4
Er. A.B.M(dB)	-44.2	-45.6	-47.7	-48.3	-48.9

A comparison confirms that the model's accuracy increases with increasing complexity. This new approach verified that, in this case, a Cardiff model with sufficient accuracy for CAD design can be achieved using a model with $M=5$ (effectively 9^{th} order). A model with only 18 coefficients. Figure 5.10 shows a comparison between measured and predicted load impedances associated with the targeted P_{out} and efficiency load-pull contours, found using 9^{th} order a-wave based model, in which the NMSE is approximately -45.8 dB.

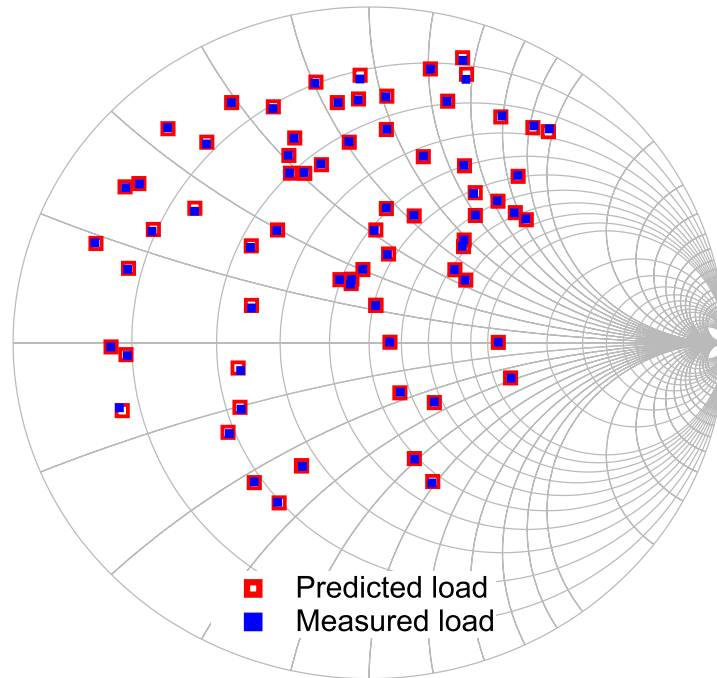


Figure 5.10: Comparison between the measured and predicted load-pull impedances associated with efficiency and power contours of 10 W Cree device at 1 GHz operation frequency and class B biasing condition when a 9th order a-wave based Cardiff behavioural model is used.

Figure 5.11 quantifies the quality of the a-wave based model by comparing the measured and modelled values of P_{out} , and also the drain efficiency. This verifies the excellent accuracy of the resulting Cardiff model within the -3 dB power contour design space with a maximum difference in P_{out} of about 0.12 dB and a 12% efficiency contour space with a maximum difference in efficiency (ΔE) of about 2.16%. It is worth mentioning that the 7th order a-wave based Cardiff behavioural model would be optimal if only the P_{out} contours are targeted wherein $\Delta P_{out} = 0.12$.

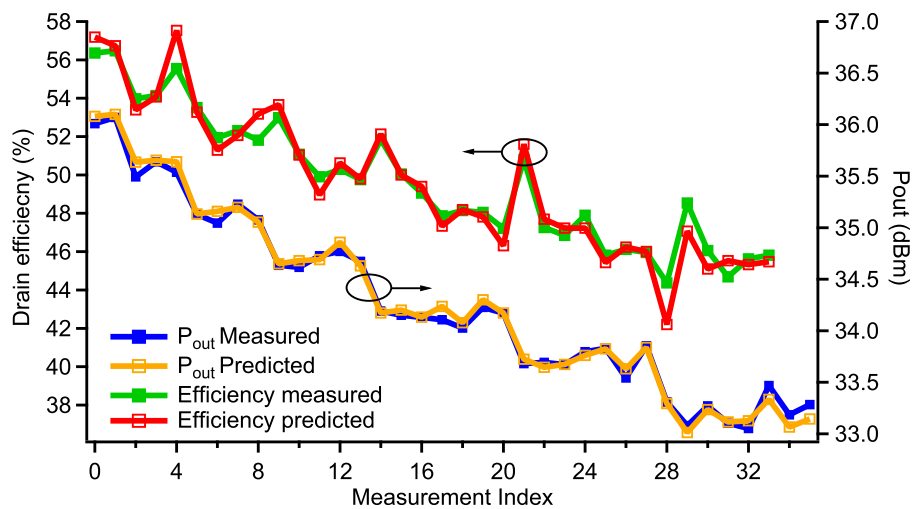


Figure 5.11: Comparison between the measured and predicted load-pull efficiency and power contours of 10 W Cree device at 1GHz operation frequency and class B biasing condition when a 9th order a-wave based Cardiff behavioural model is used.

5.5 POWER CONTOURS OVER DIFFERENT INPUT POWER LEVELS

The ideal modelling process is achieved once the extracted model is constructed by reliable data in which targeted operating conditions are covered. Variation of the operating conditions allows the PA designer to investigate a wide design space; hence, ensuring that the best PA design is achieved. This kind of modelling process typically requires a large number of measurements, hence can be very time consuming [5]. Therefore, minimising the number of measurements required for

modelling process would allow for time saving, hence, more operating conditions to be included.

Consequently, the process that has been introduced and described in section 5.2 can be extended to define the optimum design space and extract the CAD model over different power levels within one measurement session while still providing for a robust and verified model extraction. This kind of measurement has been realised by exploiting the same approach that has been mentioned in chapter 4 section 4.2.4 where b_{21} scaling was used to define the required injected signal (a_{21}) for the load-pull at a new power level. Figure 5.12 shows the generic flow diagram of the measurement scenario where load-pull data targeting power contours at different input power levels can be achieved within one measurement session.

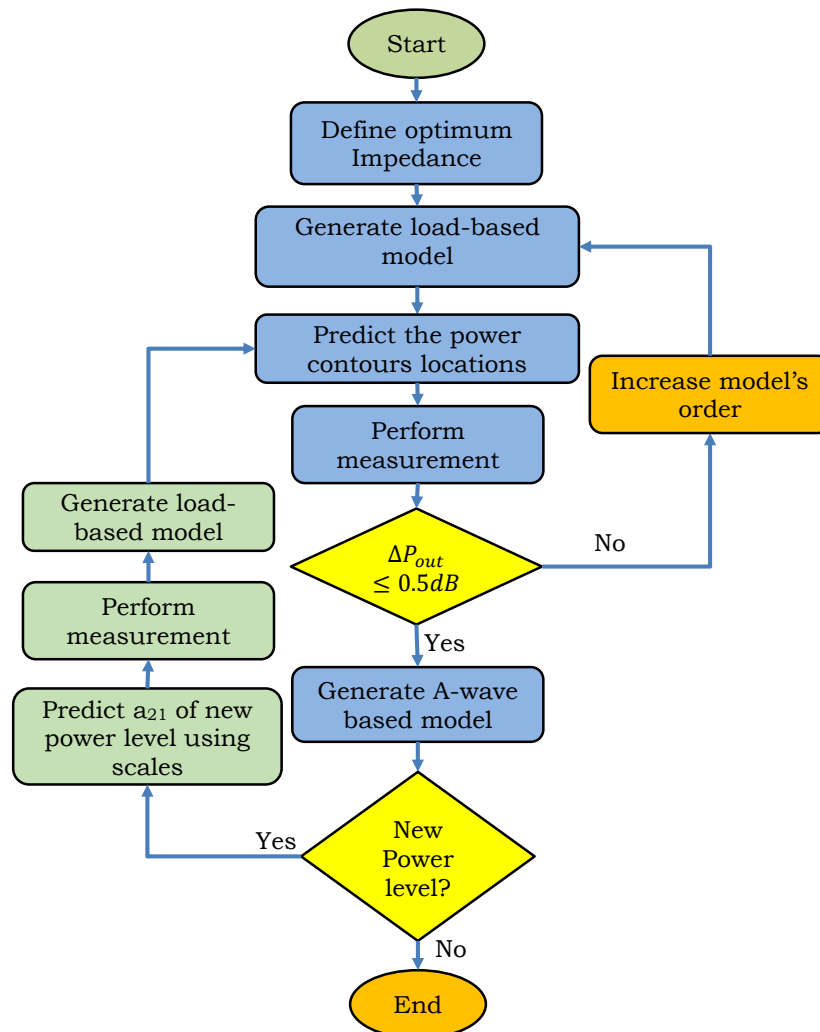


Figure 5.12: Generic flow diagram of the automated load-pull process for different power level.

The first load-pull measurements, which rely on the scaling approach have been considered as initial measurements of the new power level. The initial measured data is used to generate the associated load-based behavioural model by which the second load-pull measurement will be driven, and P_{out} contours are predicted. In this case, the second load-pull measurements target the impedance locations that are associated

with the desired P_{out} contours. This would allow for measurement verification by comparing the P_{out} predicted with the actual value. Once the comparison between measured and predicted P_{out} of the new power level is within the tolerance (0.5dB), the measured data would be used to generate the A-wave based model.

An example of load-pull measurements over 15 different input power levels has been performed on 10W Cree device ranging from (A11=18.3 dBm, A11=13.3 dBm, A11=4 dBm). The total number of measurements required to define the desired power contours for 15 power levels is 1191 measurements. This number is a result of three measurement groups: one performed for the first power level which is about $(75+3 \times 36=183)$ measurements; the second is required for the first iteration for each power level step which is $(36 \times 14=504)$; with the same number executed within the second iteration $(36 \times 14=504)$. The total time consumed for performing these $(183+504+504=1191)$ measurements is about 1 minute. This time includes the load-pull measurements, the data analyses and the time to generate the a-wave based model required for the CAD tool design.

Because showing all power contours of 0.5 dB step for 15 power level in single plot is not sensible, only the centre and the -3dB power contour are plotted in Figure 5.13 for three selected power levels ranging between the maximum and minimum ($A_{11}=18.3$ dBm, $A_{11}=13.3$ dBm, $A_{11}=4$ dBm)..

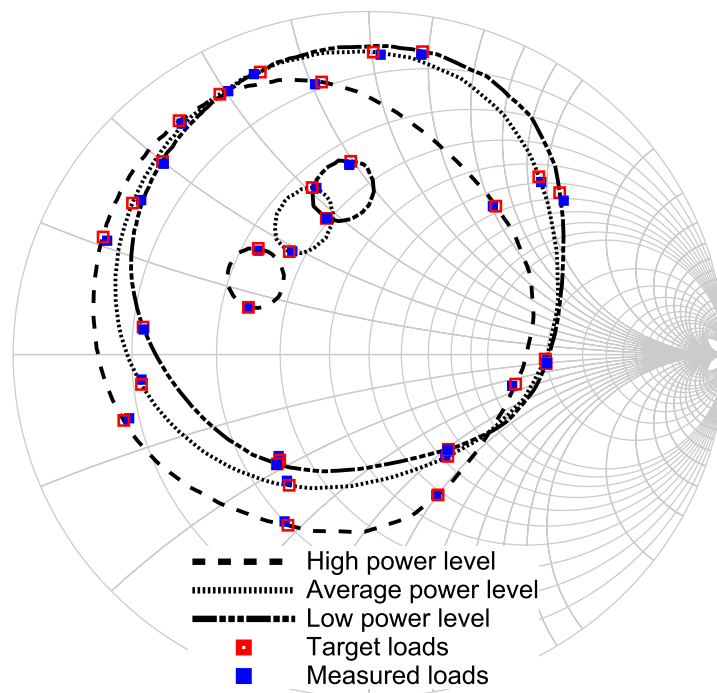


Figure 5.13: Comparison between the measured and predicted power contours of 10 W Cree device operating at 1GHz and class B biasing condition for three input power levels ($A_{11} = 18.3$ dBm, $A_{11} = 13.3$ dBm, $A_{11} = 4$ dBm)

The good agreement between measured and targeted impedances for the three power levels, wherein the NMSE is about -30 dB, can be clearly seen. Figure 5.14 shows the comparison between measured and predicted P_{out} for the same input power levels in Figure 5.13.

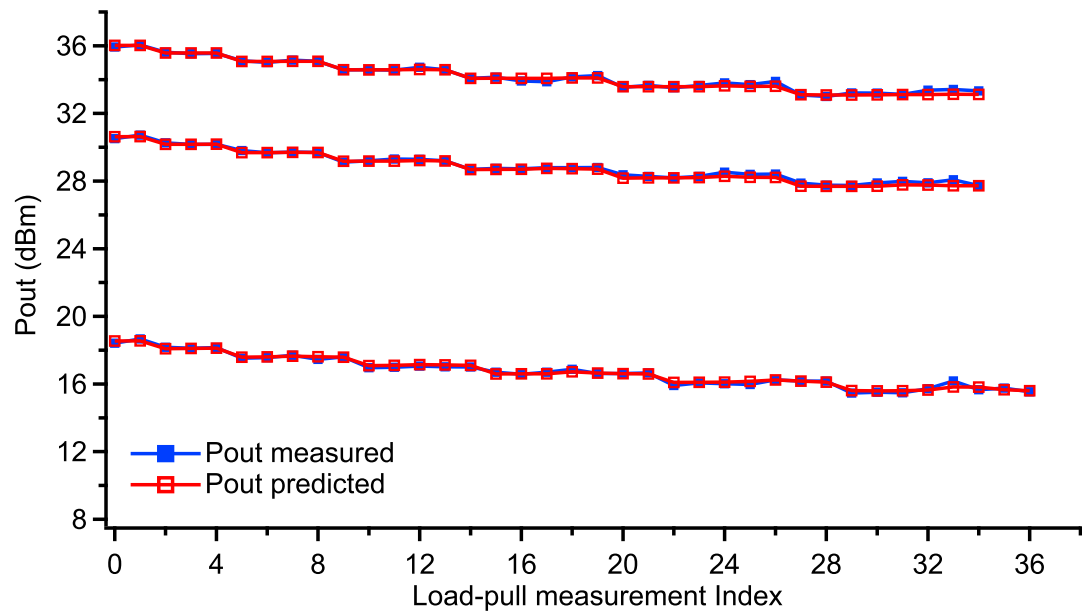


Figure 5.14: Comparison between the measured and predicted P_{out} of 10 W Cree device operating at 1 GHz and class B biasing condition for three input power levels $A_{11} = 18.3dBm$, $A_{11} = 13.3dBm$, $A_{11} = 4dBm$

This result shows an excellent agreement between measured and predicted output power within the second iteration when a 7th order load-based model was used. This agreement is an indication that this is a reliable dataset for generating the a-wave based model that is compatible with the CAD tool environment. It has been observed that the 7th order a-wave based model was required to achieve a model

accuracy within NMSE equal to -45 dB. This approach yields a 7th order a-based model with a different set of coefficients over the power range.

Figure 5.15 shows a comparison between measured P_{out} and the prediction of the a-wave based Cardiff behavioural model.

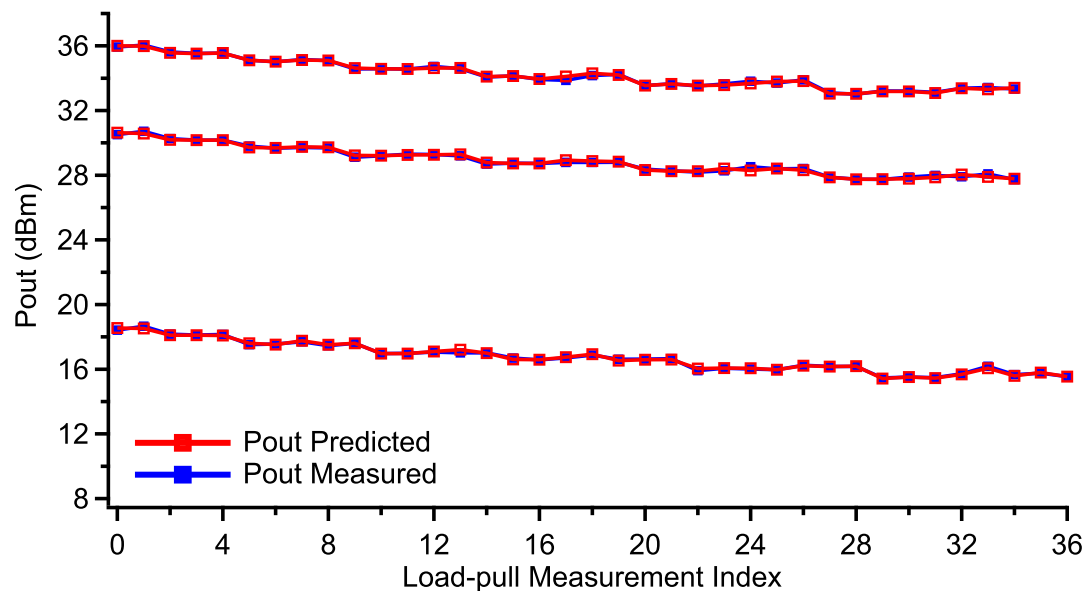


Figure 5.15: Comparison between the measured and predicted P_{out} using 7th order a-wave based model for 10 W Cree device operating at 1 GHz and class B biasing condition for three input power levels $A_{11} = 18.3dBm$, $A_{11} = 13.3dBm$, $A_{11} = 4dBm$).

Table 5.3 summarises the result of the three selected load-pull examples shown in Figure 5.13, 5.14, and 5.15. Similar results have been achieved at other power levels, which are omitted here for the sake of brevity.

Table 5.3: Summary of multi-power level load-pull measurement.

Power level Index	No. Measur.		Actual measurement			A-wave based model prediction		
	1 st	2 nd	Model Order	NMSE	Max Pout	Model Order	NMSE	Max Pout
	1	36	36	7 th	-36.5	0.28	7 th	-45
2	36	36	7 th	-36.5	0.34	7 th	-44.2	0.23
3	36	36	7 th	-36.44	0.35	7 th	-46.4	0.18

5.6 LINEAR INTERPOLATION OF THE MODEL'S COEFFICIENTS

A robust and reliable global behavioural model within a single operating frequency and bias point would require a dense of measurements over a wide range of input drive power levels. Such requirement would cost a lot of time and efforts, since every single change within the input drive power level (a_{11}) requires set of load-pull measurements. For instance, the generation of a global model for an input power range (4.1 to 18.1 dBm) and density grid of 0.01 dB would require 1401 input power levels. This would lead to the requirement of performing $72 \times 1401 = 100,872$ measurements, since each input power level requires at least 72 measurements to define its optimum space according to the strategy that was mentioned in section 5.5. Such large number of measurements is not acceptable from different aspects, like the system utilization and time taken as well as the manpower requirement. This

problem requires a solution that makes the modelling process for a device easier, simpler and efficient.

A mathematical frame work that can be used for such kind of modelling has been mention in [6], where an advance formulation of the Cardiff behavioural model has been mentioned. This formulation allowed for the a-wave model generation of a very small power range that includes only three power levels with a power step of 1dB. The general formulation that presented has not been tested for a large power range which leaves the door opened toward thinking about an alternative solution.

A simple linear interpolation among the coefficients of the extracted a-wave Cardiff behavioural model can solve the previous limitation. This was achieved by perform the linear interpolation among the extracted coefficients of multi-power levels. Due to the difficulty of the interpolate between the complex number of the extracted coefficients, linear interpolation was performed among the real and imaginary parts where their behaviour along the input power levels is applicable for such kind of interpolation process. Figure 5.16 and Figure 5.17 shows the real and the imaginary parts of the interpolated data of 14

coefficients for 8 power level ranges from 4.1 dBm to 18.1 dBm, while 2 dB power step was used to generate the interpolation data.

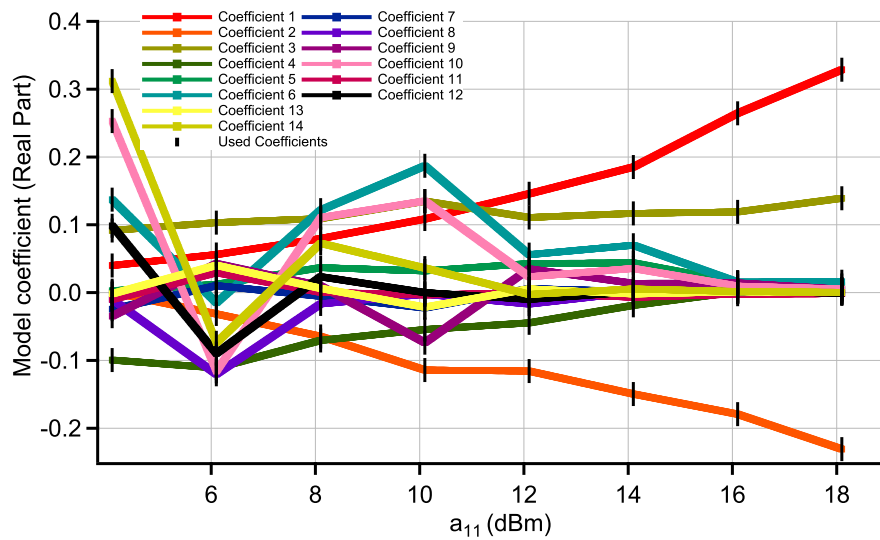


Figure 5.16: The real part of the 7th order extracted model coefficients for multi input power levels range from 4.1 dBm to 18.1 dBm with power space 0.01dB

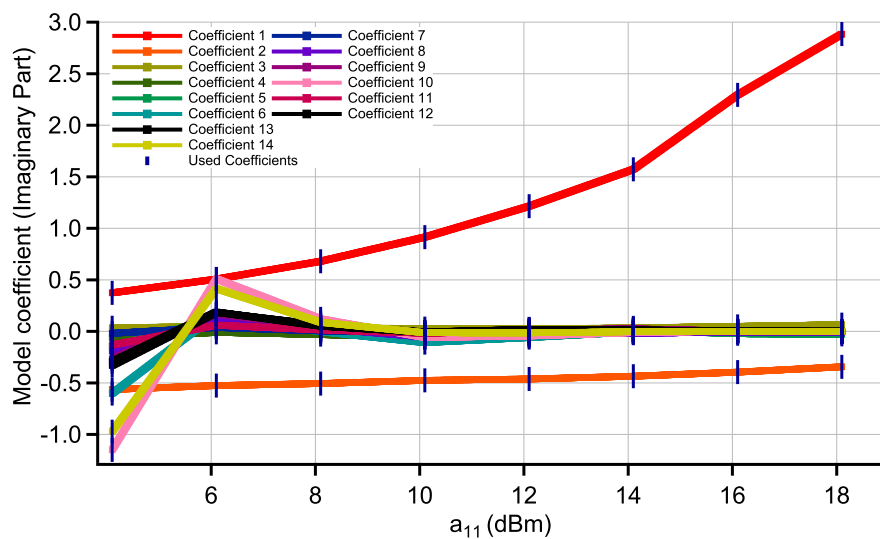


Figure 5.17: The Imaginary part of the 7th order extracted model coefficients for multi input power levels range from 4.1 dBm to 18.1 dBm with power space 0.01 dB

The presented method was tested by using the interpolated coefficients for predicting the b_{21} of an input drive power levels a_{11} that weren't involved within the interpolation process. The results over three different power levels illustrated in Table 5.4 show a very good agreement between the loads that been predicted by using the interpolated data and the loads that been predicted by using the exact extracted coefficients.

Table 5.4: Comparison between using interpolated and the exact coefficient for predicting loads

A11 (dBm)	NMSE (dB)
5.1	-39.7
15.1	-28.3
17.1	-42.1

Figure 5.18 shows the worst case of the above-mentioned results where the comparison between predicted loads using the exact coefficient and the interpolated coefficient is illustrated.

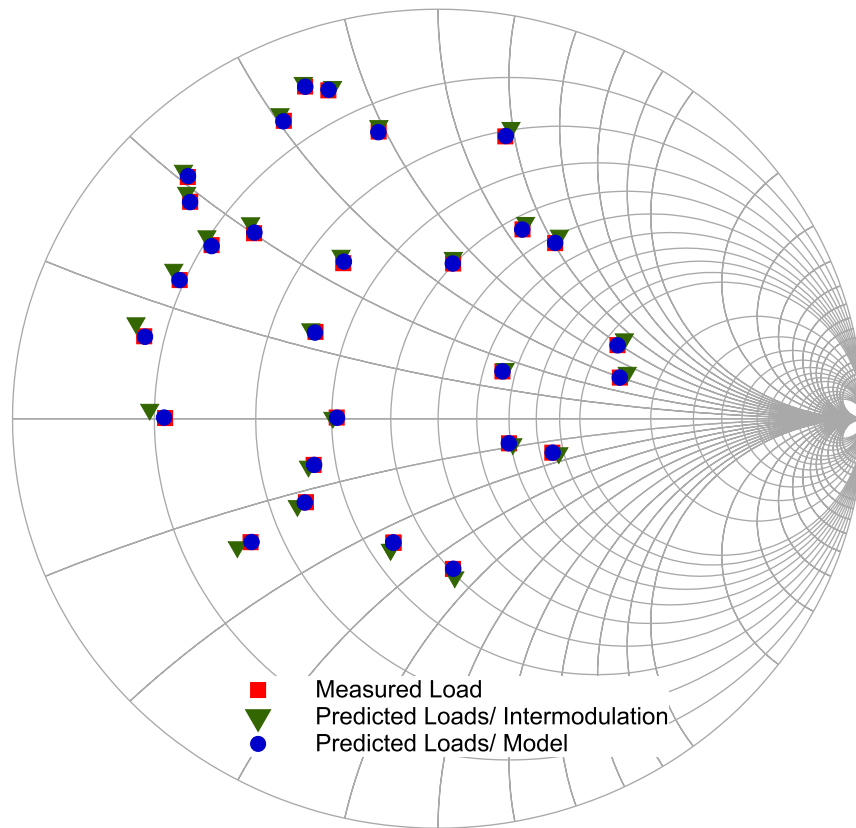


Figure 5.18: Comparison between loads predicted by the exact extracted model coefficients and loads predicted by using the model coefficient that been extracted using the interpolation method. Power level=15.1 dBm, NMSE=-28.3 dB

5.7 CHAPTER SUMMARY

This chapter has discussed an advanced and automated approach to address the challenge of identifying, in a time efficient manner, the appropriate load-pull impedance space for RF device performance evaluation. It also ensures that an accurate CAD behavioural model extraction is obtained. The novel features of emerging high-speed load-pull systems not only allows for more measurement data but also introduces new capabilities that are highly relevant in RF device modelling and RFPA design. The novel approach taken provides optimal datasets by selecting load impedances that target the direct measurement of load-pull contours, which are essential design information. The complete process was achieved by performing around 183 load-pull measurements, which includes the measurement for defining the optimum impedance and three load-pull iterations. The iterations were required to obtain the best agreement between the predicted and measured data. Within these iterations, the order of the load-based model has been increased from 3rd to 7th, wherein the latter been found to be the best for prediction because the difference between P_{out} predicted and P_{out} measured is within the tolerance of 0.5 dB. It is worth mentioning here that the whole process takes about 10 seconds.

This method was extended to also include efficiency contours. The method development allowed the load-pull measurement system to directly target efficiency and power contours in one measurement cycle. This combined approach minimised the number of load-pull measurements, hence the time required to define the optimum design space over which the desired efficiency and power contour variations are covered. It has been observed that four iterations were required to achieve the best agreement while the order of the load-based model that is necessary is increased to the 9th order. The required increment is due to the sensitivity of the efficiency with the achieved load. For example, the slight difference between load target and measured load would be reflected in a large difference between the predicted and measured efficiencies, thus one more iteration was required to achieve a good agreement. In conclusion, the number of measurements required to address the optimum design space in which efficiency and power contours are covered is 286 measurements and the time required is only about 12 seconds.

Further development of this approach has been achieved by targeting load-pull power contours at different drive power levels within one measurement session. While stepping from drive power levels during the load-pull measurement process, measurement speed was improved

by using b_{21} -scaling, which has been measured during the initial 50 power sweep. The load-pull measurement that is based on this scaling has been considered to be an initial measurement. This is followed by the second iteration, in which the load-based Cardiff behavioural model extracted at each drive power level is used. It is found that the agreement between measured and predicted P_{out} within the second iteration is less than 0.5 dB. Apart from the first power level, which requires about 286 measurements to define the desired (in this case up to -3 dB) power contours, each subsequent power level requires only around 72 measurements to define the power contours. According to the example that has been used in this chapter, defining the power contours of 15 different input power levels would require $(183 + 72 \times 14 = 1191)$ measurements), which can be performed within 1 minute, including the plotting and the a-wave model extraction.

The dataset allowed for both the accurate extraction and verification of a-wave based Cardiff behavioural models. The ability of this CAD compatible model to accurately predict the load-pull contours within the desired (-3 dB) load-pull power contour design space was directly verified by comparing the measured P_{out} with the predicted one. It has been found that the 7th order model would be sufficient to achieve

good agreement between measured and predicted P_{out} with less than 0.2 dB.

Additionally, In order to mitigate the number of the input power levels that are required to generate a global model, the linear interpolation method was applied on the extracted coefficients. This has allowed the extracted models of only 8 power levels to generate interpolated coefficients that can predict the device response b_{21} of any input power level locates within the range.

REFERENCES

- [1] S. C. Cripps, *RF Power Amplifiers for Wireless Communications*, 2nd ed. Norwood, MA: Artech House, 2006.
- [2] S. Woodington, R. Saini, D. Williams, J. Lees, J. Benedikt, and P. J. Tasker, "Behavioral model analysis of active harmonic load-pull measurements," in *IEEE MTT-S International Microwave Symposium*, May 2010, pp. 1688–1691.
- [3] J. J. Bell, R. Saini, S. Woodington, J. Lees, J. Benedikt, S. Cripps, and P. J. Tasker, "Behavioral model analysis using simultaneous active fundamental load-pull and harmonic source-pull measurements at x-band," in *IEEE MTT-S International Microwave Symposium Digest*, June 2011, pp. 1–4.
- [4] J. J. W. Bell, R. Saini, J. Lees, J. Benedikt, S. Cripps, and P. J. Tasker, "X-band behavioral model analysis using an active harmonic source-pull and load-pull measurement system," in *Asia-Pacific Microwave Conference*, Dec. 2011, pp. 1430–1433.
- [5] S. Woodington, T. Williams, H. Qi, D. Williams, L. Pattison, A. Patterson, J. Lees, J. Benedikt, and P. J. Tasker, "A novel measurement based method enabling rapid extraction of a rf waveform look-up table based behavioral model," in *IEEE MTT-S International Microwave Symposium Digest*, June 2008, pp. 1453–1456.
- [6] M. R. Moure, M. Casbon, M. Fernández-Barciela, and P. J. Tasker, "Direct extraction of an admittance domain behavioral model from large-signal load-pull measurements," in *IEEE MTT-S International Microwave Symposium*, June 2017, pp. 1057–1060.

CHAPTER 6

CONCLUSION AND FUTURE WORK

6.1 CONCLUSION

THE research in this thesis has successfully achieved its objectives. In particular, this thesis has presented a high-speed load-pull measurement system that maintains accuracy and high dynamic range. In addition, an intelligent search algorithm to define the optimum impedance and the appropriate design space over multipower levels has been presented. This work has also highlighted the importance and the utility of using the behavioural model and its applications to intelligently drive the load-pull measurement system. This conclusion will next briefly summarise the main results of each chapter.

The literature review in Chapter 2 has summarised the evolution of microwave measurements and the strict requirement of moving from

linear to nonlinear measurement. It has discussed the purpose of nonlinear measurements and the important instruments that are used, in addition to the important research done in this area. This review also includes the evolution of load-pull measurement techniques in terms of their strengths and weaknesses, as well as the instruments and strategies that have been used. Important trends towards accurate and fast load-pull measurement has also been considered in the literature review.

The in-depth review of the employed load-pull measurement techniques and strategies in addition to the exploited systems that perform this kind of measurements shows that there is a crucial need to develop a new system and strategies. This is a result of the weaknesses that are encountered by the load-pull measurement system, such as the measurement speed, the iteration process, the system utilization, and the rigidness of the existing systems, where there is a difficulty to add or amend functionalities. Therefore, this thesis has focused on these two areas, developing a new measurement system that can potentially perform hundreds of large-signal measurements within a practical time. This thesis has also employed new strategies that can perform the active load-pull measurement, where user interac-

tion, system utilization and the number of iterations are kept to a minimum.

Based on this realisation, Chapter 3 presented a new modular measurement system architecture based on NI PXIe modules. This system has the potential to perform 200 measurement/sec for the fundamental power sweep when 10 k samples per average are used, which increases to about 700 measurement/sec when 100 samples per average are used. With regard to the dynamic range, six harmonics of the 10W Cree device were measured by the this system. This has shown the ability of the presented system to reach up to 100 dB with a noise floor at about -136 dBm/Hz.

In Chapter 4, the load-based Cardiff behavioural model and the high-speed measurement system have been used together to derive a fully-automated fundamental active load-pull measurement process. This measurement involves sequential systematic steps, which have been designed to define the optimum impedance required for high efficiency or high output power automatically with minimum user interaction and iterations. The only requirement from the user is to assign a valid power sweep range to begin the measurement. The load-based Cardiff behavioural model has been used to predict the desired injected

signal to emulate a load target. The results shows that 8 seconds are sufficient to automatically identify the optimum impedance for six power levels. Automatically hopping over the power level while performing load-pull measurements has been achieved by using b_{21} scales, which are measured during the 50Ω power sweep. In addition, the nonlinear measurements have been extended to include load-pull at harmonic frequencies. The results show that the mix load-based Cardiff behavioural model is able to successfully predict the required injected signal to emulate a 2F0 load target located at $|\Gamma_{22}| = 0.7$ from the first iteration within an NMSE = -22 dB. The mixed model generation required for the second harmonic load-pull requires an initial measurement.

Furthermore, a simple look-up table and descriptive function to model the nonlinear RF test-set path were investigated. The models have been experimentally validated under large-signal excitations and their performance has been compared. Both methods have shown a very good agreement between measured and targeted powers, and the average magnitude residual difference for the same number of measurements is 0.1 dB. It has been found that 14 measurements are enough to generate sufficiently accurate models with an average NMSE error at approx. -23 dB. The investigation clearly demonstrated that

increasing the complexity of the nonlinear models offers little to no benefit and suggests a straight-forward method for the further improvement of an open-loop active load pull system.

The presented approaches have shown great success in terms of load-pull measurement system utilisation and speed. In addition, the strategy that has been presented provides an efficient way to define the optimum impedance without risking the device. The potential of the Cardiff behavioural model to drive the load-pull measurement system effectively has been shown in several different aspects.

The third main objective of this thesis has been successfully achieved in Chapter 5. This chapter discussed a novel strategy to address the challenge of identifying, in a time efficient manner, the appropriate load-pull impedance space for RF device performance evaluation and extracting an accurate behavioural model. The novel approach taken here provides optimal datasets by selecting load impedances that target the direct measurement of the efficiency and power load-pull contours, which is essential design information. This strategy has mitigated the number of the load-pull measurements required to define accurate load-pull contours. It also permits a direct extraction and verification of the behavioural model. Moreover, this approach

has been applied to drive the load-pull measurement over several power levels. Two to three measurement iterations were required to accurately define the -3 dB load-pull power contours of a single power level during the automated process. The examples that were given show that the total number of measurements required to define the desired power contours for 15 power levels is 1191 measurements, within about 1 minute. This was done in one measurement session and the behavioural model is extracted simultaneously. Furthermore, a simple linear interpolation between the extracted coefficients of the behavioural model was utilized in this chapter to mitigate the required number of measurements. This has significantly reduced the required number, for example measurements of only 8 power levels can be utilized to predict accurately the DUT's response (b_{21}) of any power level within the range and to a resolution of 0.01 dB.

6.2 FUTURE WORK

The flexible nature of the measurement system developed and the load-pull strategy allows for many opportunities for future work. In Chapter 3, the system that was presented has allowed for about 200 measurements/sec. This achievement is based on the first software programming trail. However, this can be modified by using a better programming approach, such as the utilisation of built-in FPGA that permits for high speed data processing. It is also possible to exploit the behavioural model to maximise the load-pull measurement speed. This can be achieved by using a behavioural model based on dynamic samples per average. The number of samples can be set according to the predicted output power: for a high predicted power, a low number of samples per average can be used; and for a low predicted power, a high number of samples per average can be used. This approach may be able to significantly reduce the number of samples within one measurement and, hence, will increase the measurement speed. Moreover, the availability of high dynamic range and the noise floor measurement would suggest the potential application of the presented system for noise type characterisations. For instance, allow for characterizing the noise figure of the DUT under different load conditions.

Furthermore, thanks to the flexibility and the expandability of the presented system in term of software and the hardware, in addition to the available characteristics of the of the VSA/VSG within the presented measurement system, such as the sampling rate of the AWG (400 MS/s) and the bandwidth of the ADC (50 MHz), would allow the system to be developed further, such as an implementation of the pulse mode, 2-tone, multi-tone, and modulated signal and a load-pull to be performed on each of these measurement types.

The presented measurement system only covers the fundamental and the second harmonic load-pull based on Cardiff behavioural model. However, due to the importance of the 3rd harmonic load-pull measurement to achieve high efficiency, it would be possible to extend the load-pull measurement to cover three harmonic load-pulls.

Furthermore, because generating an accurate model for circuit simulation directly from measurements has recently received significant interest, automated the CAD behavioural model generation can be significantly improved by automating the load-pull measurement—not only for multi-power levels but also to cover different conditions (e.g. frequency and biasing points). Such strategy together with the coefficients interpolation approach that has been presented in Chapter

5 would allow for the rapid, direct and simple extraction of a global device model from measurements while using a verified small number of measurements.

APPENDIX A

GENERAL DESCRIPTION OF THE SYSTEM'S HARDWARE

The presented system is a combination of the two PXI chassis that contains VSGs and VSAs in conjunction with other external hardware shown in Figure A.1.

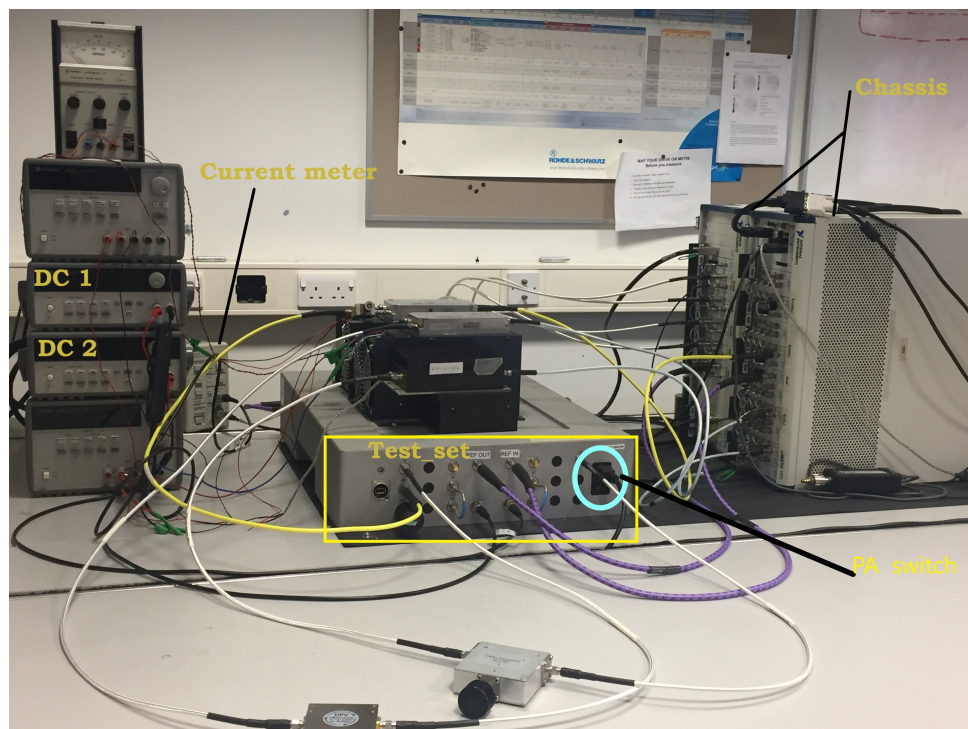
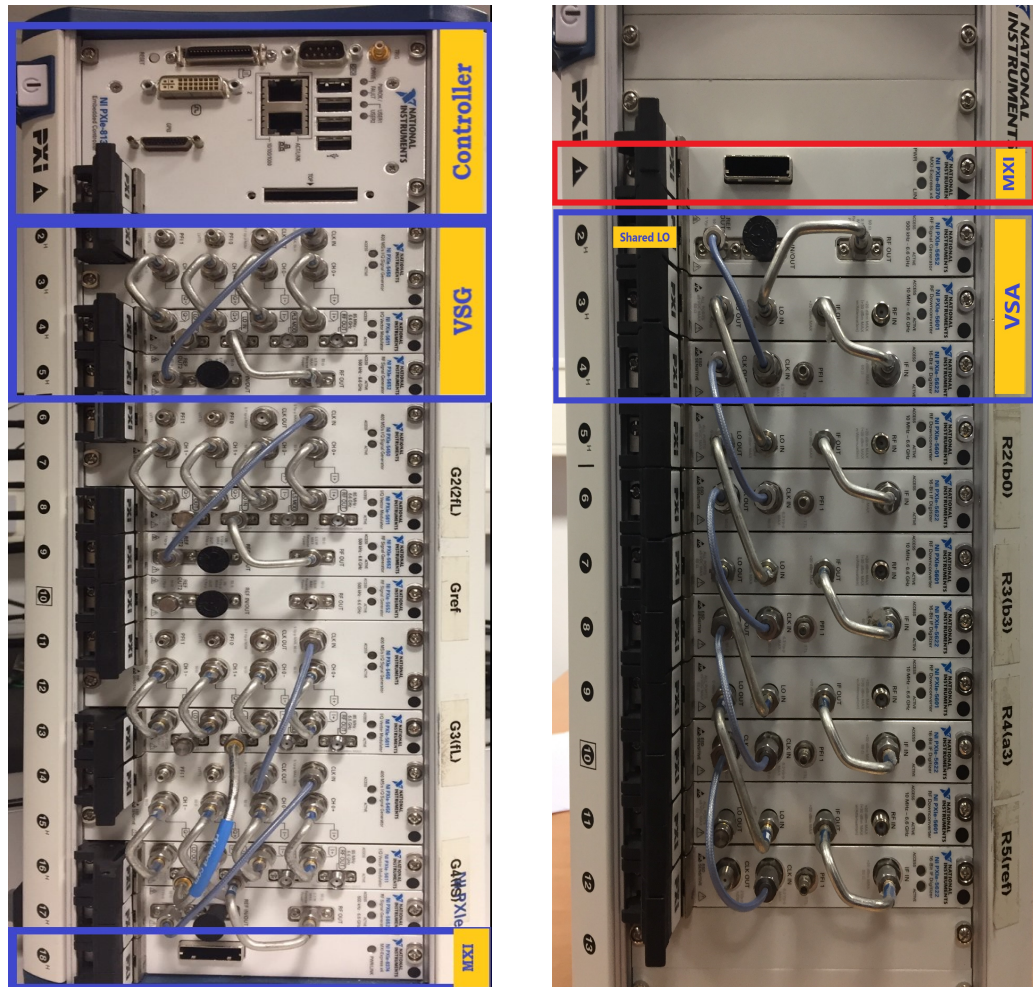


Figure A.1: Picture of the actual measurement system.



(a) Generators chassis

(b) Receiver chassis

Figure A.2: Picture of the Actual chassis

The generator chassis contains the VSGs- one for the source side, one for each of three harmonics on the load side, one for supplying the input to the phase reference standard. Also, it included Embedded controller and the MXI link card, which connects to the receiver chassis. The receiver chassis involves 5 VSAs, the MXI link card - connects to the generator chassis, and two Digitiser cards -one is

used to read from the current probe. The other part of the hardware is the test-set box as shown in Figure A.1. This box contains the PA of the phase reference standard, which provides harmonics with known phases, to allow for waveform reconstruction. Also, it contains the directional couplers to separate the incident and reflected waves at each of the device ports. Other hardware part that are shown in Figure A.1 are Agilent DC supplies, which supplies for biasing devices and the Tektronix current probe that is used to measure current.

To start using this system, the following instructions have to be followed

1. Turn on the PA DC supplier shown in Figure A.1.
2. Turn on VGS and VDS DC supplier shown in Figure A.1.
3. Turn on the DC current meter.
4. Turn on the PA of the phase reference standard as shown in Figure A.1.
5. Turn on first the VSAs chassis and then the VSGs chassis.

GENERAL DESCRIPTION OF THE MEASUREMENT SYSTEM'S SOFTWARE

In order to run the software of the presented measurement system, the LabVIEW project must be run first and then run EDITED Loadpull GUI.vi from the Master UI folder as shown in Figure A.3.

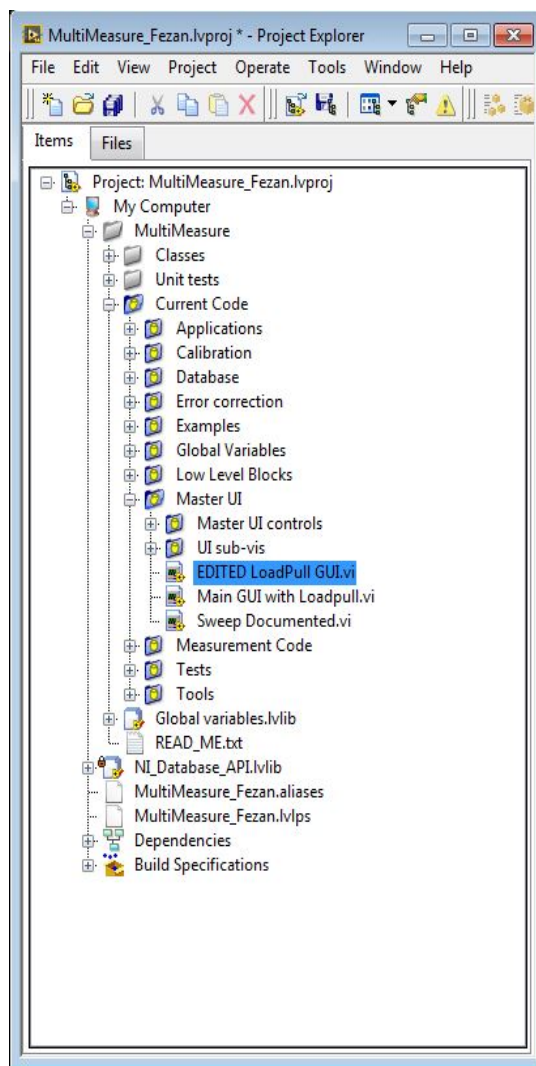


Figure A.3: The main measurement system's project navigator.

The EDITED Loadpull GUI.vi shows the main GUI (Graphical user interface) of the software that can be used to navigate for different parts of the software such as the calibration manger, load-pull parts, and the DC control unit as shown in Figure A.4.

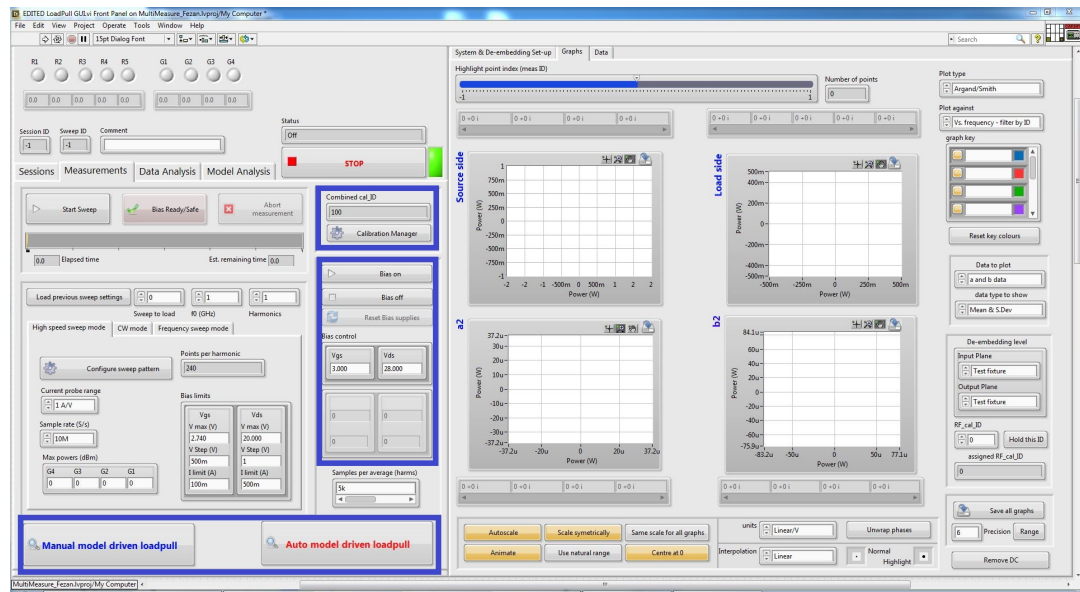


Figure A.4: The main GUI of the measurement software

The calibration manger shown in Figure A.6 would take the user to the four calibration types; the RF calibration Figure A.7, the receiver's calibration Figure A.7, and the generator calibration Figure A.8.

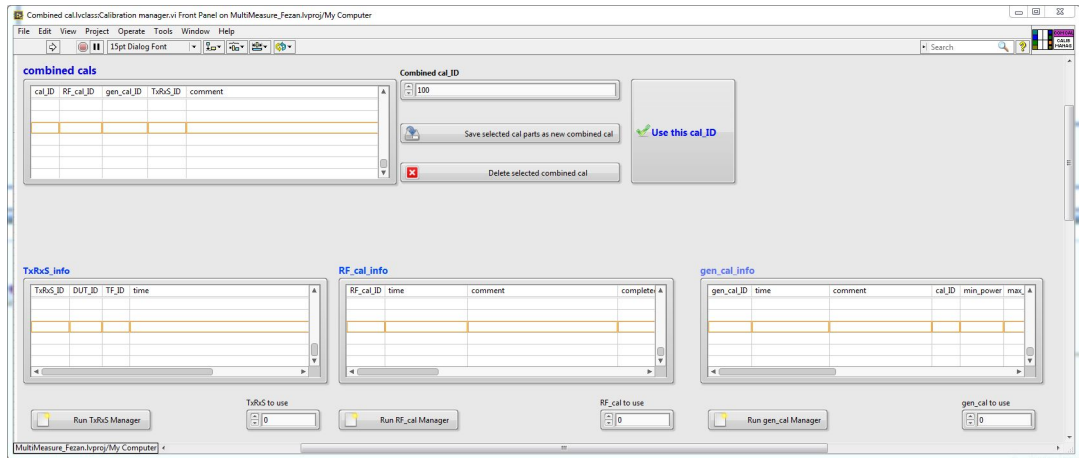


Figure A.5: The calibration manger GUI

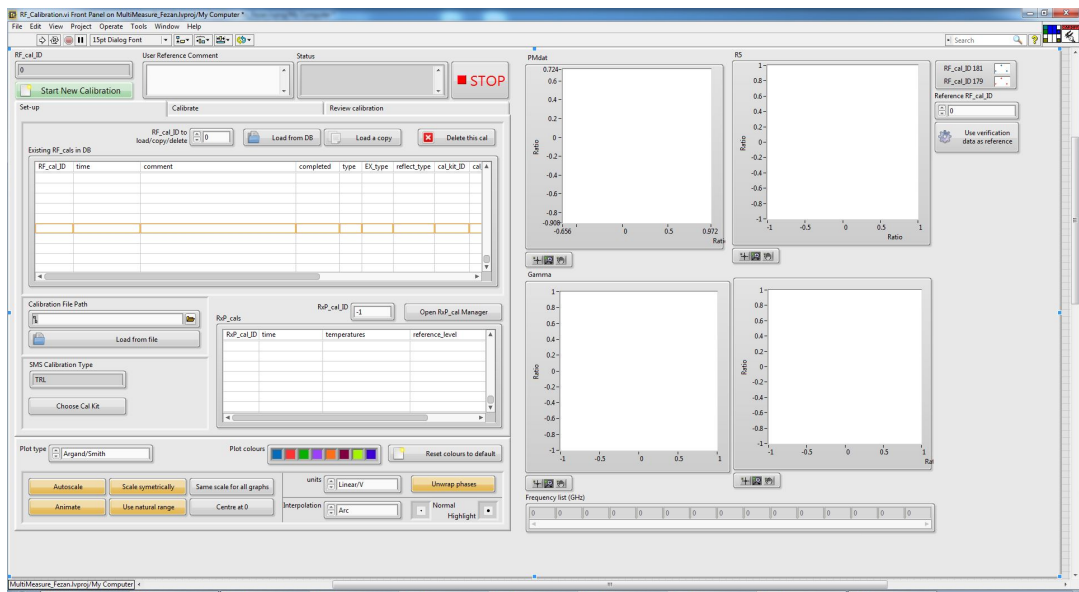


Figure A.6: The calibration GUI

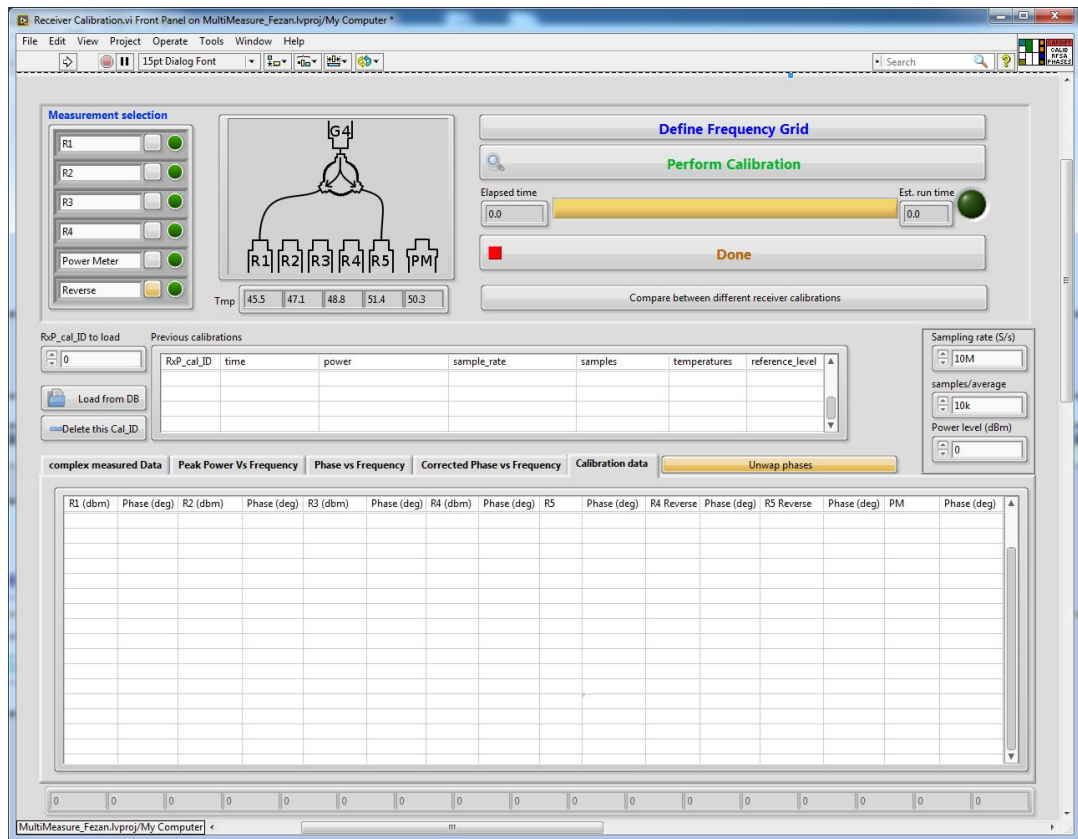


Figure A.7: The GUI of the receiver calibration

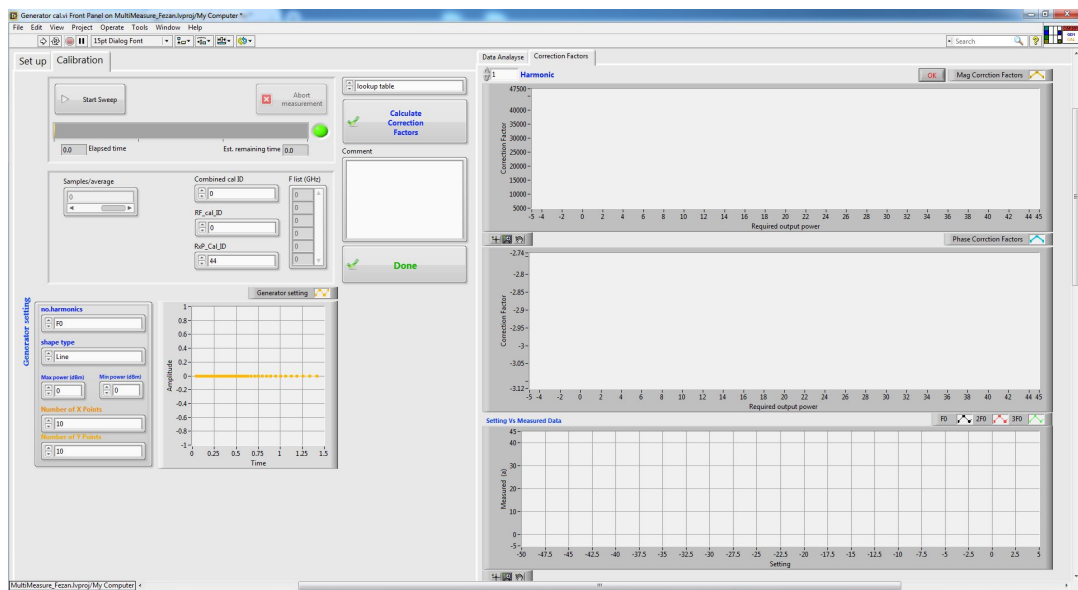


Figure A.8: The GUI of the generator calibration

MODEL DRIVEN LOAD-PULL SOFTWARE

Login to the model driven load-pull can be achieved by pressing on either the manual model driven load-pull or the auto model driven load-pull that have been shown in Figure A.4. The model driven load-pull GUI has several taps, all of them work for automating the load-pull measurements. For example, the first tap is used to define the main factors of the load-pull measurements such as operating frequency, combined calibration ID, sampling rate and the tracking factor.

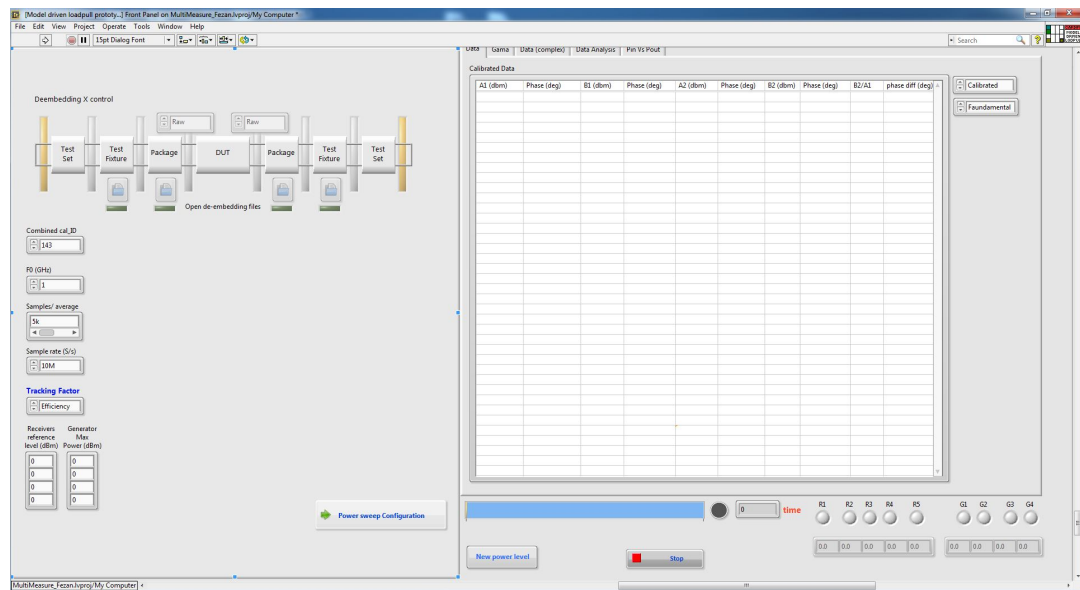


Figure A.9: The first tap of the load-pull measurement GUI

By the second tap shown in Figure A.10 the power sweep range that can be performed on the DUT can be defined. Also, a generator that wanted to be used for the measurement can be defined by this tap .

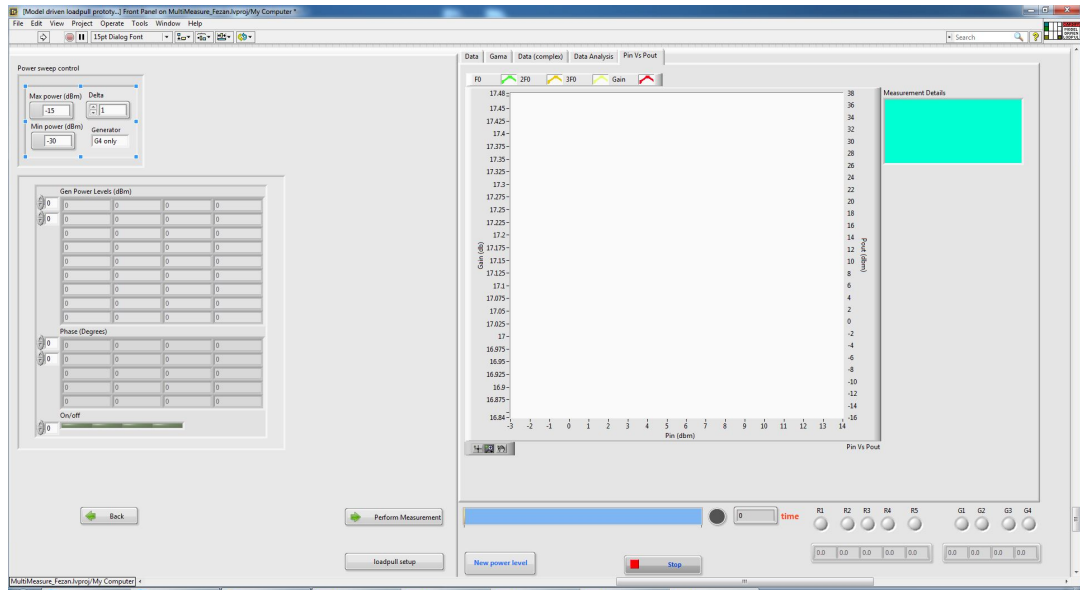


Figure A.10: Power sweep setting tap

The following step shown in Figure A.11 is defining the operating condition of the initial load-pull measurements such as the impedances grid shape and the range of the a_{21} .

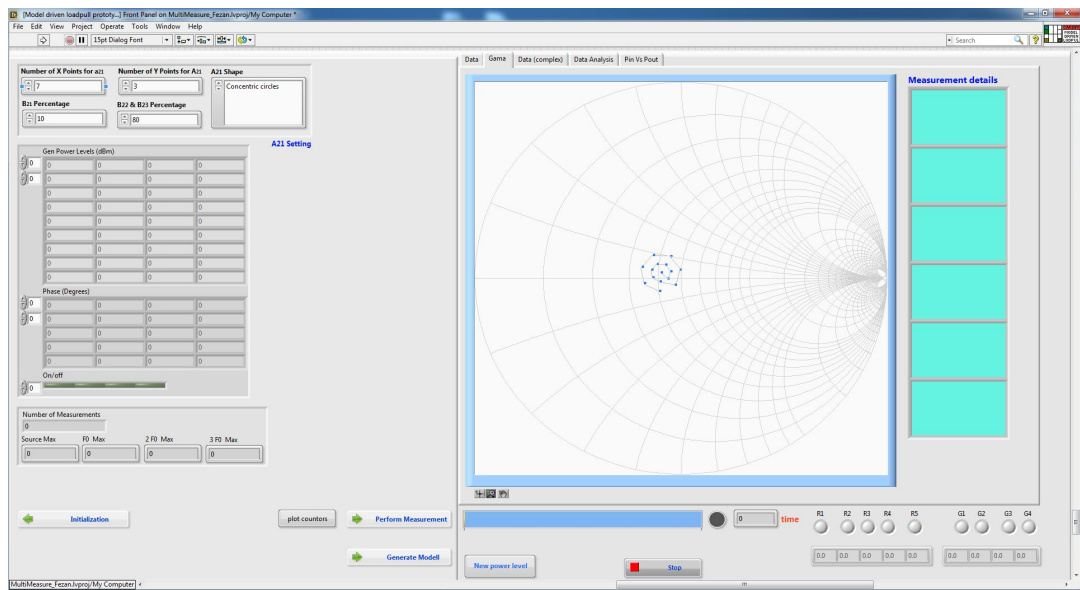


Figure A.11: The initial load-pull measurement setting tap

In order to generate the model using the measured data, the generated model button shown in Figure A.11 has to be pressed after the initial measurement is performed. This will allow the model's exponent matrix generator window to show up as shown in Figure A.12. Choosing the required exponents is followed by the model verification tap shown in Figure A.13 where the quality of the generated model is quantified by calculating the NMSE between b_{21} predicted and b_{21} measured. In case different set of exponents is required the regenerate model button can be pressed.

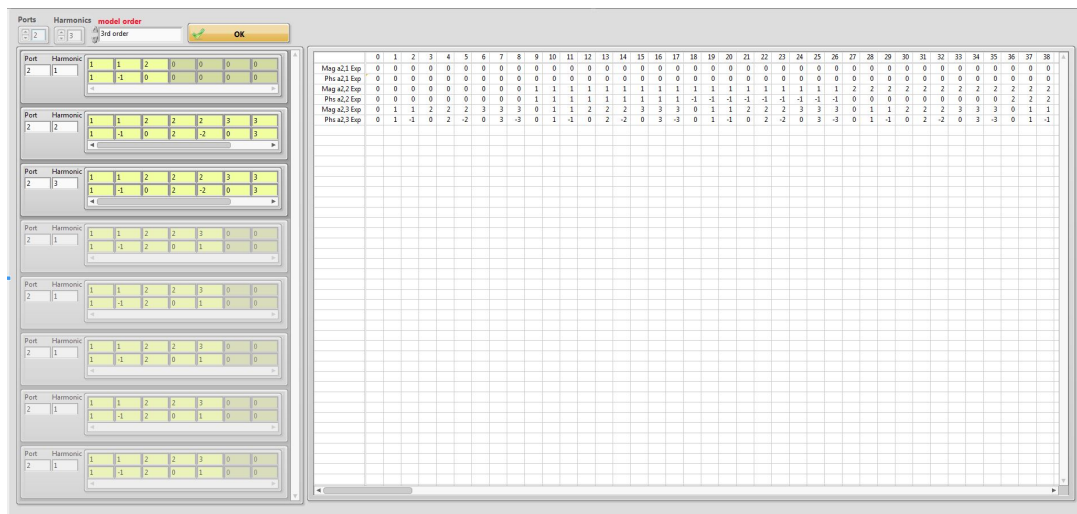


Figure A.12: Model's exponent matrix generator

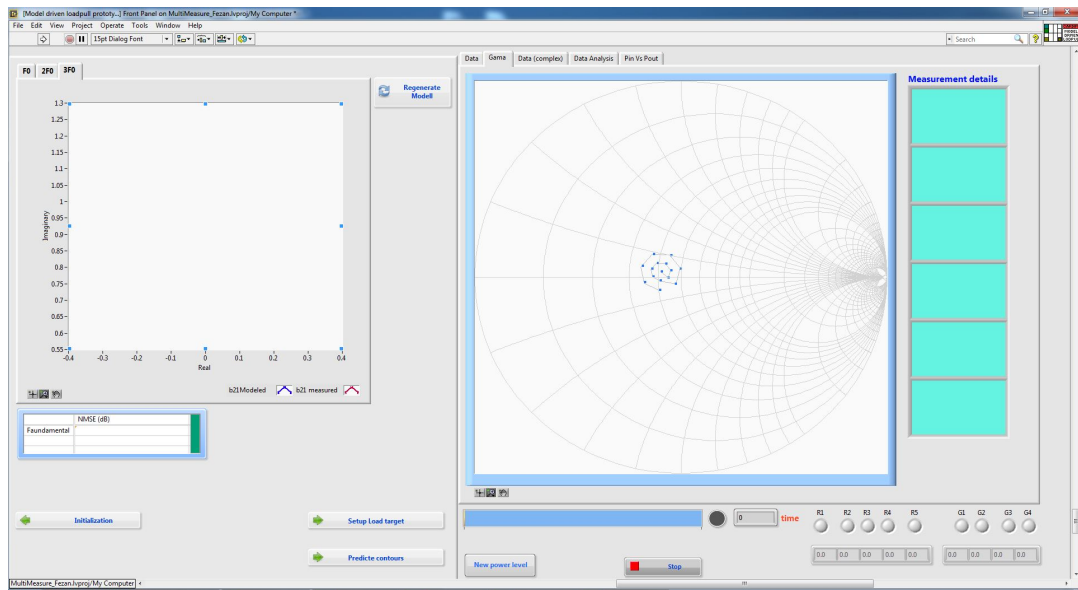


Figure A.13: The model verification tap

After the load-based behavioural model is generated, the load targets for the next load-pull measurement can be set by using the tap shown in Figure A.14 which is shown up by pressing the button " setup load target" shown in Figure A.13. This tap has several option to set the load targets either for the fundamental only or fundamental and harmonics.

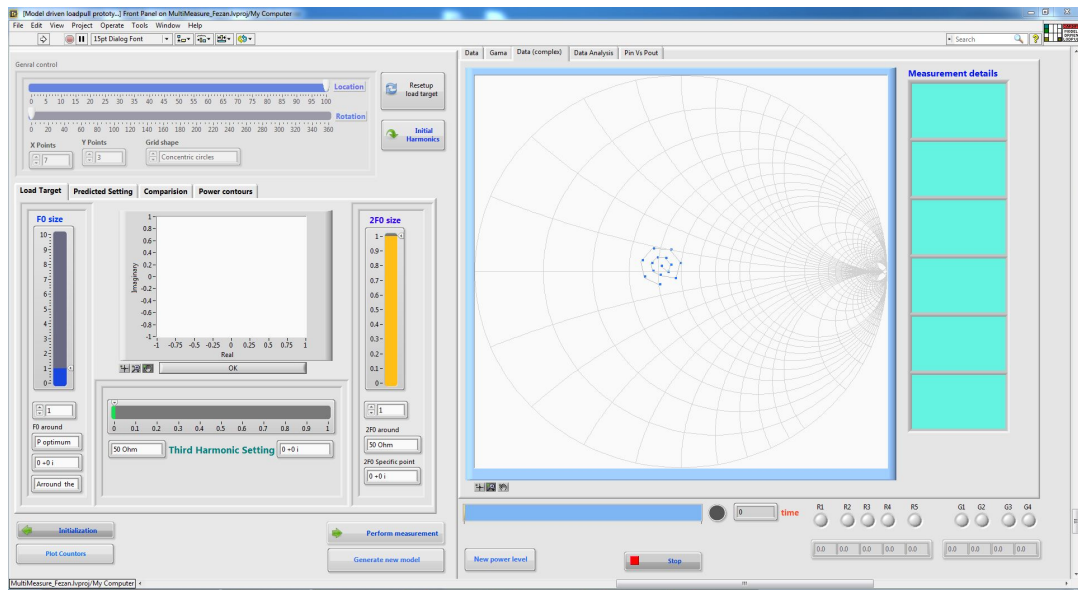


Figure A.14: *Harmonic load-pull targets set-up*

In case the user's preference is to predict the location of the contours and target them directly, the "predict contours" button shown in Figure A.13 has to be pressed, which shows up the tap shown in Figure A.15.

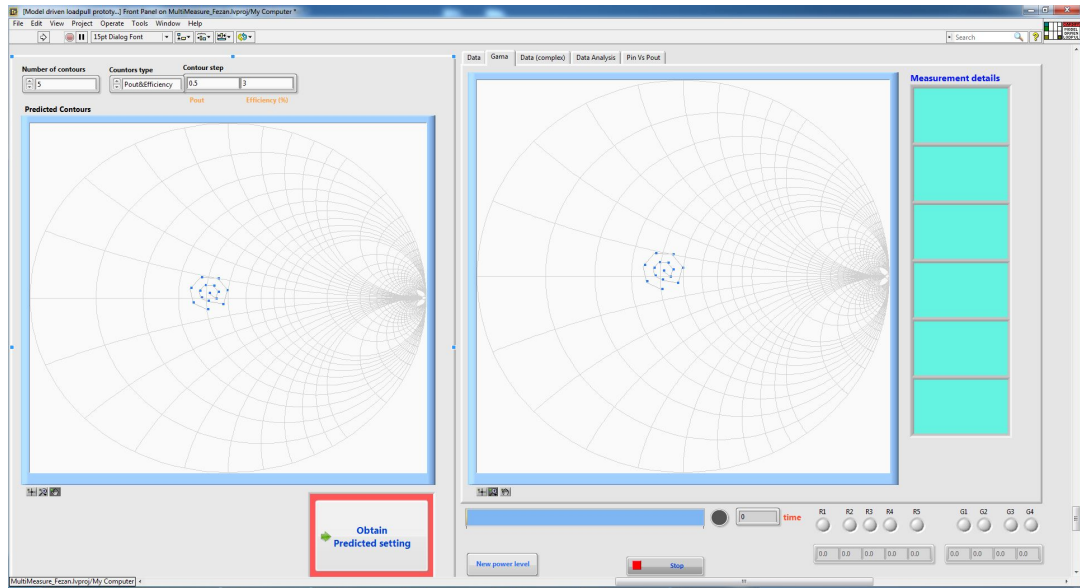


Figure A.15: *Contours prediction tap*

This tap would allow the user to choose whether the prediction is only for the Pout or Pout and efficiency together. Also, the user here can define up to which compression region the prediction is performed?

APPENDIX B

This appendix would show the two published paper that were presented in ARFTG 2018 and the International Microwave Symposium (IMS 2018) as well as the joint paper which is accepted by the 2019 Radio and Wireless Week Conference (RWW).

On the Effective Modeling of the Test-Set Non-linearity

Thoalfukar Hussein^{*}, Azam Al-Rawachy[‡], Syed S. Anera[†], James Bell[†], Paul Tasker[†], Johannes Benedikt[†]

^{*}Technical Institute of Karbala, Al-Furat Al-Awsat Technical University, Karbala, Iraq

[†]School of Engineering, Cardiff University, Cardiff, UK, CF24 3AA

[‡]Engineering Department, Mosul University, Mosul, Iraq

Email : Husseinith@Cardiff.ac.uk

Abstract—This paper investigates and compares the use of nonlinear test-set models for an effective and accurate operation of active load-pull systems. The results demonstrate a simple-to-implement and yet robust technique to align the generator and receiver reference plane with a minimum set of required measurements. With only 14 measurements a high agreement between target and measured load points was achieved with an average error less than 0.1 dB over a 70dB dynamic range. An increase in modeling complexity has therefore yielded no improvement. To compare the results, a behavioral model was employed, and it is shown that a high order of model complexity is required to achieve the same level of accuracy. The presented work provides, for the first time, a practical and effective method for the modeling of test-set nonlinearities, hence allowing a cost-effective implementation of active load-pull systems that operate power amplifiers within a gain compression region.

Index Terms—Automated Active Load-pull, Behavioral model, Generator setting.

I. INTRODUCTION

Load-pull measurements are becoming more important in the design and modeling of power amplifier (PA) [1], however the traditional load-pull techniques have shown a shortage in the execution speed due to the number of iterations required to achieve a specific load target [2]. This time-consuming iteration must be minimized to speed up characterization process [3].

A key aspect is the accurate nonlinear modeling of the signaling path between the generator, which controls the injected a_2 signal. It allows for the use of load-pull amplifiers within their nonlinear regime to keep their required maximum output power at a minimum. This in turn reduces the overall costs of the nonlinear measurement system. It is an aspect of particular relevance for systems operating at high-frequencies where power amplifiers with sufficiently high output power are either not available or come with a high cost-premium.

Several types of strategies have been used to speed up the load-pull measurement and mitigate number of iterations. A typical approach is the use of look-up-tables to correct for the AM-to-AM and AM-to-PM non-linearities of the load-pull amplifiers. However, little has been reported in the literature on its implementation and the achieved accuracy improvements in setting targeted load-impedances within the first iteration. There are number of potential techniques, albeit often more complex in nature, that might be employed to further improve the load-pull performance. One of those approaches is the use of a behavioral model.

This paper investigates new methods to model the PA's nonlinearities. For this purpose, a look-up table (LUT) method

is developed which is based on gradients of AM-to-AM and AM-to-PM of the load-pull amplifier (LPA). In addition, the Cardiff model has been reformulated to account for the simplified loading conditions of the LPA and its performance is used as a reference. The investigation also seeks to identify the minimum number of measurements for both approaches that are required to achieve sufficient load-pull accuracy with the first iteration. The objective is to provide a guide for the implementation of new and cost-effective active load pull system.

II. LOAD-PULL MEASUREMENT SYSTEM

Fig. 1 shows the block diagram of the high-speed nonlinear measurement system that has been utilized to carry out the measurements in this paper. The new systems architecture based on high speed PXIe modules is conceptually similar to previously published systems that are based on a Vector Network Analyzer (VNA) [4]. Data acquisition is performed by vector signal analyzers (VSA). For the signal generation, vector signal generators (VSG) with magnitude and phase control are employed. These are used to provide the stimulus for the device under test (DUT) and the open-loop active load-pull at the fundamental and harmonic frequencies.

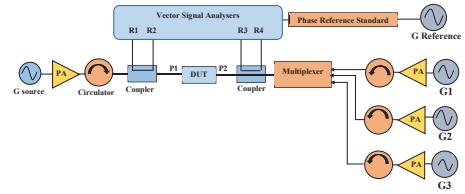


Fig. 1: Block diagram of the high-speed measurement system, which is realized PXIe instrumentation.

The open-loop active load-pull in this work is relying on a Cardiff load-based model to predict the required injected signals (1). It allows for the prediction of the DUT nonlinear response and obtain the correct a_2 signal for a targeted load impedance with a single iteration.

$$b_2 = \sum_{D=0}^{D=1} \sum_{C=-(M-D)}^{C=+(M-D+1)} K_{|C|+2D,C} |\Gamma_2|^{|C|+2D} \left(\frac{\Gamma_2}{|\Gamma_2|} \right)^C \quad (1)$$

This model structure is a variant of the Cardiff behavioral model. Here, the b_2 signal is a function of the load reflection coefficient Γ_2 . The user defined parameter, M , defines the model complexity, while $K_{p,q}$ are the extracted model coefficients.

The predicted signal a_2 computed by the Load-based model according to (1) does not take into consideration the effect of the passive and active components which fall between generator and the DUT, such as couplers, circulators, PA drivers and cables. This hinders in achieving load targets during the load-pull measurements, since the phase and magnitude of the injected signal a_2 are not completely accounted for.

In an effort to overcome this problem, different techniques have been used. In principle, there are two approaches. A numerical technique [5] allows to compensate any differences between the measured and target loads values through use of successive iterations and compensates for the nonlinear DUT and LPA responses. Relatively, simple methods such as Newton-Raphson algorithm provide here a robust and continuously improving approximation at the expense of a large number of iterations. To overcome these issue, a dedicated nonlinear model of the PA path can be employed. This allows for the load-pull amplifiers to operate into their non-linear regime while allowing for the accurate generation of the load impedances.

III. MEASUREMENT SETUP AND MODEL EXTRACTION

The measurement configuration required for extracting nonlinear LPA models is depicted in Fig. 1. This setup should involve all the hardware required for the load-pull measurement to ensure that every loss and amplification is included through the model computation. This measurement requires port 1 and port 2 to be terminated by 50 Ohm, as the termination eliminates unwanted signal reflections during the measurement of a-wave signal.

Fundamentally, the non-linear large-signal traveling wave response at the DUT output (a_2) of a PA during this measurement is mathematically related to the generated traveling wave stimulus a_{LP} that is provided the VSAs. The non-linearity of the generated signal is a consequence of the PAs behavior when driven at high power level. The extracted model coefficient must quantify the generic relationship; $a_2 = f(a_{LP})$. The load based-model equation that mentioned in the previous section, was specifically reformulated (2) in order to provide a simplified polynomial equation.

$$a_{LP} = \left(\frac{a_2}{|a_2|} \right) \sum_{n=0}^{n=\infty} K_{2n+1} |a_2|^{2n+1} \quad (2)$$

This equation provides a mathematical framework that can be used to characterize a signal path of the load-pull test-set to move the generator reference plane to the device reference plane. To have a full utilization of the power amplifier that is used within the measurement setup, the model has to be generated while the PA is

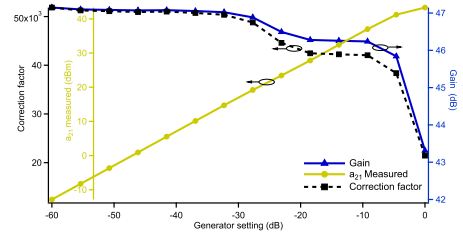


Fig. 2: Generator setting versus a_{21} -wave measured, gain and associated correction factors of the PA.

driven into the compression region as shown in Fig 2.

For the generation of the Cardiff model, an a_{LP} spiral is generated by the VSG and the a_2 response measured by the receivers (VSAs) within the measurement system. The generated spiral is shown in Fig. 3 and includes both magnitude and phase changes. The magnitude values span over the same dynamic range of the PA performance as shown in Fig. 2. This measurement is used to generate Cardiff models with an increasing complexity.

The error of the generated Cardiff model is estimated from the difference between the actual a_{LP} settings and the values predicted by the models. The overall error is estimated using the minimum normalized mean square error (NMSE) algorithm. Table I shows that sufficient accuracy can be achieved with a model complexity of 13^{th} or higher, i.e. $n=6$ in (2).

TABLE I: NMSE of different model complexity

Complexity	3^{rd}	5^{th}	7^{th}	9^{th}	11^{th}	13^{th}
n	1	2	3	4	5	6
Error (dB)	-25.1	-29.5	-34.7	-39.6	-44.34	-47

Fig. 3 shows the high agreement between the generator setting that has been used for the model generation and the generator setting when predicted by the generated model.

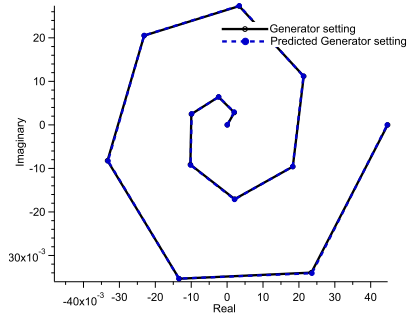


Fig. 3: 13^{th} order Model verification

The obtained Cardiff model coefficients can be saved in a database and re-used during the forthcoming measurements. This is particularly beneficial for the load-pull measurement because it can be applied directly during the measurement on the required powers a_2 and then converted for a suitable generator setting.

The second investigated LPA model utilized the same measurement data to generate a look-up table (LUT). As the absolute AM-to-AM and AM-to-PM values of the LPA exhibit a relatively strong variations, a large number of measurement points would be required to represent the nonlinear behavior of the amplifier. To keep the number of required measurements at a minimum the utilized LUT model is based on the gradient of the measured AM-to-AM and AM-to-PM curves. The table is comprised of the indexed a_2 measured and stored correction factors (CF) for magnitude and phase response of the LPA path where CFs are calculated according to (3).

$$CF = \frac{a_2}{a_{L,P}} \quad (3)$$

The calculated magnitude CFs shown in Fig. 2 (black trace) and clearly show a dependence on the gain of the LPA path. At the flat gain region the value of the CFs are relatively constant while it drops once the PA operate through the non-linear region, when its' gain is compressed accordingly.

The look-up table is used to transform the required a-wave at the DUT reference plane to its corresponding generator setting by applying the ratio calculated in (3). For example, if the a-wave at the device reference plane is a_2 its related correction factor will be looked-up from the stored look-up table. To apply the correction factor, eq. (3) will be rearranged and solved for $a_{L,P}$. The implementation utilizes nearest value interpolation, therefore, for power values between the indexed a_2 data points, the nearest power index is looked-up and the associated magnitude and phase CFs are used to compensate the loss and amplification through the signal path between the load-pull generator and the DUT reference plane.

To experimentally verify the two modeling approaches over a set generator settings, a direct comparison between the target and measured power points is illustrated in Figs. 4 and 5.

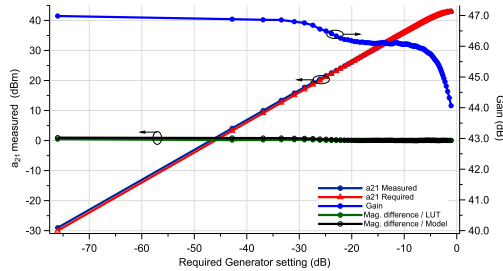


Fig. 4: Comparison between required and measured a_{21} at linear and compression region

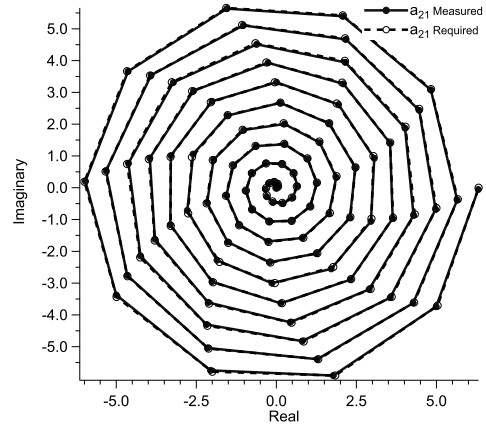


Fig. 5: Illustration of the agreement in phase and magnitude between required and measured a_{21}

Fig. 4 shows an excellent agreement is obtained for both type of models over a dynamic range of 75 dB including the 3dB compression region of the PA. Here, a 13th order Cardiff model and an LUT comprising 14 measurements are utilized, i.e. for the generation of the two models the same number of measurement was used. The average residual difference between target and measured powers is 0.1 dB for the Cardiff model. The residual difference that results when using the LUT, which has been obtained from the same power sweep. The average magnitude residual difference for the same number of measurements is slightly lower at approx. 0.06 dB.

This comparison has been expanded over a range of measurements that is used for the generation of both models. The results are shown in Table II. As it can be seen 14 measurements are sufficient for an accurate $a_{L,P}$ prediction. Both models exhibit similar error, approx. -23 dB, over the increasing number of measurements. In fact, the LUT models shows a slightly better overall performance despite its simplicity.

TABLE II: Comparison between the NMSE of the Cardiff model (C.M) and the look-up table (LUT) approach

No. meas.	14	21	28	36
Er./C.M	-23.6	-23.5	-23.5	-23.4
Er./LUT	-23.3	-23.63	-23.7	-23.59

Fig. 6 shows how the generated model has been experimentally used during a load-pull measurement, to predict a generator setting required for emulating specific load targets on the Smith Chart.

It should be noted that to obtain these results a Cardiff model for DUT was employed to predict its non-linear response. The DUT model constantly updates from any in-

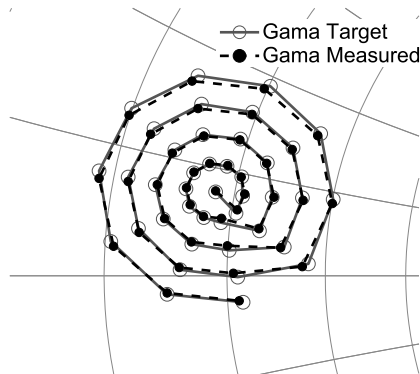


Fig. 6: Comparison between required and measured a_{21} at a DUT reference plane

coming measurement data. The comparison has shown again the high agreement between measured and targeted loads for a load-pull measurement performed on 10W Cree device at 1GHz. The excellent results might be ultimately a combination of both the nonlinear DUT and LPA models. Nevertheless, the addition of the nonlinear LPA model provides a significant improvement of the load-pull accuracy. A load-pull measurement utilizes the same sweep as shown in Fig. 6 and using a constant CF over the entire dynamic range of the signal produced an error of -16.8 dB

IV. CONCLUSION

This paper investigated different approaches for the nonlinear modeling of the LPA signal path within a load-pull system. These models are used to characterize losses and amplifications of a load-pull test-set that effect a required injected signal at DUT reference plane. The models have been experimentally validated under large-signal excitations and their performance compared. Both methods have shown a very good agreement between measured and targeted powers wherein the average magnitude residual difference for the same number of measurements is 0.1 dB. Moreover, it has been found that 14 measurements are enough to generate sufficiently accurate models with an average error at approx. -23 dB. This is a rather surprising result given the simplicity of the LUT-based model. The investigation demonstrates clearly that increasing the complexity of the nonlinear LPA model offers little to no benefit and suggests a straightforward method to improve the performance of an open-loop active load pull system.

ACKNOWLEDGMENT

The authors would like to thank the Karbala Technical Institute, Al-Furat Al-Awsat Technical University for supporting and funding this project.

REFERENCES

- [1] J. Bell, R. Saini, S. Woodington, J. Lees, J. Benedikt, S. Cripps, and P. Tasker, "Behavioral model analysis using simultaneous active fundamental load-pull and harmonic source-pull measurements at x-band," in *Microwave Symposium Digest (MTT), 2011 IEEE MTT-S International*. IEEE, 2011, pp. 1–4.
- [2] M. Thorsell and K. Andersson, "Fast multiharmonic active load –pull system with waveform measurement capabilities," *IEEE Transactions on Microwave Theory and Techniques*, vol. 60, no. 1, pp. 149–157, Jan. 2012.
- [3] M. S. Hashmi, A. L. Clarke, S. P. Woodington, J. Lees, J. Benedikt, and P. J. Tasker, "An accurate calibrate-able multiharmonic active load –pull system based on the envelope load –pull concept," *IEEE Transactions on Microwave Theory and Techniques*, vol. 58, no. 3, pp. 656–664, Mar. 2010.
- [4] P. J. Tasker, "Practical waveform engineering," *IEEE Microwave Magazine*, vol. 10, no. 7, 2009.
- [5] R. S. Saini, S. Woodington, J. Lees, J. Benedikt, and P. J. Tasker, "An intelligence driven active loadpull system," in *75th ARFTG Microwave Measurement Conference*, May 2010, pp. 1–4.

Automating the Accurate Extraction and Verification of the Cardiff Model via the Direct Measurement of Load-Pull Power Contours

Thoalfukar Husseini¹, Azam Al-Rawachy², Johannes Benedikt³, James Bell³, Paul Tasker³

¹Technical Institute of Karbala, Al-Furat Al-Awsat Technical University, Karbala, Iraq

²Engineering Department, Mosul University, Mosul, Iraq

³School of Engineering, Cardiff University, Cardiff, UK

Email : Husseinith@Cardiff.ac.uk

Abstract—The CAD design of Power Amplifiers requires an accurate non-linear modelling solution. Generally, this is provided by state function (I-V, Q-V) model formulations. These typically require time consuming measurement procedures for model extraction and verification. Look-up table a-wave based behavioral models, i.e. the Cardiff Model, extracted directly from measurement data provide for a robust alternative, addressing both simulation accuracy and model extraction time. The challenge is identifying, in a time efficient manner, the appropriate load-pull impedance space, that ensures the model coefficients are accurately extracted. This paper outlines an automated approach addressing this requirement, that exploits the novel features of emerging high-speed load-pull measurement systems to identify and then measure directly load-pull power contours. The automated approach reduces significantly the number of required measurements, hence the measurement time, compared with the traditional approach while also ensuring an accurate Cardiff Model is extracted. The approach is demonstrated on a 10W packaged Cree HFET.

Index Terms—Load-pull, Behavioral model, Power contours.

I. INTRODUCTION

Load and Source-pull measurements are widely used in the design of power amplifiers to deduce optimum efficiency, gain, linearity, power, and providing a clear understanding of the various modes of amplifier operation [1][2]. For example, one of the important characteristics required for RF designers are load-pull power contours. To define these contours accurately, directly from measurement data, requires a high number (>100) of measurements. The process can thus be very time consuming, hence, the need for measurement strategies, which can considerably speed up this process, are crucial. Several research strategies have been used to address this challenge [3]. One logical approach would be to exploit behavioral models, that can be extracted during the measurement process, to provide for intelligent guidance for the measurement system. In [4] a localized behavioral model was successfully utilized to increase the measurement efficiency of an open-loop active load-pull system to increase the speed of obtaining device performance over an impedance grid that is overlaid a priori on the impedance plane. The approach requires the definition of a sufficiently large grid or successive measurements of the grid to ensure all relevant points are covered.

In this paper, a load based behavioral model concept is introduced and used to fully automate the load-pull measurement process. The strategy developed, allows for the rapid identification of both the appropriate load-pull measurement space

and the computation of an optimum sequence of measurements within this space. In this case, we have computed measurement data-sets that are targeted to be located directly on the load-pull power contours. This approach reduces significantly the number of measurements, hence time required for performance identification.

In addition, this sequence of measurements is shown to be an ideal data-set for the accurate extraction and verification of the a-wave based Cardiff behavioral model formulation compatible with implementation in Power Amplifier design CAD tools. This optimally targeted load-pull data-set allows for a direct comparison between measured and CAD model predicted load-pull power contours.

II. HIGH SPEED MEASUREMENT SYSTEM

Fig. 1 shows a schematic block diagram of the high-speed non-linear measurement system that has been utilized to carry out the measurements in this paper. The system architecture is conceptually similar to previously published systems that are based on a Vector Network Analyzer (VNA) [5]. Data acquisition is performed by vector analyzers and the signal generation by signal generators with magnitude and phase control. These are used for generating open-loop active load-pull a_{2h} signals.

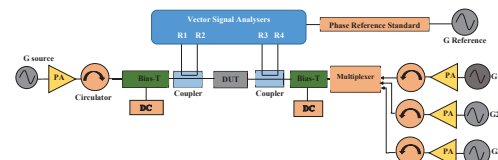


Fig. 1: Block diagram of the high-speed measurement system based on PXIe modules.

III. LOAD BASED BEHAVIORAL MODEL

The approach taken in this work is that once a set of measurements are undertaken a localized fundamental load based behavioral model defined in (1) is extracted.

$$b_{21} = \sum_{D=0}^{D=1} \sum_{C=-(M-D)}^{C=+(M-D+1)} K_{|C|+2D,C} |\Gamma_{21}|^{|C|+2D} \left(\frac{\Gamma_{21}}{|\Gamma_{21}|} \right)^C \quad (1)$$

This model structure is a variant of the Cardiff behavioural modelling concept only in this case b_{21} is a function of the load reflection coefficient Γ_{21} . The user defined parameter, M, defines the model complexity, while $K_{p,q}$ are the extracted model coefficients. This model can be used in the next measurement cycle to compute an array of targeted load-pull $[\Gamma_{21}]$ values, hence the required array of a_{21} values = $b_{21}(\Gamma_{21}) \times \Gamma_{21}$ required for load synthesis in an "open-loop" active load-pull.

IV. OPTIMUM DESIGN SPACE SEARCH ALGORITHM

The strategy of finding the optimum load impedance is based on tracking the maximum output power of each successive data-set of load-pull targets, 28 points defined on a spiral. Fig. 2 shows an example of the search process for the optimum impedance of a 10W Cree packaged device with constant drive power level (around the 2dB gain compression point) at 1 GHz. Bias point $V_{gs} = -3.2V$, $V_{ds} = 28V$. The process includes successive load-pull spirals that end-up with a data-set enclosing the optimum impedance for maximum output power, the last spiral in Fig.2. In this case a load-based behavioral model using $M=1$ (effectively 3rd order), hence extraction of 6 coefficients is sufficient. Typically, about 5-6 cycles are required, so a total time of less than 5sec.

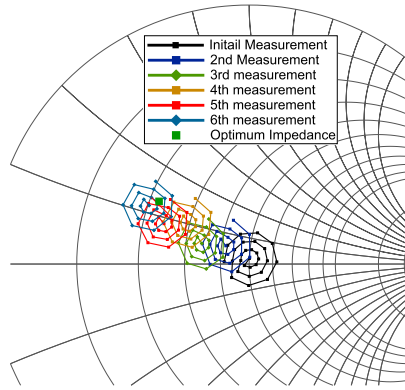


Fig. 2: Optimum impedance tracking of 10W Cree device at constant A_{11} .

Once the location of the maximum power is determined the next step is to identify a design space within which to undertake an optimized data-set of load-pull measurements. In this case we have defined this optimum design space as that encompassed within the $-2dB$ load-pull power contour. Since a key design objective for the CAD models is to accurately predict load-pull contours, a data-set targeting load locations

on an array of load-pull power contours within this design space was considered better than just the simple grid approach. Initially, the required array of $[\Gamma_{21}]$, load targets, is computed using already extracted load-based model with $M=1$. Typically, this first guess does not predict the design space with sufficient accuracy as can be seen in Fig. 3. However, this new dataset, which targeted the power contours allows for extraction of an improved load-based behavioral model with higher complexity, which can then be used to update the array of Γ_{21} , load targets. This process is repeated until sufficient accuracy is achieved. Visually this is simply achieved by comparing the targeted (modeled) and measured load locations on the Smith Chart. An example is shown in Fig. 3, in which three iterations were required, hence total measurement time of less than 2.5sec. In each step a data-set of 140 points, distributed on 5 load-pull contours (-0.1, -0.5, -1.0, -1.5 and -2 dB).

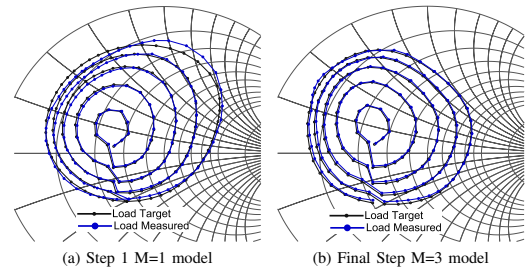


Fig. 3: Comparison showing the iterative convergence of predicted load-pull contours and the measured load locations at 1 GHz.

This plot, Fig. 3 compares the predicted load-pull power contour locations (in blue) with the resulting measured load locations (in black). This figure highlights also how this new approach quickly provides for the direct measurement of the load-pull contours.

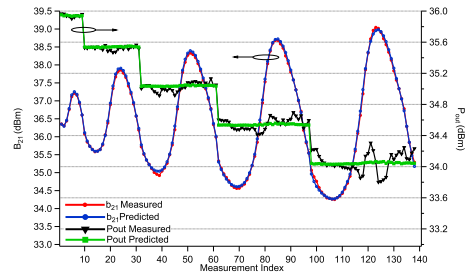


Fig. 4: Comparison of P_{out} and b_{21} at 1 GHz between predicted, using 7th order load-based behavioral model, and directly measured on completion of the iterative search.

The accuracy with which this approached predicted the location of the load-pull contours is quantified in Fig. 4, which compares the predicted and measured b_{21} and P_{out} along all the targeted contours for the final iteration (step 3 with M=3 model). The maximum difference between predicted and measured P_{out} is found on the -2dB contour and is about ± 0.25 dB.

V. CAD BEHAVIORAL MODEL EXTRACTION AND VERIFICATION

We now investigated the use of this optimal data-set, load pull contour targeted measurements, in the extraction and verification of the conventional a-wave based Cardiff behavioral Model. This is a-wave based model format is a compatible CAD tool formulation. The formulation used in this case is given in (2).

$$b_{21} = P \sum_{D=0}^{D=1} \sum_{C=-(M-D)}^{C=(M-D+1)} L_{|C|+2D,C} |a_{21}|^{|C|+2D} \left(\frac{Q}{P}\right)^C \quad (2)$$

In this equation, P is the phase of the input a_{11} stimulus, while Q is the phase of the output a_{21} stimulus. The user defined parameter M , again defines the model complexity, while $L_{p,q}$ are the extracted model coefficients.

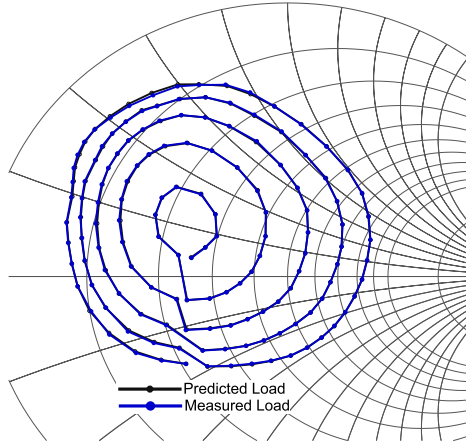


Fig. 5: Demonstration of the ability of the 7th order a-b Cardiff behavioral model, to accurately predicted load locations associated with the targeted load-pull contours at 1 GHz.

In order to determine the necessary model complexity, different values of M were investigated, beginning with $M=1$ (effectively 3rd order) and ending with $M=4$ (effectively 9th order). The comparison confirms that model accuracy increases with increasing complexity. This new approached verified that, in this case, a Cardiff Models with sufficient accuracy for CAD design can be achieved using a model with $M=3$ (effectively 7th order). A model with only 14 coefficients. Fig. 5 shows comparison between measured and

predicted, using 7th order a-based Cardiff behavioral model, load locations associated with the targeted load-pull contours. Fig. 6 compares the measured and modeled values of b_{21} and P_{out} , verifying the excellent accuracy of the Cardiff Model within the -2dB contour design space. In this case, the maximum difference, which is on the -2dB load-pull contour is only ± 0.25 dB.

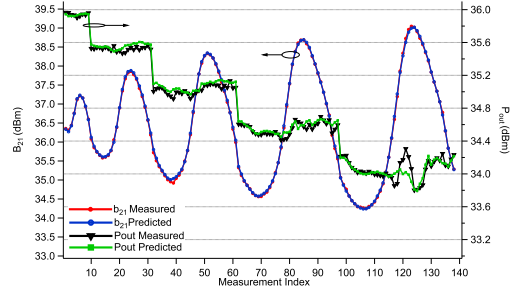


Fig. 6: Demonstration of the ability of the 7th order a-b Cardiff behavioral model, to accurately predicted Pout and b_{21} , on the targeted load-pull contours at 1 GHz.

VI. CONCLUSION

An advanced and automated approach addressing the challenge of identifying, in a time efficient manner, the appropriate load-pull impedance space for RF devices. It ensures also that an accurate behavioral model extraction is obtained. The novel features of emerging high-speed load-pull systems not only allows for more measurement data but also introduces new capabilities that are highly relevant in RF device modeling and RFPA design. The novel approach taken provides optimal data-sets by selecting load impedances that target the direct measurement of load-pull contours; the essential design information. While this minimizes the number of measurements required, hence measurement time, accuracy of extracted behavioral models is not compromised. This optimal data-set allowed for both the accurate extraction and verification of a-wave based Cardiff Behavioral models. The ability of this CAD compatible model to accurately predict the load-pull contours within the -2dB load-pull power contour design space, was directly verified. The complete process was achieved by performing less than 565 measurements in a total measurement time of only 6.6 sec.

ACKNOWLEDGMENT

The authors would like to thank the Karbala Technical Institute, Al-Furat Al-Awsat Technical University for supporting and funding this project.

REFERENCES

- [1] J. Benedikt, R. Gaddi, P. J. Tasker, and M. Goss, "High-power time-domain measurement system with active harmonic load-pull for high-efficiency base-station amplifier design," *IEEE Transactions on Microwave Theory and Techniques*, vol. 48, no. 12, pp. 2617–2624, Dec. 2000.
- [2] J. Bell, R. Saini, S. Woodington, J. Lees, J. Benedikt, S. Cripps, and P. Tasker, "Behavioral model analysis using simultaneous active fundamental load-pull and harmonic source-pull measurements at x-band," in *Microwave Symposium Digest (MTT), 2011 IEEE MTT-S International*. IEEE, 2011, pp. 1–4.
- [3] M. Thorsell and K. Andersson, "Fast multiharmonic active load –pull system with waveform measurement capabilities," *IEEE Transactions on Microwave Theory and Techniques*, vol. 60, no. 1, pp. 149–157, Jan. 2012.
- [4] R. S. Saini, J. W. Bell, T. A. J. Canning, S. P. Woodington, D. FitzPatrick, J. Lees, J. Benedikt, and P. J. Tasker, "High speed non-linear device characterization and uniformity investigations at x-band frequencies exploiting behavioral models," in *Proc. 77th ARFTG Microwave Measurement Conf*, Jun. 2011, pp. 1–4.
- [5] P. J. Tasker, "Practical waveform engineering," *IEEE Microwave Magazine*, vol. 10, no. 7, 2009.

Cardiff Behavioural Model Analysis using a Two-Tone Stimulus

*Azam Al-Rawachy, ‡ Thoalfukar Husseini, † Johannes Benedikt, † Paul Tasker, † James Bell

*Software Engineering Department, Mosul University, Mosul, Iraq

†School of Engineering, Cardiff University, Cardiff, UK, CF24 3AA

‡Technical Institute of Karbala, Al-Furat Al-Awsat Technical University, Karbala, Iraq

AL-RawachyAA@Cardiff.ac.uk

Abstract—This paper presents a new technique for identifying the mixing structure, model coefficients and therefore model order of the Cardiff behavioral model for phase related nonlinearities. The technique employs a two-tone measurements approach and the Fast Fourier Transform (FFT) to be able to observe the mixing structure above the noise floor of the measurement system. Spectral tone visibility explicitly requires model coefficient inclusion for accurate (NMSE < -40dB) data fitting, which is verified by comparing model fitting of full and truncated model formulations. The identified maximum phase model order from two-tone measurements, for annuli on the Smith Chart, is shown to be accurate for Continuous Wave (CW) measurements.

Index Terms—Behavioral model, Two-tone stimulus, device nonlinear models.

I. INTRODUCTION

Behavioral models are a necessary tool to transport device data, from a developing technology, into CAD for further design related analysis. The Cardiff Model exploits the property that when multiple stimuli are injected into a multi-port nonlinear system they interact or 'mix'. The Cardiff Model is defined in the frequency domain and when correctly implemented should include all the resulting frequency components. Hence, the Cardiff Model differentiates itself from other popular behavioral modeling formulations, S-parameters, Polyharmonic Distortion (PHD) modeling [1], [2] and X-parameters [3], by not limiting the number of model coefficients that can be extracted; for example, 2 coefficients for S-parameters and 3 for analytical X-parameters and PHD modeling. This approach allows for a global model fit of data, obtained by executing impedance sweeps over an area of the Smith Chart, rather than a local fit about/at each impedance point of the sweep. Previous work in [4] has verified the Cardiff Model coefficient structure so that global models of harmonic source and load-pull data can be accurately extracted with attempts at avoiding over-fitting the data.

In this paper, a new technique for determining the correct, and present, phase polynomial coefficients of the Cardiff Model will be presented. This technique utilizes two-tone measurements and the Fast Fourier Transform (FFT) to be able to observe the mixing order and resultant intermodulation (IMD) products and demonstrate that they are directly correlated to the modeling coefficients used in the Cardiff Model. This approach allows for the direct and accurate determination of

the maximum number of model phase coefficients needed for two-tone and CW measurements.

II. THE MEASUREMENT SYSTEM ARCHITECTURE AND PROCEDURE

The measurement system for this paper utilizes two Arbitrary Waveform Generators (AWG) to enable two-tone generation, and four Vector Signal Analyzers (VSAs) for traveling-wave acquisition. Fig. 1 shows a block diagram of the measurement system, which is comprised of the aforementioned AWGs and VSAs and also driver PAs, filters, and a calibrated test-set. The system architecture is fundamentally linked to previous work on Vector Network Analyzer (VNA) based systems [5]. Fig. 1 also depicts the measurement scenario by showing the DUT input driven by a single tone and the DUT output driven by a two-tone stimulus. The chosen DUT is the Wolfspeed 10W packaged device, biased at $V_{gs}=-2.8V$ and $V_{ds}=28V$, driven with $|a_{11}| = 24.65dBm$.

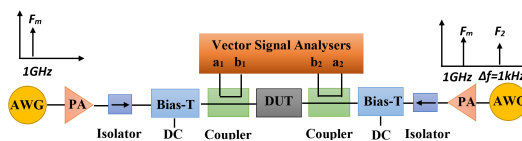


Fig. 1. Block diagram of the measurement system.

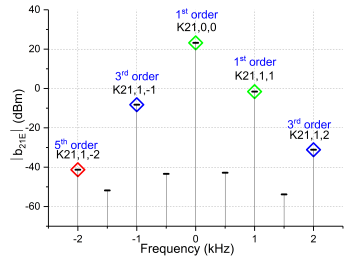
The VSAs have an instantaneous 50MHz bandwidth, which allows for the acquisition of the down converted two tones and IMD products without changing the Local Oscillator (LO) frequency. Due to limits on the calibration coefficients being able to extend over a 50MHz bandwidth, the main-tone frequency was chosen to be 1GHz and the tone frequency spacing was limited to 1kHz; very close to the calibrated frequency.

To ensure the data was design relevant, the main tone impedance was located at the DUT's optimum power point on the Smith Chart, using the algorithm in [6]. To be able to investigate the presence of model terms and their relation to the IMD spectra, the 2nd output tone magnitude $|a_{21,2}|$ was varied from -6dBc to +6dBc of the main tone signal magnitude, $|a_{21,1}|$. This will create growing levels of observable distortion in the b-wave response and hence a growing model complexity and load modulation coverage of the Smith Chart.

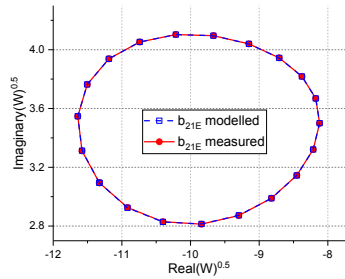
III. SPECTRAL ANALYSIS OF THE BEHAVIORAL MODEL

In order to analyze the received, down converted spectra, the selected tones in the receiver bandwidth needed to be calibrated and phase-normalized to the input traveling-wave (a_{11}) at the main tone frequency (1GHz). This established a relative phase system, key for behavioral modeling and analysis [2]–[4]. The raw, down converted IMD tones lie on a harmonic grid ($\pm n \cdot 1\text{kHz}$) and were compared to a proposed noise floor of -85dB for selection before calibration. Using the IFFT, the time-domain traveling-wave quantities were then constructed from the selected tones. This allowed for b-wave analysis and load modulation coverage to be observed on the Smith Chart. All noise tones were removed in this process. After identifying the maximum model order for the two-tone measurements, selected impedances were used for CW measurement and model analysis was performed to verify whether the identification holds for the CW domain.

Fig. 2 (a) depicts the down converted $|b_{21E}|$ (the b-envelope about the fundamental tone) spectral plot, for $|a_{21,2}| = -6\text{dBc}$, and links the observable tones, above the noise floor, to Cardiff Model coefficients ($K_{ph,m,\varphi}$). The 'p' and 'h' subscripts denote the respective port and harmonic, and the 'm' and ' φ ' subscripts denote the coefficient's related traveling-wave mag and phase exponent respectively (see eq.1). Overlaid, on the model tones is the associated model term contribution (e.g., $K_{21,1,1}|a_{21E}|(\frac{Q}{P})$) after extracting the model for eq. 1. The almost exact overlap indicates the accuracy of the model formulation's ability to fit the data.



(a) $|b_{21E}|$ spectrum showing 5th order coefficients.



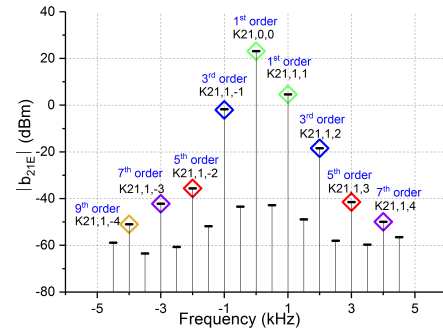
(b) b_{21E} comparison for the selected coefficients.

Fig. 2. b_{21E} analysis for $|a_{21,2}| = -6\text{dBc}$.

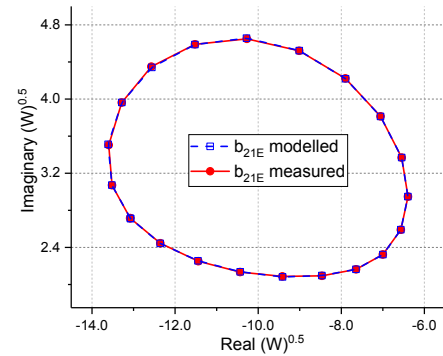
Equation 1 formulates the required Cardiff Model in this case based on the observations from the spectra in fig. 2 (a) this is a relative phase polynomial only, as each annulus is taken at a fixed $|a_{21}|$ injection and the relative phase is the only variable. Fig. 2 (b) shows the comparison between b_{21E} model and measured data, it clearly shows an accurate model fit to the data and verifies the fit of the model terms, in eq. 1, to the spectral tones, in fig. 2 (a).

$$\frac{b_{21}}{P} = K_{(21,0,0)} + K_{(21,1,1)}|a_{21E}|(\frac{Q}{P}) + K_{(21,1,-1)}|a_{21E}|(\frac{Q}{P})^{-1} + K_{(21,1,2)}|a_{21E}|(\frac{Q}{P})^2 + K_{(21,1,-2)}|a_{21E}|(\frac{Q}{P})^{-2} \quad (1)$$

Fig. 3 (a) shows the resulting spectrum for $|a_{21,2}| = 0\text{dBc}$, and indicates that stronger mixing process are present, which requires a commensurate model formulation (9th order) for accurate model extraction. Again, the overlaid extracted model term contributions map directly onto the spectral lines. Fig. 3 (b) shows another good model fit to the measured data.



(a) $|b_{21E}|$ spectrum showing 9th order coefficients.



(b) b_{21E} comparison for the selected coefficients.

Fig. 3. b_{21E} analysis for $|a_{21,2}| = 0\text{dBc}$.

The final measurement, where $|a_{21,2}| = 6\text{dBc}$ of the main tone, was performed to cover a significant area of the Smith Chart. Fig. 4 shows the resultant $|b_{21E}|$ spectrum, from which the Cardiff Model equation was formulated commensurate with the observed model order.

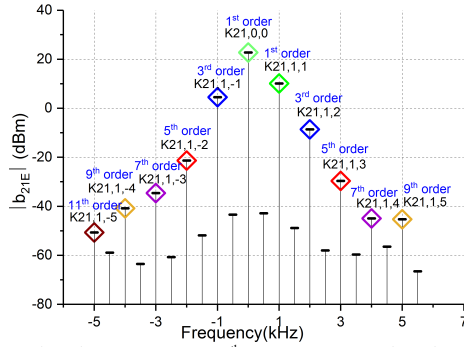
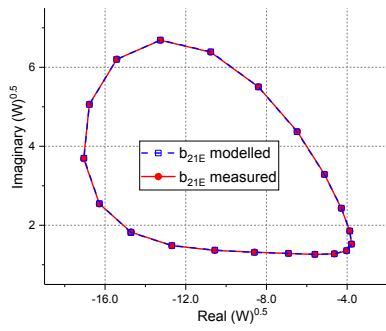
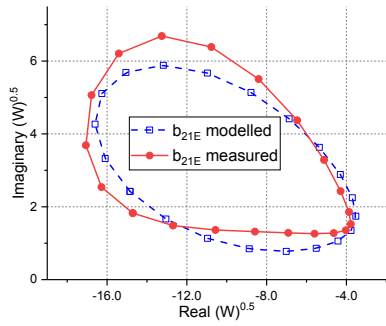


Fig. 4. $|b_{21E}|$ spectrum showing 11th order coefficients for $|a_{21,2}| = 6\text{dBc}$.



(a) b_{21E} comparison for 11 coefficients (Cardiff model).



(b) b_{21E} comparison for 3 coefficients (analytical X-parameter model).

Fig. 5. b_{21E} analysis for $|a_{21,2}| = 6\text{dBc}$.

Fig. 5 shows the comparison between model and measurement data for full and truncated models. To demonstrate the inaccuracy of model truncation, the full 11th order Cardiff Model, in (a), has been compared with the 3-term analytical X-parameter model, in (b), and clearly shows a limitation of the analytical X-parameter model for this $|a_{21,2}|$. However, $|a_{21,2}| = 2\text{dBc}$ is where the analytical X-parameter formulation begins to produce a normalized mean square error (NMSE) $> 40\text{dB}$, above 1% error, below 2dBc the error is acceptable but not optimal.

Fig. 6 shows all the annuli collected in the measurement process with each annulus being modeled with its corresponding, spectrally-identified, behavioral model equation. Fig. 7 shows the impedance area covered by the load-modulation that occurs from the two-tone measurements. The -6dBc , 0dBc , and 6dBc annuli are highlighted and the optimum load is plotted with an asterisk. This shows that, with only 7 measurements, a large area of the Smith Chart can be captured and the maximum model order identified for each area. To verify this result for normal CW measurements, the trace icons in fig. 7 were used as CW impedance targets and model analysis was performed on the received data.

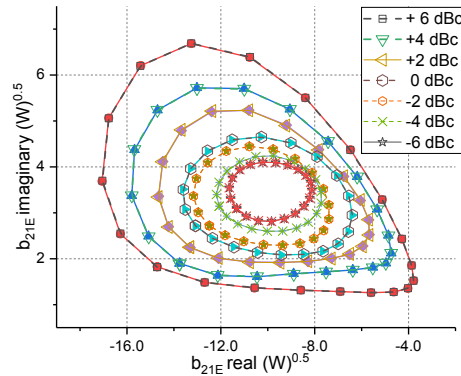


Fig. 6. b_{21E} modeled and measured comparisons for different $|a_{21,2}|$ power levels with phase variation only.

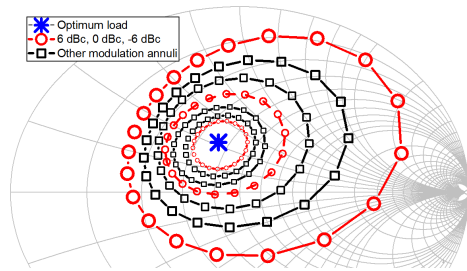


Fig. 7. Load-modulation annuli for different $|a_{21,2}|$ power levels. Trace icons indicate impedance targets for CW measurement.

Fig. 8, plots the NMSE, for selected $|a_{21,2}|$ power levels, against model order for the two-tone and CW cases. It can be seen that the addition of model coefficients increases the accuracy of the model and that the two-tone and CW results are offset for $|a_{21,2}| = 0\text{dBc}$ and $|a_{21,2}| = 6\text{dBc}$, this is due to an a_{21} that exhibits magnitude and phase variation for the larger annuli in fig. 7. However, it can be seen that the maximum model order, obtained from the two-tone measurements, holds for the CW case (NMSE $< -40\text{dBm}$). In both cases, small gains in accuracy can be achieved after the identified model order, however, the models would be over-determined.

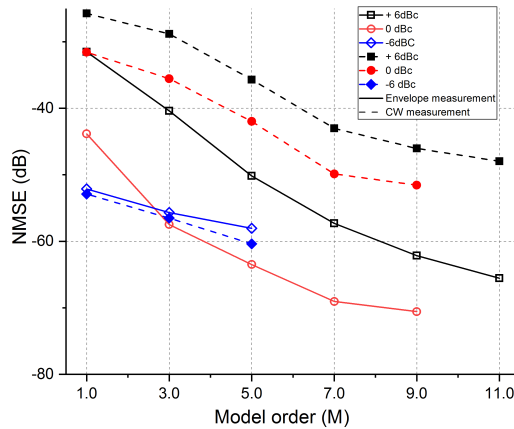


Fig. 8. NMSE versus model order for two-tone measurements at selected $|a_{21,2}|$ and CW measurements with impedances lying on their respective two-tone load-modulation annuli.

IV. CONCLUSION

A new technique, exploiting two-tone measurements, for the correct determination of Cardiff Model phase coefficients has been introduced. Using this technique, the analytical X-parameter model formulation has been shown to remain accurate until $|a_{21,2}| = 2\text{dBc}$, however, higher order formulations are required for better accuracy with increasing $|a_{21,2}|$ power levels. The $|a_{21,2}|$ perturbation has been increased to cover a substantial area of the Smith Chart and is accurately modeled by an 11th order phase polynomial. This approach allows for the maximum model complexity to be clearly identified directly from measurements, hence allowing for the direct extraction of both the maximum model order as well as the associated coefficients. Using impedance targets obtained from the two-tone measurements, model analysis was performed for CW measurements over the same area of the Smith Chart, and shows that the model identification can directly be applied to CW measurements for accurate models that avoid over-determination.

ACKNOWLEDGMENT

I would like to dedicate my gratitude to the Higher Committee for Education Development (HCED) in Iraq for supporting and funding this project.

REFERENCES

- [1] K. Kurokawa, "Power waves and the scattering matrix," vol. 13, no. 2, IEEE, 1965, pp. 194–202.
- [2] D. Root *et al.*, "Polyharmonic distortion modeling," *IEEE microwave magazine*, vol. 7, no. 3, pp. 44–57, 2006.
- [3] D. Root, J. Horn, L. Betts, C. Gillese, and J. Verspecht, "X-parameters: The new paradigm for measurement, modeling, and design of nonlinear rf and microwave components," no. 12, 2008, p. 16.
- [4] J. Bell, R. Saini, S. Woodington, J. Lees, J. Benedikt, S. Cripps, and P. Tasker, "Behavioral model analysis using simultaneous active fundamental load-pull and harmonic source-pull measurements at x-band," in *Microwave Symposium Digest (MTT), 2011 IEEE MTT-S International*. IEEE, 2011, pp. 1–4.
- [5] P. J. Tasker, "Practical waveform engineering," *IEEE Microwave Magazine*, vol. 10, no. 7, 2009.
- [6] T. Hussein, A. Al-Rawachy, J. Benedikt, J. Bel, and P. Tasker, "Automating the accurate extraction and verification of the cardiff model via the direct measurement of load-pull power contours," in *2018 IEEE/MTT-S International Microwave Symposium-IMS*. IEEE, 2018, pp. 544–547.